GLOBAL AND LOCAL BUCKLING ANALYSIS OF STIFFENED AND SANDWICH PANELS USING MECHANICS OF STRUCTURE GENOME

A Dissertation

Submitted to the Faculty

of

Purdue University

by

Ning Liu

In Partial Fulfillment of the

Requirements for the Degree

of

Doctor of Philosophy

May 2019

Purdue University

West Lafayette, Indiana

THE PURDUE UNIVERSITY GRADUATE SCHOOL
STATEMENT OF DISSERTATION APPROVAL

Dr. Wenbin Yu, Chair

School of Aeronautics and Astronautics

Dr. Vikas Tomar

School of Aeronautics and Astronautics

Dr. Arun Prakash

School of Civil Engineering

Dr. Tyler Tallman

School of Aeronautics and Astronautics

Approved by:

Dr. Weinong Chen

Head of the School Graduate Program

ACKNOWLEDGMENTS

Firstly, I would like to express my sincere gratitude to my advisor Prof. Wenbin Yu for the continuous support of my PhD study and related research, for his patience, motivation, and immense knowledge. His guidance helped me in all the time of research and writing of this thesis. Besides my advisor, I would like to thank the rest of my thesis committee: Prof. Vikas Tomar, Prof. Arun Prakash and Prof. Tyler Tallman, for their insightful comments and encouragement. I also thank my colleagues at Purdue University: Dr. Liang Zhang, Dr. Fang Jiang, Dr. Hamsasew Sertse, Bo Peng, Zhenyuan Gao, Yufei Long, Su Tian, Xin Liu, Banghua Zhao, Ankit Deo, Ernesto Camarena, Fei Tao among others. You are not only my colleagues, but my friends and mentors. Last but most importantly, I want to express my deepest gratitude to my beloved parents, Gang Liu and Xuehong Yang for standing by me in good and bad times and giving me strength to move forward.

TABLE OF CONTENTS

Page

LIST OF TABLES

LIST OF FIGURES

Figure Page

Figure Page

ABSTRACT

Liu, Ning Ph.D., Purdue University, May 2019. Global and Local Buckling Analysis of Stiffened and Sandwich Panels Using Mechanics of Structure Genome. Major Professor: Wenbin Yu Professor.

Mechanics of structure genome (MSG) is a unified homogenization theory that provides constitutive modeling of three-dimensional (3D) continua, beams and plates. In present work, the author extends the MSG to study the buckling of structures such as stiffened and sandwich panels. Such structures are usually slender or flat and easily buckle under compressive loads or bending moments which may result in catastrophic failure.

Buckling studies of stiffened and sandwich panels are found to be scattered. Most of the existed theories employ unnecessary assumptions or only apply to certain types of structures. There are few unified approaches that are capable of studying the buckling of different kinds of structures altogether. The main improvements of current approach compared with other methods in the literature are avoiding unnecessary assumptions, the capability of predicting all possible buckling modes including the global and local buckling modes, and the potential in studying the buckling of various types of structures.

For global buckling that features small local rotations, MSG mathematically decouples the 3D geometrical nonlinear problem into a linear constitutive modeling using structure genome (SG) and a geometrical nonlinear problem defined in a macroscopic structure. As a result, the original structures are simplified as macroscopic structures such as beams, plates or continua with effective properties, and the global buckling modes are predicted on macroscopic structures. For local buckling that features finite local rotations, Green strain is introduced into the MSG theory to achieve

geometrically nonlinear constitutive modeling. Newton's method is used to solve the nonlinear equilibrium equations for fluctuating functions. To find the bifurcated fluctuating functions, the fluctuating functions are then perturbed under the Bloch-periodic boundary conditions. The bifurcation is found when the tangent stiffness associated with the perturbed fluctuating functions becomes singular. Moreover, the arc-length method is introduced to solve the nonlinear equilibrium equations for post-local-buckling predictions because of its robustness. The imperfection is included in the form of geometrical imperfection by superimposing the scaled buckling modes in linear perturbation analysis on mesh.

Extensive validation case studies are carried out to assess the accuracy of the MSG theory in global buckling analysis and post-global-buckling analysis, and assess the accuracy of the extended MSG theory in local buckling and post-local-buckling analysis. Results using MSG theory and extended MSG theory in buckling analysis are compared with direct numerical solutions such as 3D FEA results and results in literature. Parametric studies are performed to reveal the relative influence of selective geometric parameters on buckling behaviors. The extended MSG theory is also compared with representative volume element (RVE) analysis with Bloch-periodic boundary conditions using commercial finite element packages such as Abaqus to assess the efficiency and accuracy of the present approach.

1. INTRODUCTION

Structural instability has been an important branch of structural analysis in the design of modern structural systems. The loss of stability is usually associated with the scenarios that structures pass from one deformation pattern commonly seen in compression to another. For example, an axially-loaded column which originally remains straight deforms into a combination of compression and bending. The load at which structures experience dramatic transition in deformation is usually called the critical load and such structural instability is also called buckling. Figure 1.1 shows a buckled tank caused by axial compression and axisymmetric hoop tension.

Fig. 1.1. A stainless-steel wine tank buckled at the Wente Brothers Winery caused by earthquake in the Livermore, California on January 24, 1980 [1].

A number of approaches have been proposed and applied to the structural buckling analysis over history. Classical approaches seek to find such an equilibrium that two or more deformation patterns coexist at the same time. The point which indicates coexisted deformation patterns is called the bifurcation point (see the intersection of primary path and secondary path in Fig. 1.2). The stress is redistributed at the bifurcation point which results in a lower strain energy level in the secondary path. Mathematically, the classical approach linearizes the buckling problem to an eigenvalue problem in which the eigenvalues are the critical loads and the eigenvectors are the buckling mode shapes. Another category is the perturbation approach. A small disturbance is introduced to the system and causes the system deviated from the equilibrium state. The deviation can be made as small as desired. The critical condition is reached if such a small disturbance causes a finite deviation of the system from the considered equilibrium state [2,3]. Other approaches include but not limit to the energy approach, which states the onsets of instability are established when the second variation of the potential energy about a static equilibrium state becomes semi-definite [4], and etc.

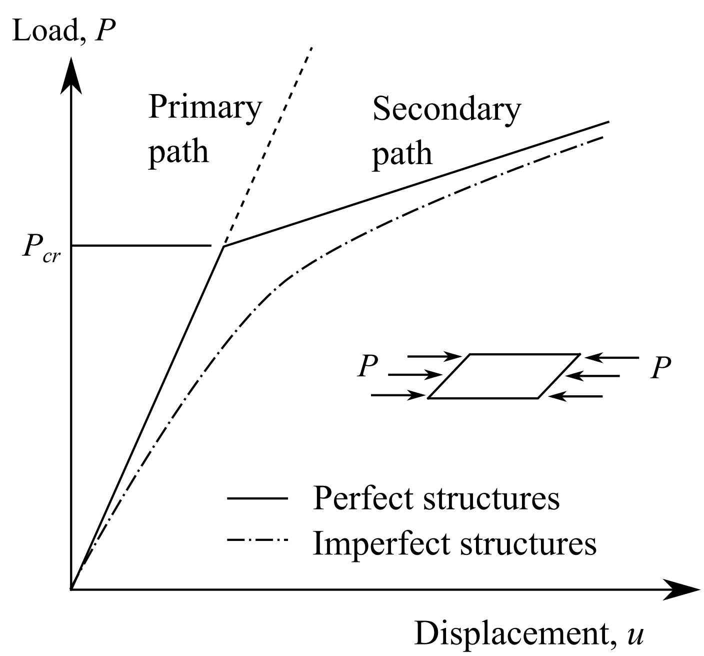

Fig. 1.2. An example of load/displacement curve in buckling of plates subject to uniaxial compressive loads. The bifurcation point disappears in the presence of imperfection.

Buckling loads and associated buckling mode shapes of a structure or structural component depend on many factors, such as the geometries, materials and/or boundary conditions. For example, two distinctive types of responses, local buckling and global buckling, are found in the buckling of stiffened panels (Fig. 1.3). The local buckling is seen as the occurrence of buckled skin between stiffeners. The global buckling, not seen between the stiffeners, involves lifting the stiffeners together with the skin. Other types of buckling are seen in buckling of stiffeners, interactive buckling which is a mix of aforementioned buckling modes. If the stiffeners have small flexural rigidities or are closely distributed, they tend to buckle together with the skin, giving rise to a global mode. If the stiffeners are flexurally stiff or sparsely distributed, buckling occurs in a local mode. Buckling is also seen in other types of structures for example the sandwich structures, porous structures, etc.

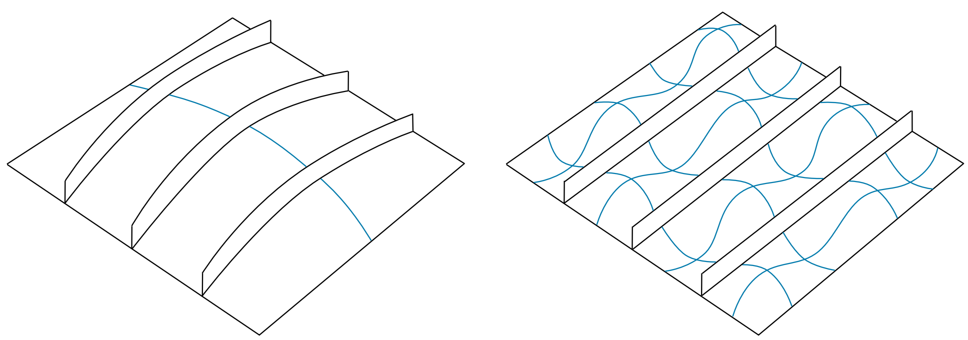

(a) Global mode (b) Local mode

Fig. 1.3. Two main buckling modes of stiffened plates.

When the buckling occurs, structures enter the post-buckling regime (secondary path in Fig. 1.2). The bifurcation point disappears in the presence of imperfection. While the classical buckling analysis yields a good estimation of the load at which a perfect structure undergoes buckling deflections, it gives no indication of how imperfect structures behave, nor does it shed light on the post-buckling behavior. The actual buckling loads from test results are frequently found to be as little as one-quarter of the classical loads [4]. Koiter [5] showed that a small amplitude of imperfection in cylindrical shells caused significant reduction in buckling load. In practice, the allowable critical load is reduced by an empirical knockdown factor (Fig. 1.4) that accounts for imperfection associated with geometry, material, loading and boundary conditions. The conservative lower-bound design philosophy developed in the late 1960s has been widely used for metallic structures [6–12]. Besides, both the pre-buckling and the post-buckling behavior of an imperfect structure can be noticeably nonlinear. The nonlinearity comes from the nonlinear kinematic relations in finite deformation theory and nonlinear material behavior. The general approach for post-buckling analysis requires complex nonlinear equilibrium equations to be solved incrementally [13,14]. The finite element analysis (FEA) enables accurate results but with a cost of high computational effort and long simulation time. The presence of composite lamination, or new materials such as functionally graded materials (FGM) even escalates the computational effort due to large number of involved degrees of freedom.

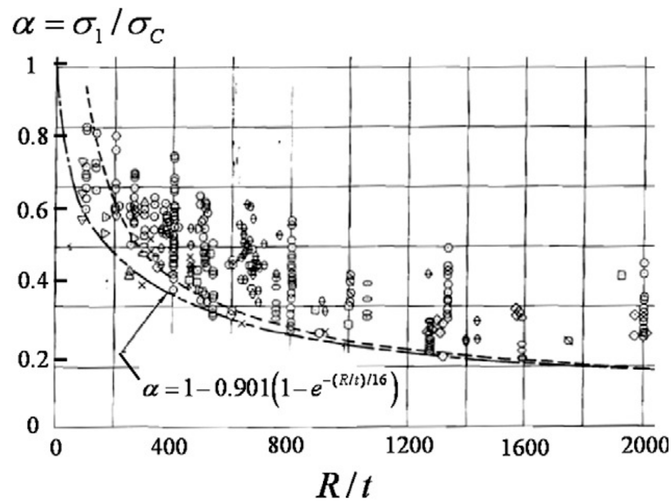

Fig. 1.4. The recommended knockdown factor for uniaxially compressed cylindrical shells measured from experimental data plotted against the radius to thickness ratio R/t [15].

Extensive efforts are made to develop analytical or semi-analytical approaches to improve accuracy and efficiency on buckling and post-buckling predictions. Various assumptions are made in the studies, such as modeling the stiffeners of stiffened panels and skins of sandwich structures as Euler–Bernoulli beams [16, 17]. Early developed theories either lack of accuracy [18, 19] or only apply to specific structures [20] or certain types of buckling modes [21, 22]. Detailed literature reviews on the buckling studies of stiffened and sandwich panels are given in the following sections.

1.1 Literature review on the buckling of stiffened panels

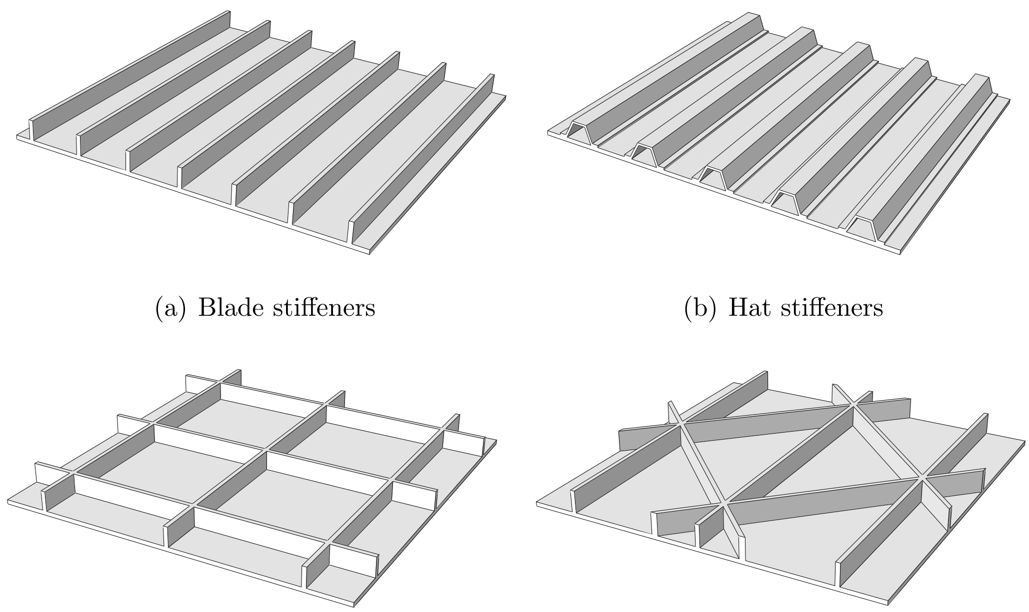

(a) Blade stiffeners

(b) Hat stiffeners

(c) Orthogrid stiffeners

(d) Isogrid stiffeners

Fig. 1.5. Examples of stiffened panels.

Stiffened panels have been widely used in different fields including aerospace engineering, civil engineering and marine engineering. By adding stiffeners to plate, the bending stiffness of the structure is greatly enhanced without increasing too much weight and cost. Typical examples of stiffened panels are shown in Fig. 1.5. However, stiffened panels are usually flat and easily buckle under compressive loads. The buckling analysis of stiffened panels has been a subject of interest in the study of stiffened panels for many years. Depending on the flexural stiffness of stiffeners and the space between stiffeners, buckling modes are generally seen in two types, i.e., the global buckling mode and the local buckling mode (Fig. 1.3). In global modes, skin and stiffeners are lifted together while in local modes only the skins between stiffeners are lifted or the stiffeners are buckled. The author presents below the literature reviews on global and local buckling studies of stiffened panels respectively. Copyright has been obtained to reuse the published materials from [23].

1.1.1 Global buckling of stiffened panels

According to the failure mode map [24], global buckling is considered to be the major failure mode for stiffened shells under axial compression or/and external pressure [25] and the design objective for optimization [26]. Among the methods to study global buckling of stiffened panels, extensive studies are focused on the finite element method (FEM) and the smeared stiffener method (SSM). FEM enables accurate results without limitations regarding boundary conditions, stiffener shapes and/or lay-up sequences. However, it has been showed that modeling the stiffeners using two-dimensional (2D) elements resulted in significant error in the predicted buckling loads in comparison with using three-dimensional (3D) elements [27]. Accurate buckling simulation of stiffened panels generally needs high computational effort and long simulation time, prohibiting evaluation of different configurations and materials in preliminary design and optimization [28].

The smearing techniques for plate and shell analysis have been thoroughly summarized by Szilard [29]. The basic idea is to smear the stiffness of stiffeners into the plate and compute effective shell properties. Various SSMs are proposed over the years based on this idea. The SSMs are in general computationally efficient to execute, however, most of existing SSMs are either lack of accuracy or developed to study the stiffened panels with specific stiffened patterns or materials. The extension-bending coupling interaction caused by the eccentricity of stiffeners was neglected in the study by Chen et al. [18], which resulted in the imprecise prediction of buckling results [30]. The SSM proposed by Jaunky et al. [20] only applied to symmetric laminates. Byklum et al. [31] proposed a SSM to study the stiffened panels with stiffeners in longitudinal and transverse directions. The resultant forces and moments were assumed to be decoupled, which made this approach difficult to use for composite structures. Kidane et al. [16] superimposed the forces and moments of the stiffeners on those of the shell to compute the effective shell properties. The method simplified the stiffeners as beams without considering the transverse shear stiffness and neglected the skin-stiffener interaction. Xu et al. [32] took into consideration the skin-stiffener interaction and proposed an improved SSM. It was applied to various stiffened patterns but only the longitudinal modulus of the stiffeners was included in the theory. Numerical-based SSM were developed to combine the efficiency of SSM with the accuracy of FEM [18, 19, 33].

Recently, the development of new materials such as FGM initiated active research on buckling behaviors of stiffened FGM structures. Ninh et al. [34] studied torsional buckling and post-buckling of stiffened FGM toroidal shell. The same authors [35] also investigated dynamical buckling of stiffened FGM toroidal shell under dynamical pressure of fluid. Dung et al. [36–38] studied buckling and post-buckling of FGM truncated conical shells reinforced by orthogonal stiffeners under thermomechanical loads. Theoretical formulations in these research studies [34–38] are derived based on SSMs and classical thin shell theory with geometrical nonlinearity in the von Karman sense.

Due to the fact that most of SSMs are developed for specific grid-patterns or materials, the applications of such SSMs for covering various stiffener patterns are greatly challenged. Homogenization methods do not have such limitations regarding stiffener patterns or materials. By using the asymptotic expansions and the assumption of periodicity, physical quantities can be evaluated on two different levels: the macroscopic and the microscopic, where the former implies slow variation and the latter implies rapid oscillations [39]. Homogenization has been widely used in calculating effective properties of a heterogeneous medium [40–42].

It should be pointed out that there are many multiscale methods in the literature. Besides the homogenization theories mentioned above [39, 43, 44], the multi-scale finite element method (MsFEM) [45–48] also attracted significant attention. The main idea of MsFEM is to construct multiscale finite element base functions through discretizing the microstructure with a fine mesh while keeping a coarse mesh on the global domain. The construction of base function is fully decoupled from element to element which allows MsFEM to study non-periodic structures and avoid scale separation assumption [48].

1.1.2 Local buckling of stiffened panels

Extensive numerical approaches are developed to study local buckling of stiffened panels. In general, they do not have limitations regarding stiffener profiles and material properties. However, accuracy of the solutions by numerical methods depends on the mesh size and the shape functions selected to approximate displacement fields. Mallela and Upadhyay [49] used commercial finite element (FE) program to carry out a parametric study on simply supported laminated composite blade-stiffened panels subjected to in-plane shear loading. A variety of stiffeners and materials were studied. Patel et al. [50] presented a FE formulation for analysis of stiffened shells subjected to uniform in-plane harmonic edge loading. Degenerated beam and shell elements were used to model stiffeners and plates. FE-based numerical approaches are also seen in Graciano and Lagerqvist [51], Madhavan and Davidson [52], Ghavami and Khedmati [53]. Ovesy et al. [54] used finite strip method (FSM) for post-local-buckling analysis of thin-walled prismatic structures under uniform compression. Bedair [55, 56] presented a numerical approach for buckling analysis of stiffened plates that idealized the structure as assembled plates and beams and claimed that the method does not require discretization to the structure unlike FEM or FSM. Peng et al. [57] presented a mesh-free Galerkin method for stability analysis of stiffened panels. A first-order shear deformation theory was used to approximate displacements of the plate and stiffeners. Moreover, the in-plane bending and torsional stiffness of the stiffeners are neglected.

Besides numerical approaches, efforts are also made in developing analytical or semi-analytical methods such as those simplifying stiffeners as constraints to the plate. Byklum and Amdahl [58] developed a simplified method for local buckling of isotropic stiffened panels. The structure being considered is the panel between stiffeners. The stiffeners are replaced with simply supported boundary conditions to the panel. Bisagni and Vescovini [28] developed an analytical formulation for the local buckling and post-buckling analysis of isotropic and laminated stiffened panels under uniaxial compression. The stiffeners are modeled as rotational bars and provide rotational rigidities to the panel. The method was later extended by the same authors to study curved stiffened panels [59, 60]. Similar constraints are seen in [61] with a focus on panels stiffened by omega-stringers. Stamatelos et al. [62] modeled the stiffeners as compression and torsion springs. After the idealization made to stiffeners in these studies, the local buckling loads are solved by Ritz method. The accuracy of the solution by Ritz method varies by the selection of trial functions and the number of terms chosen for approximation.

1.2 Literature review on the buckling of sandwich panels

Sandwich structures are important structural elements in modern lightweight engineering. Sandwich structures generally consist of two relatively thin stiff face sheets separated by a relatively thick soft core. The face sheets are designed to carry in-plane loads whereas the core is to support the face sheets. The most important characteristic of sandwich structures is that they have high bending stiffness, yet they are lightweight compared with metallic structures owing to low material density of the core.

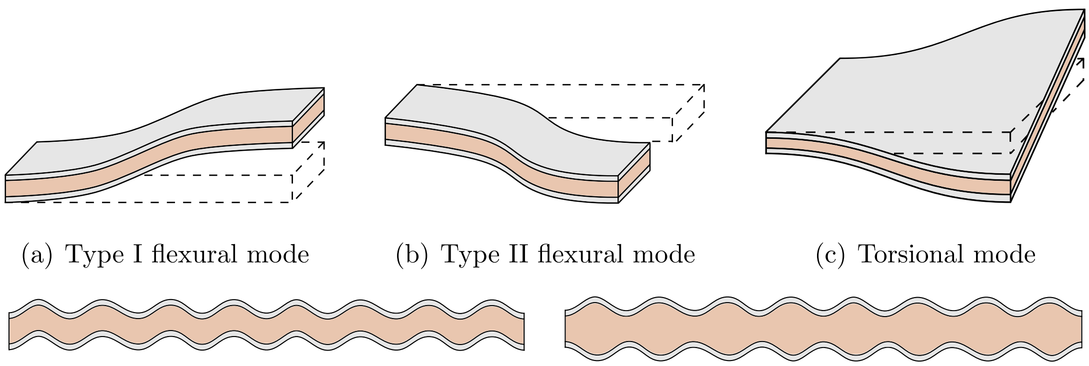

(a) Type I flexural mode (b) Type II flexural mode (c) Torsional mode

(d) Antisymmetric wrinkling mode (e) Symmetric wrinkling mode

Fig. 1.6. Global and local (wrinkling) buckling modes of sandwich structures.

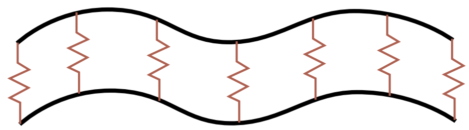

(a) Antisymmetric wrinkling mode

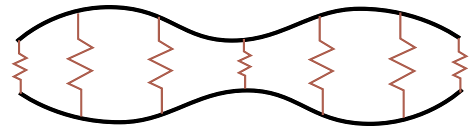

(b) Symmetric wrinkling mode

Fig. 1.7. The Wrinkler foundation model.

Sandwich structures are prone to buckling under compressive loads or bending moments. The uniqueness of buckling analysis of sandwich structures is due to the fact that the buckling behavior of sandwich structures can be entirely different from the buckling behavior of classical laminated structures. In addition to the standard overall buckling modes, sandwich often exhibit local (wrinkling) modes with a wavelength that is much smaller than the in-plane dimensions. Accurate and effective predictions of buckling loads and associated buckling modes are vital to the design and optimization of sandwich structures. The buckling modes are seen in two categories, namely global buckling modes and local buckling (wrinkling) modes. The global buckling modes comprise the type I flexural mode (Fig. 1.6(a)), the type II flexural mode (Fig. 1.6(b)) and the torsional mode (Fig. 1.6(c)); the local buckling modes consist of the antisymmetric wrinkling mode (Fig. 1.6(d)) and the symmetric wrinkling mode (Fig. 1.6(e)). While the type I flexural mode and the local modes are well predicted by many approaches such as [17, 63–65], the type II flexural mode and the torsional mode are rarely seen and mentioned in literature.

Early approaches are based on simplified models that each has different assumptions for the core. They are the Winkler foundation model [66], the Hoff and Mautner's model [67], the Plantema's approach [68] and the Allen's approach [69] to name a few. The Winkler foundation model states that the core supports the skins as an array of continuously distributed linear springs as shown in Fig. 1.7. The critical load in flange is

$$P_{\text{cr,Winkler}} = \sqrt{\frac{2E_f t_f E_c}{3t_c}} \tag{1.1}$$

where E_f and E_c are the Young's modulus of flange and core respectively, t_f and t_c are the flange and core thickness respectively. What makes this model unreliable is that it does not consider the shear in core. This is only reasonable if the core has a very low shear modulus. The Hoff and Mautner's model takes into account the shear effect. The formula to compute critical load by Hoff and Mautner is simple and still widely used in industry today. The critical load in flange is

$$P_{\text{cr,Hoff}} = 0.91\sqrt[3]{E_f E_c G_c} \tag{1.2}$$

and the wrinkling wavelength is

$$L_{\text{Hoff}} = 3.3 t_f \sqrt[6]{\frac{E_f^2}{E_c G_c}} \tag{1.3}$$

Hoff suggests that a 0.5 coefficient should be use in Eq. (1.2) for practical use. The drawback of this model is that it is independent of sandwich geometry and the stress field in core does not satisfy the 2D stress equilibrium. The Plantema's approach extends the Hoff and Mautner's approach by including the skin bending stiffness into the energy formulation. In Allen's approach, the shear stress is derived from an Airy stress function thus it overcomes the drawbacks of aforementioned approaches. The critical load in flange under uniaxial compression is

$$P_{\text{cr,Allen}} = \sqrt[3]{\frac{9E_f E_c^2}{4(3-\nu_c)^2(1+\nu_c)^2}} \tag{1.4}$$

and the wrinkling wavelength is

$$L_{\text{Allen}} = 2\pi t_f \sqrt[3]{\frac{(3-\nu_c)(1+\nu_c)E_f}{12(1-\nu_f^2)E_c}} \tag{1.5}$$

For Poisson's ratio of core $\nu_c = 0.3$, the critical load by Allen reduces to

$$P_{\text{cr,Allen}} = 0.78\sqrt[3]{E_f E_c G_c} \tag{1.6}$$

which is very close to the Hoff's equation in Eq. (1.2). In a nutshell, the basic idea of these classical approaches is that the faces are treated as infinite plates resting on an elastic media, and this idea continues in more refined analytical techniques nowadays. A more detailed overview of the classical approaches is given by Fagerberg [70].

Unified approaches based on various assumptions regarding the kinematics of the core and the skins have been proposed to study instabilities of sandwich structures over the recent decades. Frostig et al. developed a higher-order sandwich panel theory (HSAPT) [71]. The theory modeled the skins as Euler–Bernoulli beams and modeled the core using 2D elasticity theory. Shear stress in the core was assumed to be constant. The theory was applied to study buckling behaviors of sandwich structures but only considered the global and symmetric wrinkling modes [21, 22]. Phan et al. developed an extended HSAPT by taking the in-plane rigidity of the core into consideration [72] and showed that using the extended HSAPT resulted in more accurate buckling predictions for both soft and stiff cores than using the HSAPT [73, 74]. Leotoing et al. modeled sandwich structures using a layerwise theory and provided closed-form formulas for critical loads of global buckling and local wrinkling modes [63]. The skins were modeled as Euler–Bernoulli beams and the core kinematics was expressed in polynomial functions. It is noted that a linear distribution of transverse shear stress was assumed. The method was later extended to study the post-buckling of sandwich structures that considered elastoplastic behavior of the core material [75]. Douville and Le Grognec [17] modeled the face sheets as Euler–Bernoulli beams and modeled the core as a 2D continuous solid satisfying the plane stress assumption. They provided formulas for critical displacements of sandwich columns in compression but did not provide formulas for those in bending. Theoretical studies on instabilities of sandwich structures in bending can also be seen in [76]. Later Saoud and Le Grognec developed a one-dimensional (1D) finite element model for the buckling analysis of sandwich structures [77]. Both frameworks were then extended to study post-buckling behaviors of sandwich structures using the arc-length method and considered the plasticity [78, 79]. In contrast to Leotoing et al. [75] in which plastic deformation only occurred during post-buckling responses, Le Grognec et al [78] showed the onset of buckling as the core already behaved plastically.

The model in [77] assumed a Timoshenko beam theory for the skin kinematics. In contrast, Hu et al. [80] in its 1D FE model assumed a Euler–Bernoulli beam theory for the skin kinematics. Several selected 1D FE models were evaluated in studying global and local instabilities of sandwich structures, and the effect of associated assumptions regarding the core kinematics on shear deformation of the core was assessed [81]. The results were compared with 2D FEA results which were considered as the reference solutions.

Liu et al. [82] developed a new Fourier-related double-scale method to study interactive buckling of sandwich structures between global and local modes. Slowly varying coefficients in the Fourier series accounted for global instabilities whereas rapid oscillations in shorter wavelengths represented local instabilities. Due to the fact that such periodic responses at the onsets of instabilities are not always valid near boundaries, this model was later extended to capture the boundary effect by using the Arlequin method to couple distinct mechanics at boundaries in a weak sense [83]. Other studies in interactive buckling of sandwich structures can be seen in [84, 85]. A review of the development in the modeling and buckling analysis of sandwich structures was given by Hohe and Librescu [86].

1.3 Literature review on Bloch wave theory

One of the FE techniques to simulate local buckling is to perform representative volume element (RVE) analysis with periodic boundary conditions (PBC) [87]. However, onsets of local buckling may break the periodicity into a new periodic pattern. Figure 1.8 shows the break of periodicity of a stiffened panel into a group of 4 unit cells (2×2) at onset of local buckling. For a single unit cell, the displacements at periodic boundaries do not satisfy PBC.

A recent interest in using Bloch wave theory to study local buckling in periodic structures arises. Bloch wave is a wave function in describing a particle in a periodically-repeating environment, most commonly seen in describing the energy

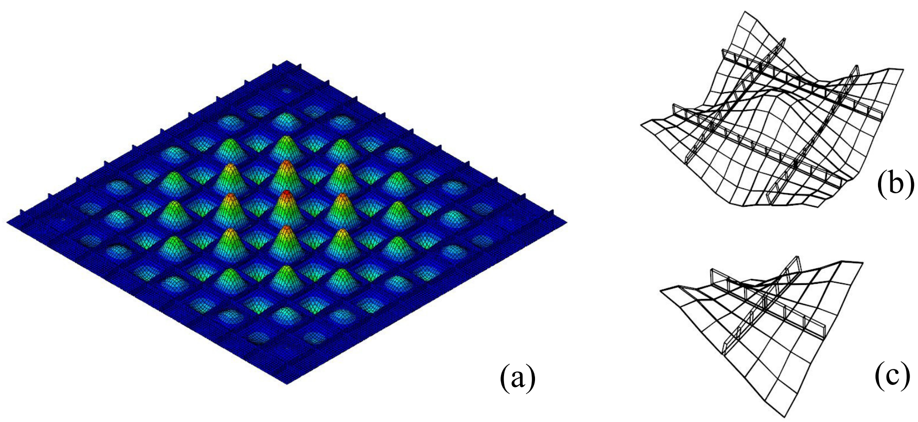

Fig. 1.8. The break of periodicity at onset of local buckling. (a) A local buckling mode of a stiffened panel. (b) The periodicity consists of 2×2 unit cells. (c) Buckling mode of one unit cell showing aperiodic boundary conditions.

potentials of electrons in crystals in quantum mechanics [88]. The connection between Bloch wave theory and local buckling study was first established by Geymonat et al. [89]. Subsequent work by Triantafyllidis et al. [90–92], Ning and Pellegrino [93], Wang and Abdalla [43], Do and Le Grognec [94] and Bertoldi et al. [95–100] showed the Bloch wave representation of local buckling in various studies of periodic structures.

1.4 Motivation

Based on the literature review and discussion above, simplifying assumptions often allowed analytical formulas for the critical load or displacement, however, different configurations or boundary conditions required different formulas. Accuracies of the proposed methods in the literature were assessed ubiquitously by comparing with 2D FEA results, and the accuracies compared with 3D FEA were unclear. Studies of the global buckling of the sandwich panels often assumed that the sandwich structures buckled in column-buckling modes which ruled out plate-buckling modes.

To the best of author's knowledge, there are very few unified approaches capable of studying the buckling of different structures, which motivates the author to develop current method. The main improvements of current method compared with other methods seen in literature are avoiding unnecessary assumptions, the capability of predicting all possible buckling modes including the global and local buckling modes, and the potential of the method in studying the instability of various types of structures.

In this work, the author employed and extended a homogenization theory namely the mechanics of structure genome (MSG) [101] to study the buckling behavior of different structures. MSG is a unified homogenization theory that provides the constitutive modeling of 3D continua, beams, and plates/shells [102–105]. The term *genome* is generalized from the RVE concept in micromechanics. A structure genome (SG) is the smallest mathematical building block of a structure (e.g. cross section of a beam, transverse normal line of a composite laminate, unit cell of a periodic structure) which can be used to compute constitutive relations for macroscopic structure (Fig. 1.9). It is the domain for constitutive modeling to compute the effective structural properties and recover the local stress and strain fields in the original structure. For example, the SG of a prismatic helicopter rotor blade in Fig. 1.9 is the cross section of the rotor blade from which the effective beam properties are computed such as a 4×4 Euler–Bernoulli beam stiffness matrix or a 6×6 Timoshenko beam stiffness matrix. The SG of a laminated plate is a one-dimensional (1D) line featuring the material heterogeneity across the thickness. The SG of a particle-reinforced solid can be represented as a cubic unit cell with a particle in center and one quarter of the hemisphere in each corner whose volume fraction equals to the volume fraction of the particle in solid. As a result, a computationally efficient macroscopic structural analysis replaces the analysis of original structure. MSG bridges the microstructure with the macroscopic structural analysis and provides a unified way to compute effective structural properties for 3D structures, beams, plates and shells in terms of microstructures.

MSG can be used in a variety of applications, yet current work only focuses on applying MSG in buckling analysis of stiffened and sandwich panels. In buckling analysis for global buckling modes, MSG mathematically decouples the original geometrical nonlinear problem into a linear constitutive modeling over the SG and a geometrically nonlinear analysis over the macroscopic model. In the linear constitutive modeling, the effective properties such as the A, B, and D matrices are computed. Then the effective properties are used as equivalent plate properties of plate elements in commercial finite element softwares such as Abaqus to carry out buckling and post-buckling analysis. Lastly, buckling loads/buckling mode shapes and post-buckling curve are predicted on a homogeneous plate with the effective plate properties. Figure 1.10 shows the workflow of MSG in global buckling analysis of stiffened panels.

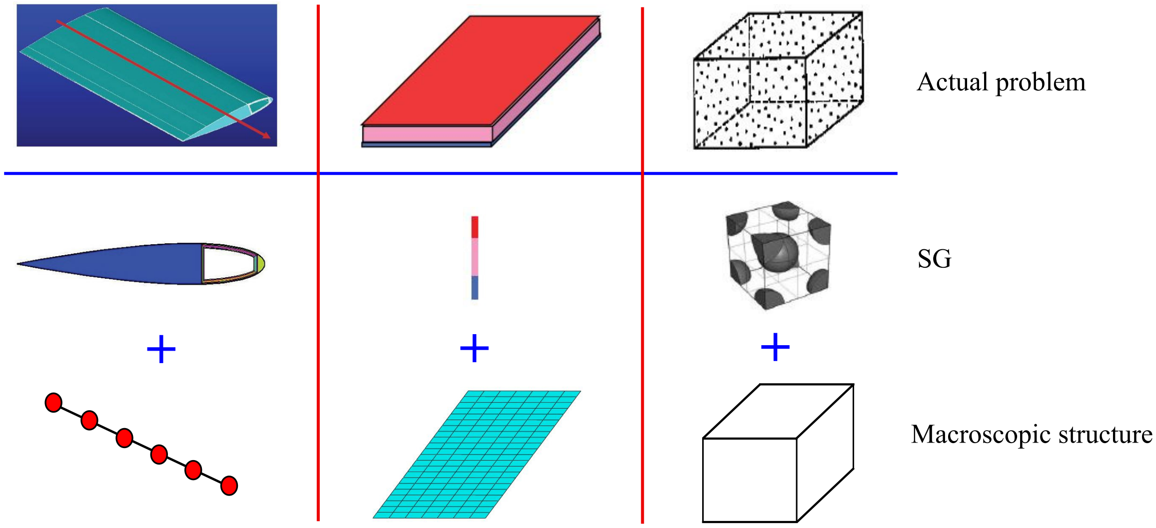

Fig. 1.9. Illustration of the unified homogenization theory: Mechanics of Structure Genome in analysis of beam-like structure, plate-like structure and 3D continua.

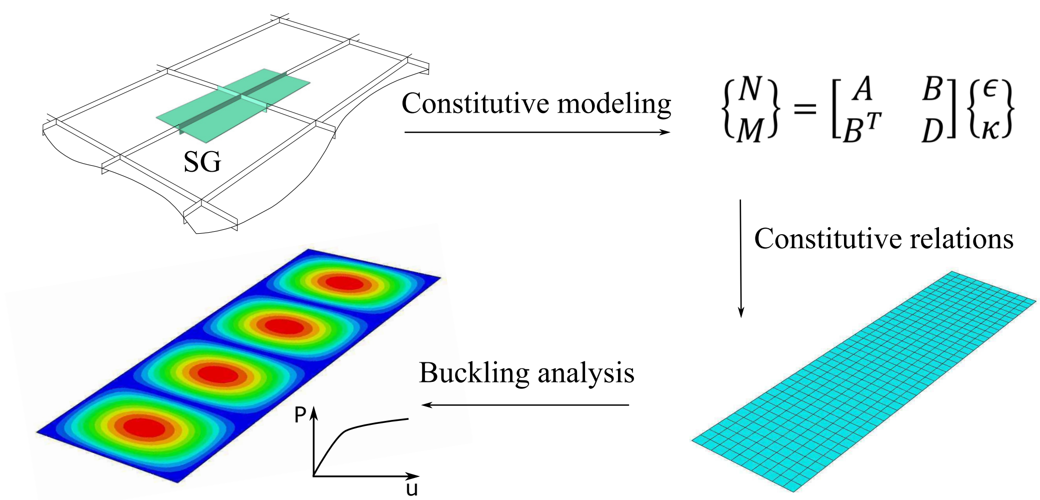

Fig. 1.10. Workflow of MSG in the global buckling analysis of stiffened panels. SG is identified as the repeating unit cell with stiffeners and skins; constitutive modeling is carried out to obtain the constitutive relations; the constitutive relations are used as effective properties of the 2D plate for buckling analysis.

In local buckling analysis, the wavelengthes of the local modes are in general much smaller than those seen in the global modes, therefore finite local rotations have to be accounted in the constitutive modeling. Current work extended MSG by introducing the Saint Venant-Kirchhoff material model and Bloch-periodic boundary condition. Saint Venant-Kirchhoff material model is an extension of the linear elastic material model to the nonlinear regime by using the Green strain. The bifurcation points are found by perturbing the fluctuating functions under the Bloch-periodic boundary condition. The onsets of local instabilities are defined as the singularities of the tangential stiffness matrix such that the perturbed fluctuating function becomes indeterminate.

This thesis is organized as follows. Chapter 2 presents the unified theoretical formulations of MSG and extended MSG in global and local buckling analysis. Chapter 3 presents the validation results and discussions. Chapter 4 summarizes the thesis and points out the potential applications and future work.

2. THEORY

In this chapter, the author presents the theoretical formulations of MSG theory for global buckling analysis and the extended MSG theory for local buckling analysis. The kinematics will be given first from which the deformation gradient is derived. For global buckling analysis, local rotations are small thus a geometrically linear constitutive modeling is constructed using the Biot strain. The global buckling is then predicted on macroscopic structures with effective properties. For local buckling analysis, local rotations become finite thus Green-Lagrange strain measures are used in the constitutive modeling. Newton's method is used to solve the nonlinear equilibrium equations for the fluctuating functions. To find the critical strains for local buckling, the fluctuating functions are perturbed under the Bloch-periodic boundary conditions. The onsets of local buckling are defined as the singularities of tangential stiffness matrix such that the perturbed fluctuating functions become indeterminate. Besides, to predict post-local-buckling behavior, a more robust numerical method, i.e., the arc-length method is introduced to solve the nonlinear equilibrium equations. Although the majority of formulations below are given in terms of the plate model, it nevertheless mean to limit the application of this theory only in studying plate-like structures. Key notes are given for modeling beam-like structures or 3D continua.

2.1 Kinematics

Two sets of coordinates are introduced namely the macro-coordinates x_i and the micro-coordinates y_i. Macro coordinates denote the coordinates in the original structure and the macroscopic structure. Micro coordinates denote the coordinates in the SG. Figure 2.1 illustrates the set-up of the macro-coordinates x_i and the micro-

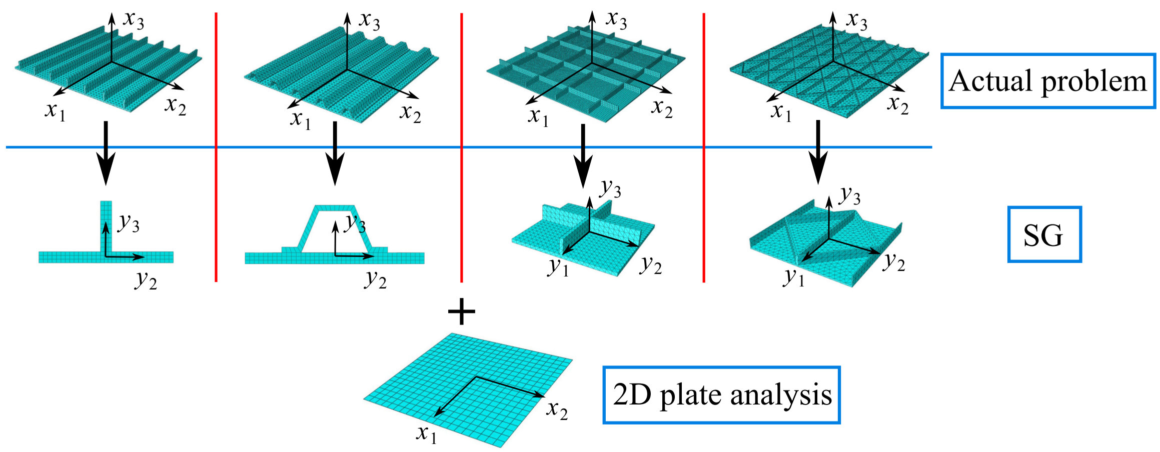

Fig. 2.1. Illustration of the macro-coordinates x_i and the micro-coordinates y_i in actual structures, SG and 2D plate analysis.

coordinates y_i in a plate-like structure that features sufficiently small SGs in the in-plane directions.

If the size of SG is much smaller than dimensions of corresponding macroscopic structure, then we have $y_i = x_i/\varepsilon$ with ε as a small book-keeping parameter. Following Bensoussan et al. [106], the partial derivative of a function $f(x_k, y_j)$ is expressed as

$$\frac{\partial f(x_k, y_j)}{\partial x_i} = \frac{\partial f(x_k, y_j)}{\partial x_i}|_{y_j=\text{const}} + \frac{1}{\varepsilon}\frac{\partial f(x_k, y_j)}{\partial y_i}|_{x_k=\text{const}} \equiv f_{,i} + \frac{1}{\varepsilon} f_{|i} \tag{2.1}$$

Throughout the dissertation, Latin indices assume 1, 2, 3 except that k, l, m assume values corresponding to the macro coordinates that remain in the macroscopic structural model, e.g., 1 for beam model, and 1, 2 for plate model. Greek indices assume values corresponding to the eliminated macro coordinates, e.g., 2, 3 for beam model, and 3 for plate model.

Let $\boldsymbol{b}_k$ denote the unit vector tangent to x_k for the undeformed configuration. We describe the position of any material point of the original structure by its position vector $\boldsymbol{r}$ relative to a point O fixed in an inertial frame such that

$$\boldsymbol{r}(x_k, y_\alpha) = \boldsymbol{r}_o(x_k) + \varepsilon y_\alpha \boldsymbol{b}_\alpha(x_k) \tag{2.2}$$

where $\boldsymbol{r}_o$ is the position vector from O to a material point of the macroscopic model.

In the plate model, we choose $\boldsymbol{b}_3$ to be chosen to be normal to the reference surface spanned by x_k, so we can describe the position of any material point of the original structure by its position vector $\boldsymbol{r}$ relative to a point O fixed in an inertial frame such that

$$\boldsymbol{r}(x_1, x_2, y_3) = \boldsymbol{r}_o(x_1, x_2) + \varepsilon y_3 \boldsymbol{b}_3(x_1, x_2) \tag{2.3}$$

Because x_k is an arc-length coordinate, we have $\boldsymbol{b}_k = \frac{\partial \boldsymbol{r}_o}{\partial x_k}$. Figure 2.2 shows the undeformed and deformed configurations in the plate model.

In the beam model, we choose $\boldsymbol{b}_1$ to be tangent to the beam reference line x_1, and $\boldsymbol{b}_2$, $\boldsymbol{b}_3$ as unit vectors tangent to the cross-sectional coordinates x_2 and x_3. So we can describe the position of any material point of the original structure by its position vector $\boldsymbol{r}$ relative to a point O fixed in an inertial frame such that

$$\boldsymbol{r}(x_1, y_2, y_3) = \boldsymbol{r}_o(x_1) + \varepsilon y_2 \boldsymbol{b}_2(x_1) + \varepsilon y_3 \boldsymbol{b}_3(x_1) \tag{2.4}$$

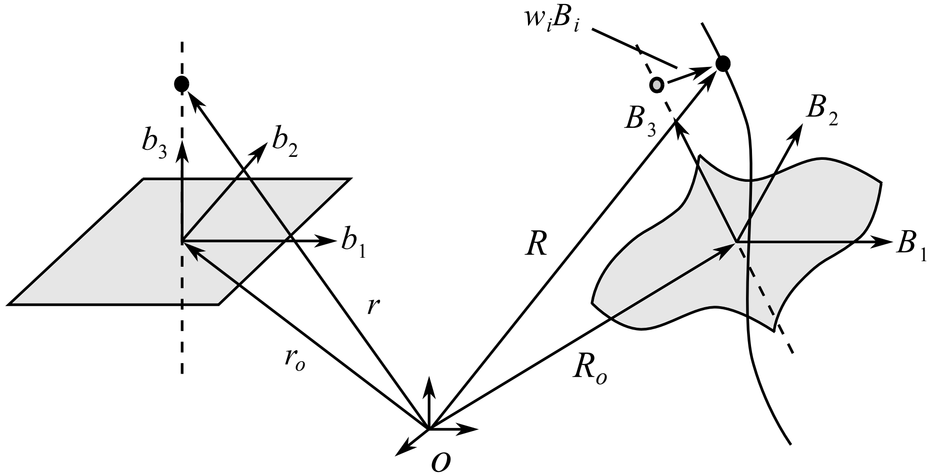

Fig. 2.2. Illustration of fluctuating functions in the deformation of a plate-like structure [107]. They are introduced to accommodate all possible deformations other than those described by $\boldsymbol{R}_o$ and $\boldsymbol{B}_i$.

When the original structure deforms, the particle that had position vector $\boldsymbol{r}$ in the undeformed configuration now has position vector $\boldsymbol{R}$ in the deformed configuration, such as

$$\boldsymbol{R}(x_k, y_j) = \boldsymbol{R}_o(x_k) + \varepsilon y_\alpha \boldsymbol{B}_\alpha(x_k) + \varepsilon w_i(x_k, y_j)\boldsymbol{B}_i(x_k) \tag{2.5}$$

where $\boldsymbol{R}_o$ denotes the position vector of the deformed structure, $\boldsymbol{B}_i$ forms a new orthonormal triad for the deformed configuration. $\boldsymbol{B}_i$ is related to $\boldsymbol{b}_i$ through a direction cosine matrix, $C_{ij} = \boldsymbol{B}_i \cdot \boldsymbol{b}_j$, subject to the requirement that these two triads are the same in the undeformed configuration. εw_i are fluctuating functions introduced to accommodate all possible deformations other than those described by $\boldsymbol{R}_o$ and $\boldsymbol{B}_i$.

In the plate model, the particle that had position vector $\boldsymbol{r}$ in the undeformed configuration now has position vector $\boldsymbol{R}$ in the deformed configuration

$$\boldsymbol{R}(x_1, x_2, y_j) = \boldsymbol{R}_o(x_1, x_2) + \varepsilon y_3 \boldsymbol{B}_3(x_1, x_2) + \varepsilon w_i(x_1, x_2, y_j)\boldsymbol{B}_i(x_1, x_2) \tag{2.6}$$

In the beam model, the particle that had position vector $\boldsymbol{r}$ in the undeformed configuration now has position vector $\boldsymbol{R}$ in the deformed configuration, such as

$$\boldsymbol{R}(x_1, y_j) = \boldsymbol{R}_o(x_1) + \varepsilon y_2 \boldsymbol{B}_2(x_1) + \varepsilon y_3 \boldsymbol{B}_3(x_1) + \varepsilon w_i(x_1, y_j)\boldsymbol{B}_i(x_1) \tag{2.7}$$

Six constraints are needed for Eq. (2.6) to ensure a unique mapping to express $\boldsymbol{R}$ in terms of $\boldsymbol{R}_o$, $\boldsymbol{B}_i$, and w_i. These constraints can be obtained through proper definitions of $\boldsymbol{R}_o$ and $\boldsymbol{B}_i$. If we define

$$\boldsymbol{R}_o = \langle\langle \boldsymbol{R} \rangle\rangle - \langle\langle \varepsilon y_3 \rangle\rangle \, \boldsymbol{B}_3 \tag{2.8}$$

where $\langle\langle \cdot \rangle\rangle$ indicates averaging over the SG. We can obtain three constraints on the fluctuating functions according to Eq. (2.6):

$$\langle\langle w_i \rangle\rangle = 0 \tag{2.9}$$

The other three constraints can be obtained through $\boldsymbol{B}_i$. For a plate/shell-like structure, we can constrain $\boldsymbol{B}_3$ so that

$$\boldsymbol{B}_3 \cdot \boldsymbol{R}_{o,1} = 0, \quad \boldsymbol{B}_3 \cdot \boldsymbol{R}_{o,2} = 0 \tag{2.10}$$

which implies that $\boldsymbol{B}_3$ is chosen to be normal to the reference surface of the deformed plate. It should be noted that this choice has nothing to do with the well-known Kirchhoff hypothesis. In the Kirchhoff assumption, the transverse normal can only rotate rigidly without any local deformation. However, in the present formulation, all possible deformation is allowed by classifying all deformation other than those described by $\boldsymbol{R}_o$ and $\boldsymbol{B}_i$ in terms of the fluctuating function w_i. The last constraint is specified by the rotation of $\boldsymbol{B}_k$ around $\boldsymbol{B}_3$ such that

$$\boldsymbol{B}_1 \cdot \boldsymbol{R}_{o,2} = \boldsymbol{B}_2 \cdot \boldsymbol{R}_{o,1} \tag{2.11}$$

This constraint symmetrizes the macro strains for the plate model as defined in Eq. (2.18) later.

For beam-like structures, we can select $\boldsymbol{B}_\alpha$ in such a way that

$$\boldsymbol{B}_2 \cdot \boldsymbol{R}_{o,1} = 0, \quad \boldsymbol{B}_3 \cdot \boldsymbol{R}_{o,1} = 0 \tag{2.12}$$

which provides two constraints implying that we choose $\boldsymbol{B}_1$ to be tangent to the reference line of deformed beam. Note that this choice is not the well-known Euler-

Bernoulli assumption as the present formulation can describe all deformations of the cross section. We can also prescribe the rotation of $\boldsymbol{B}_\alpha$ around $\boldsymbol{B}_1$ such that

$$\boldsymbol{B}_3 \cdot \frac{\partial \boldsymbol{R}}{\partial x_2} - \boldsymbol{B}_2 \cdot \frac{\partial \boldsymbol{R}}{\partial x_3} = 0 \tag{2.13}$$

which implies the following constraint on the fluctuating functions

$$\langle\langle w_{2|3} - w_{3|2} \rangle\rangle = 0 \tag{2.14}$$

This constraint actually defines the twist angle of the macroscopic beam model in terms of the original position vector.

For structures without initial curvatures, the 3D contravariant base vector of the undeformed configuration namely $\mathbf{g}^a$ coincides with $\boldsymbol{b}_a$ so that the deformation gradient tensor is defined as

$$F_{ij} = \mathbf{B}_i \cdot \mathbf{G}_a \mathbf{g}^a \cdot \mathbf{b}_j = \mathbf{B}_i \cdot \mathbf{G}_j \tag{2.15}$$

where $\mathbf{G}_j$ is the 3D covariant base vector of the deformed configuration. From the deformed configuration in Eq. (2.5), corresponding to the remaining macro coordinate x_k, $\mathbf{G}_k$ is expressed as follows

$$\boldsymbol{G}_k = \frac{\partial \boldsymbol{R}}{\partial x_k} = \frac{\partial \boldsymbol{R}_o}{\partial x_k} + \varepsilon y_\alpha \frac{\partial \boldsymbol{B}_\alpha}{\partial x_k} + \varepsilon \frac{\partial w_i}{\partial x_k} \boldsymbol{B}_i + \varepsilon w_i \frac{\partial \boldsymbol{B}_i}{\partial x_k} \tag{2.16}$$

Corresponding to the eliminated macro coordinate x_α, $\mathbf{G}_\alpha$ is expressed as follows

$$\boldsymbol{G}_\alpha = \frac{\partial \boldsymbol{R}}{\partial x_\alpha} = \boldsymbol{B}_\alpha + \frac{\partial w_i}{\partial y_\alpha} \boldsymbol{B}_i \tag{2.17}$$

A proper definition of the generalized strain measures for the macroscopic structural model is needed for the purpose of formulating the macroscopic structural analysis in a geometrically exact fashion. Following [108–110], we introduce the following definitions:

$$\begin{aligned} \frac{\partial \boldsymbol{R}_o}{\partial x_k} &= \boldsymbol{B}_k + \epsilon_{kl} \boldsymbol{B}_l \\ \frac{\partial \boldsymbol{B}_i}{\partial x_k} &= \kappa_{kj} \boldsymbol{B}_j \times \boldsymbol{B}_i \end{aligned} \tag{2.18}$$

where ϵ_{kl} is the Lagrangian stretch tensor, κ_{kj} is the Lagrangian curvature strain tensor (or the so-called wryness tensor). This definition corresponds to the kinematics of a nonlinear Cosserat continuum. For plate structures, if we impose the constraints given in Eq. (2.11), we will have the symmetry $\epsilon_{12} = \epsilon_{21}$ as a constraint for the kinematics of the plate model. This definition reproduces the 2D generalized strain measures of the Reissner-Mindlin model $\kappa_{kl}^{2\mathrm{D}}$ defined in [109] if we let

$$\kappa_{kl}^{2\mathrm{D}} = \alpha_{lm}\kappa_{km} \qquad \kappa_{k3}^{2\mathrm{D}} = \kappa_{k3} \tag{2.19}$$

with α_{lm} as the 2D permutation symbol: $\alpha_{11} = \alpha_{22} = 0, \alpha_{12} = -\alpha_{21} = 1$. If we further restrain $\boldsymbol{B}_3$ to be normal to the reference surface given in Eq. (2.10), this definition reproduces the 2D generalized strain measures of the Kirchhoff-Love plate model defined in [111]. For beam structures, this definition reproduces the 1D generalized strain measures of the Timoshenko beam model defined in [112]. If we restrict $\boldsymbol{B}_1$ to be tangent to $\boldsymbol{R}_o$ in Eq. (2.12), this definition reproduces the 1D generalized strain measures of the Euler-Bernoulli beam model defined in [112].

Substituting Eq. (2.18) into Eq. (2.16), we can obtain a more detailed expression for the convariant base vectors of the deformed configuration $\mathbf{G}_k$ as follows

$$\boldsymbol{G}_k = \left(\delta_{kl} + \epsilon_{kl} + \varepsilon\frac{\partial w_l}{\partial x_k}\right)\boldsymbol{B}_l + \varepsilon\left[e_{ij\alpha}\left(y_\alpha + w_\alpha\right)\kappa_{kj} + \frac{\partial w_\alpha}{\partial x_k}\delta_{\alpha i} + e_{ijl}w_l\kappa_{kj}\right]\boldsymbol{B}_i \tag{2.20}$$

Substituting Eq. (2.20) into the definition of deformation gradient in Eq. (2.15), we can obtain the deformation gradient without considering initial curvatures. For example, for the plate model, F_{11} is computed as follows

$$\begin{aligned} F_{11} &= \boldsymbol{G}_1 \cdot \boldsymbol{B}_1 \\ &= \delta_{11} + \epsilon_{11} + \varepsilon\frac{\partial w_1}{\partial x_1} + \varepsilon\left[e_{123}(y_3 + w_3)\kappa_{12} + \frac{\partial w_3}{\partial x_1}\delta_{31} + e_{132}w_2\kappa_{13}\right] \\ &= 1 + \epsilon_{11} + \varepsilon\frac{\partial w_1}{\partial x_1} + \varepsilon y_3\kappa_{12} + \varepsilon w_3\kappa_{12} - \varepsilon w_2\kappa_{13} \end{aligned} \tag{2.21}$$

The calculation of other components of deformation gradient are not shown here. Below the author lists the deformation gradient for the plate model after translating the 2D curvatures according to the convention in Eq. (2.19)

$$
\begin{aligned}
F_{11} &= 1 + \epsilon_{11} + \varepsilon y_3 \kappa_{11}^{2\mathrm{D}} + \varepsilon w_{1,1} + w_{1|1} + \varepsilon w_3 \kappa_{11}^{2\mathrm{D}} - \varepsilon w_2 \kappa_{13}^{2\mathrm{D}} \\
F_{12} &= \epsilon_{21} + \varepsilon y_3 \kappa_{21}^{2\mathrm{D}} + \varepsilon w_{1,2} + w_{1|2} + \varepsilon w_3 \kappa_{21}^{2\mathrm{D}} - \varepsilon w_2 \kappa_{23}^{2\mathrm{D}} \\
F_{13} &= w_{1|3} \\
F_{21} &= \epsilon_{12} + \varepsilon y_3 \kappa_{12}^{2\mathrm{D}} + \varepsilon w_{2,1} + w_{2|1} + \varepsilon w_3 \kappa_{12}^{2\mathrm{D}} + \varepsilon w_1 \kappa_{13}^{2\mathrm{D}} \\
F_{22} &= 1 + \epsilon_{22} + \varepsilon y_3 \kappa_{22}^{2\mathrm{D}} + \varepsilon w_{2,2} + w_{2|2} + \varepsilon w_3 \kappa_{22}^{2\mathrm{D}} + \varepsilon w_1 \kappa_{23}^{2\mathrm{D}} \\
F_{23} &= w_{2|3} \\
F_{31} &= \varepsilon w_{3,1} + w_{3|1} - \varepsilon w_1 \kappa_{11}^{2\mathrm{D}} - \varepsilon w_2 \kappa_{12}^{2\mathrm{D}} \\
F_{32} &= \varepsilon w_{3,2} + w_{3|2} - \varepsilon w_1 \kappa_{21}^{2\mathrm{D}} - \varepsilon w_2 \kappa_{22}^{2\mathrm{D}} \\
F_{33} &= 1 + w_{3|3}
\end{aligned} \tag{2.22}
$$

Likewise, we can obtain the deformation gradient for the beam model without considering initial curvatures. For example, F_{11} is computed as

$$
\begin{aligned}
F_{11} =& \boldsymbol{G}_1 \cdot \boldsymbol{B}_1 \\
=& \delta_{11} + \epsilon_{11} + \varepsilon \frac{\partial w_1}{\partial x_1} \\
&+ \varepsilon \left[e_{132}(y_2 + w_2)\kappa_{13} + e_{123}(y_3 + w_3)\kappa_{12} + \frac{\partial w_2}{\partial x_1}\delta_{21} + \frac{\partial w_3}{\partial x_1}\delta_{31} + e_{1j1} w_1 \kappa_{1j} \right] \\
=& 1 + \epsilon_{11} + \varepsilon \frac{\partial w_1}{\partial x_1} - \varepsilon (y_2 + w_2)\kappa_{13} + \varepsilon (y_3 + w_3)\kappa_{12}
\end{aligned} \tag{2.23}
$$

The deformation gradient components for the beam model without considering initial curvatures are given as follows

$$
\begin{aligned}
F_{11} &= 1 + \epsilon_{11} + \varepsilon w_{1,1} + w_{1|1} - \varepsilon (y_2 + w_2)\kappa_{13} + \varepsilon (y_3 + w_3)\kappa_{12} \\
F_{12} &= w_{1|2} \\
F_{13} &= w_{1|3} \\
F_{21} &= \varepsilon w_{2,1} + w_{2|1} - \varepsilon (y_3 + w_3)\kappa_{11} + \varepsilon w_1 \kappa_{13} \\
F_{22} &= 1 + w_{2|2} \\
F_{23} &= w_{2|3} \\
F_{31} &= \varepsilon w_{3,1} + w_{3|1} + \varepsilon (y_2 + w_2)\kappa_{11} - \varepsilon w_1 \kappa_{12} \\
F_{32} &= w_{3|2} \\
F_{33} &= 1 + w_{3|3}
\end{aligned} \tag{2.24}
$$

2.2 Formulation for the global buckling analysis

If we constrain ourself to the global buckling admitted by small local rotations, the 3D strain can be approximated as the Biot strain defined in Ref. [101] according to the decomposition of rotation tensor [113], that is

$$\Gamma_{ij} = \frac{1}{2}(F_{ij} + F_{ji}) - \delta_{ij} \tag{2.25}$$

For plate-like structures, substituting the deformation gradient in Eq. (2.22) into the 3D strain field in Eq. (2.25), dropping $\varepsilon w_{i,j}$ and the products of the curvature strains and the fluctuating functions due to the smallness of ε to construct the first approximation, the 3D strain field becomes

$$\begin{aligned}
\Gamma_{11} &= \epsilon_{11} + \varepsilon y_3 \kappa_{11}^{\mathrm{2D}} + w_{1|1} \\
\Gamma_{22} &= \epsilon_{22} + \varepsilon y_3 \kappa_{22}^{\mathrm{2D}} + w_{2|2} \\
\Gamma_{33} &= w_{3|3} \\
2\Gamma_{23} &= w_{2|3} + w_{3|2} \\
2\Gamma_{13} &= w_{1|3} + w_{3|1} \\
2\Gamma_{12} &= 2\epsilon_{12} + 2\varepsilon y_3 \kappa_{12}^{\mathrm{2D}} + w_{1|2} + w_{2|1}
\end{aligned} \tag{2.26}$$

For simplicity, the 3D strain field defined in Eq. (2.26) can be written in the following matrix form

$$\Gamma = \Gamma_h w + \Gamma_\epsilon \bar{\epsilon} \tag{2.27}$$

where $w = \lfloor w_1 \quad w_2 \quad w_3 \rfloor^T$, $\bar{\epsilon} = \lfloor \epsilon_{11} \quad \epsilon_{22} \quad 2\epsilon_{12} \quad \kappa_{11}^{\mathrm{2D}} \quad \kappa_{22}^{\mathrm{2D}} \quad 2\kappa_{12}^{\mathrm{2D}} \rfloor^T$,

$$\Gamma_h = \begin{bmatrix}
\frac{\partial}{\partial y_1} & 0 & 0 \\
0 & \frac{\partial}{\partial y_2} & 0 \\
0 & 0 & \frac{\partial}{\partial y_3} \\
0 & \frac{\partial}{\partial y_3} & \frac{\partial}{\partial y_2} \\
\frac{\partial}{\partial y_3} & 0 & \frac{\partial}{\partial y_1} \\
\frac{\partial}{\partial y_2} & \frac{\partial}{\partial y_1} & 0
\end{bmatrix} \tag{2.28}$$

and

$$\Gamma_\epsilon = \begin{bmatrix} 1 & 0 & 0 & \varepsilon y_3 & 0 & 0 \\ 0 & 1 & 0 & 0 & \varepsilon y_3 & 0 \\ 0 & 0 & 0 & 0 & 0 & 0 \\ 0 & 0 & 0 & 0 & 0 & 0 \\ 0 & 0 & 0 & 0 & 0 & 0 \\ 0 & 0 & 1 & 0 & 0 & \varepsilon y_3 \end{bmatrix} \tag{2.29}$$

If the SG is a lower-dimensional one, one just needs to vanish the term in Γ_h corresponding to the microcoordinates which are not used in describing the SG.

For structures made of linear elastic materials characterized using a 6×6 stiffness matrix C, the strain energy can be written as

$$U = \frac{1}{2} \int \frac{1}{\omega} \langle \Gamma^T C \Gamma \rangle \mathrm{d}\Omega \tag{2.30}$$

where $\langle \bullet \rangle = \int \bullet \mathrm{d}\omega$ denotes the integration over the domain of the SG and ω denotes the volume of the domain spanned by the micro-coordinate y_k corresponding to the remaining coordinates x_k in the macroscopic plate model; Ω denotes the area of the domain in the macroscopic plate model spanned by x_k. It is noted that the introduction of micro-coordinates y_i in SG enables the split of the integral of the strain energy of the original structure into an integral over the SG domain only concerned with the micro-coordinates y_i, and an integral over the plate domain only concerned with the macro-coordinates x_k.

The virtual work done by the applied loads can be calculated as

$$\overline{\delta W} = \int \frac{1}{\omega} \left(\langle \mathbf{p} \rangle \cdot \delta \mathbf{R} + \int_{\mathbf{s}} \mathbf{Q} \cdot \delta \mathbf{R} \mathrm{d}\mathbf{s} \right) \mathrm{d}\Omega \tag{2.31}$$

where s denotes the boundary surfaces of the SG with applied traction force per unit area $\mathbf{Q} = Q_i \mathbf{B}_i$ and applied body force per unit volume $\mathbf{p} = p_i \mathbf{B}_i$, and δ is the Lagrangian variation. It should be noted that the dynamic instability due to the follower loads is beyond the scope of current work and thus is not considered in this work. Substituting the Lagrangian variation of the displacement field in Eq. (2.6) in Eq. (2.31), the virtual work due to applied loads can be expressed as the following

$$\overline{\delta W} = \overline{\delta W}_H + \varepsilon\,\overline{\delta W}^* \tag{2.32}$$

where $\overline{\delta W}_H$ is the virtual work not related with the fluctuating functions w_i and $\overline{\delta W}^*$ is the virtual work related with the fluctuating functions. They are given as follows:

$$\overline{\delta W}_H = \int \left(f_i\overline{\delta q}_i + m_i\overline{\delta\psi}_i\right) \mathrm{d}\Omega, \quad \overline{\delta W}^* = \int \frac{1}{\omega}\left(\langle p_i \delta w_i\rangle + \oint Q_i \delta w_i \mathrm{d}s\right) \mathrm{d}\Omega \tag{2.33}$$

with the generalized forces f_i and moments m_i defined as

$$f_i = \frac{1}{\omega}\left(\langle p_i\rangle + \int Q_i \mathrm{d}s\right), \quad m_i = \frac{e_{i3j}}{\omega}\left(\langle \varepsilon y_3 p_j\rangle + \int \varepsilon y_3 Q_j \mathrm{d}s\right) \tag{2.34}$$

where e_{i3j} is the Levi-Civita symbol. Virtual displacements $\overline{\delta q}_i$ and rotations $\overline{\delta\psi}_j$ are defined as

$$\overline{\delta q}_i = \delta\mathbf{R}_o \cdot \mathbf{B}_i, \quad \delta\mathbf{B}_3 = \overline{\delta\psi}_j \mathbf{B}_j \times \mathbf{B}_3 \tag{2.35}$$

The principle of virtual work states

$$\delta U = \overline{\delta W} \tag{2.36}$$

where U is the strain energy, and $\overline{\delta W}$ is the virtual work done by applied loads. In view of the strain energy in Eq. (2.30) and virtual work in Eq. (2.32), the variational statement in Eq. (2.36) can be rewritten in the following after dropping the virtual work related to the small parameter ε.

$$\int \frac{1}{2\omega}\delta\left\langle \Gamma^T C \Gamma\right\rangle - \left(f_i\overline{\delta q}_i + m_k\overline{\delta\psi}_k\right) \mathrm{d}\Omega = 0 \tag{2.37}$$

Considering the fact that the last term in Eq. (2.37) is not a function of w_i, we can conclude that the fluctuating function is governed by the following variational principle

$$\delta\frac{1}{2}\left\langle(\Gamma_h w + \Gamma_\epsilon \bar{\epsilon})^T C(\Gamma_h w + \Gamma_\epsilon \bar{\epsilon})\right\rangle = 0 \tag{2.38}$$

For simple cases, this variational statement can be solved analytically. However in general this variational principle is solved using numerical techniques such as the finite element method. The fluctuating function w is discretized as

$$w(x_k, y_j) = S(y_j)V(x_k) \tag{2.39}$$

where S denotes standard shape functions, and V denotes nodal values of the fluctuating function. Substituting Eq. (2.39) into Eq. (2.38), we obtain the following discretized version of the strain energy functional

$$U = \frac{1}{2}\left(V^T E V + 2V^T D_{h\epsilon}\bar{\epsilon} + \bar{\epsilon}^T D_{\epsilon\epsilon}\bar{\epsilon}\right) \tag{2.40}$$

The first term represents the contribution from the fluctuating functions, the second term represents the contribution from the interaction of the fluctuating functions and generalized plate strains, and the last term represents the strain energy due to generalized plate strains without any fluctuating functions. The corresponding matrices are defined as

$$E = \left\langle (\Gamma_h S)^T C (\Gamma_h S) \right\rangle, \quad D_{h\epsilon} = \left\langle (\Gamma_h S)^T C \Gamma_\epsilon \right\rangle, \quad D_{\epsilon\epsilon} = \left\langle \Gamma_\epsilon^T C \Gamma_\epsilon \right\rangle \tag{2.41}$$

Minimizing U in Eq. (2.40) gives us the following linear system

$$EV = -D_{h\epsilon}\bar{\epsilon} \tag{2.42}$$

It is seen that V linearly depends on $\bar{\epsilon}$. It is noted that the linear system in Eq. (2.42) is due to the restriction of small local rotations used to define strains in Eq. (2.25). Such a restriction implies that local buckling modes within a SG are excluded. In view of the linear system in Eq. (2.42), the solution can be symbolically written as

$$V = V_0\bar{\epsilon} \tag{2.43}$$

Substituting Eq. (2.43) back into Eq. (2.40), we calculate the strain energy stored in the SG as

$$U = \frac{1}{2}\bar{\epsilon}^T \left(V_0^T D_{h\epsilon} + D_{\epsilon\epsilon}\right)\bar{\epsilon} \equiv \frac{\omega}{2}\bar{\epsilon}^T \bar{D}\bar{\epsilon} \tag{2.44}$$

For the plate model, $\bar{D}$ is 6×6 effective plate stiffness matrix (A, B and D matrices) arranged as follows

$$\begin{Bmatrix} N_{11} \\ N_{22} \\ N_{12} \\ M_{11} \\ M_{22} \\ M_{12} \end{Bmatrix} = \begin{bmatrix} A_{11} & A_{12} & A_{16} & B_{11} & B_{12} & B_{16} \\ A_{12} & A_{22} & A_{26} & B_{12} & B_{22} & B_{26} \\ A_{16} & A_{26} & A_{66} & B_{16} & B_{26} & B_{66} \\ B_{11} & B_{12} & B_{16} & D_{11} & D_{12} & D_{16} \\ B_{12} & B_{22} & B_{26} & D_{12} & D_{22} & D_{26} \\ B_{16} & B_{26} & B_{66} & D_{16} & D_{26} & D_{66} \end{bmatrix} \begin{Bmatrix} \epsilon_{11} \\ \epsilon_{22} \\ 2\epsilon_{12} \\ \kappa_{11} \\ \kappa_{22} \\ 2\kappa_{12} \end{Bmatrix} \tag{2.45}$$

Substituting the strain energy stored in SG in Eq. (2.44) into Eq. (2.37), we can rewrite the variational statement governing the original structure as

$$\int \left[\delta \left(\frac{1}{2} \bar{\epsilon}^T \bar{D} \bar{\epsilon} \right) - f_i \overline{\delta q}_i - m_k \overline{\delta \psi}_k \right] \mathrm{d}\Omega = 0 \tag{2.46}$$

This variational statement governs the macroscopic plate model as it only concerns the 2D field variables in terms of the macro-coordinates x_k. Therefore for global buckling with small local rotations, a geometrically nonlinear 3D formulation defined in Eq. (2.37) is mathematically reduced into a geometrically linear constitutive modeling over SG in Eq. (2.42) and a geometrically nonlinear 2D plate formulation in Eq. (2.46). In other words, a 2D plate represents the original 3D structure in the global buckling analysis and the buckling behavior can be predicted using a 2D plate analysis.

2.3 Formulation for the local buckling analysis

In comparison with global buckling modes, local buckling modes feature wavelengthes that are much smaller than wavelengthes of global buckling modes. Thus local rotations should not be considered as small in local buckling modes. To account for the finite local rotations, geometrical nonlinearity is necessary in constitutive modeling. The Saint Venant-Kirchhoff material model is used for this purpose. The Saint Venant-Kirchhoff material model is an extension of the linearly elastic material model to the nonlinear regime by using the Green-Lagrange strain. The Green-Lagrange strain is defined as

$$E_{ij} = \frac{1}{2}(F_{ki}F_{kj} - \delta_{ij}) \tag{2.47}$$

The strain energy density of the Saint Venant-Kirchhoff material is defined as

$$U = \frac{1}{2}E^T D E \tag{2.48}$$

where D is the second elasticity tensor. The first Piola-Kirchhoff stress can be calculated as

$$P_{ab} = \frac{\partial U}{\partial F_{ab}} = \frac{\partial U}{\partial E_{ij}}\frac{\partial E_{ij}}{\partial F_{ab}} = F_{ai}D_{ibkl}E_{kl} \tag{2.49}$$

and the second Piola-Kirchhoff stress can be obtained in a similar way. The first elasticity tensor can be calculated as

$$A_{abcd} = \frac{\partial P_{ab}}{\partial F_{cd}} = \delta_{ac}D_{dbkl}E_{kl} + F_{ai}D_{ibdl}F_{cl} \tag{2.50}$$

In view of the plate model, neglecting the drilling curvatures κ_{13} and κ_{23}, and dropping $\varepsilon w_{i,j}$ and the products of the curvature strains and the fluctuating functions due to the smallness of ε to construct the first approximation, the deformation gradient given in Eq. (2.22) can be written in a matrix form as follows

$$F = \Delta + F_\epsilon \bar{\epsilon} + F_h w \tag{2.51}$$

where

$$\begin{aligned}
&F = \begin{bmatrix} F_{11} & F_{12} & F_{13} & F_{21} & F_{22} & F_{23} & F_{31} & F_{32} & F_{33} \end{bmatrix}^T, \\
&\Delta = \begin{bmatrix} 1 & 0 & 0 & 0 & 1 & 0 & 0 & 0 & 1 \end{bmatrix}^T, \\
&\bar{\epsilon} = \begin{bmatrix} \epsilon_{11} & \epsilon_{22} & 2\epsilon_{12} & \kappa_{11}^{2\mathrm{D}} & \kappa_{22}^{2\mathrm{D}} & 2\kappa_{12}^{2\mathrm{D}} \end{bmatrix}^T, \\
&w = \begin{bmatrix} w_1 & w_2 & w_3 \end{bmatrix}^T
\end{aligned}$$

and

$$F_\epsilon = \begin{bmatrix} 1 & 0 & 0 & \varepsilon y_3 & 0 & 0 \\ 0 & 0 & \frac{1}{2} & 0 & 0 & \frac{1}{2}\varepsilon y_3 \\ 0 & 0 & 0 & 0 & 0 & 0 \\ 0 & 0 & \frac{1}{2} & 0 & 0 & \frac{1}{2}\varepsilon y_3 \\ 0 & 1 & 0 & 0 & \varepsilon y_3 & 0 \\ \multicolumn{6}{c}{O_{4\times 6}} \end{bmatrix} \tag{2.52}$$

$$F_h = \begin{bmatrix} \frac{\partial}{\partial y_1} & 0 & 0 \\ \frac{\partial}{\partial y_2} & 0 & 0 \\ \frac{\partial}{\partial y_3} & 0 & 0 \\ 0 & \frac{\partial}{\partial y_1} & 0 \\ 0 & \frac{\partial}{\partial y_2} & 0 \\ 0 & \frac{\partial}{\partial y_3} & 0 \\ 0 & 0 & \frac{\partial}{\partial y_1} \\ 0 & 0 & \frac{\partial}{\partial y_2} \\ 0 & 0 & \frac{\partial}{\partial y_3} \end{bmatrix} \tag{2.53}$$

One can also obtain the matrix form of deformation gradient for the beam model according to Eq. (2.24) as follows

$$F = \Delta + F_\epsilon \bar{\epsilon} + F_h w \tag{2.54}$$

where

$$\begin{aligned} &F = \begin{bmatrix} F_{11} & F_{12} & F_{13} & F_{21} & F_{22} & F_{23} & F_{31} & F_{32} & F_{33} \end{bmatrix}^T, \\ &\Delta = \begin{bmatrix} 1 & 0 & 0 & 0 & 1 & 0 & 0 & 0 & 1 \end{bmatrix}^T, \\ &\bar{\epsilon} = \begin{bmatrix} \epsilon_{11} & \kappa_{11} & \kappa_{12} & \kappa_{13} \end{bmatrix}^T, \\ &w = \begin{bmatrix} w_1 & w_2 & w_3 \end{bmatrix}^T \end{aligned}$$

and

$$F_\epsilon = \begin{bmatrix} 1 & 0 & \varepsilon y_3 & -\varepsilon y_2 \\ 0 & 0 & 0 & 0 \\ 0 & 0 & 0 & 0 \\ 0 & -\varepsilon y_3 & 0 & 0 \\ 0 & 0 & 0 & 0 \\ 0 & 0 & 0 & 0 \\ 0 & \varepsilon y_2 & 0 & 0 \\ 0 & 0 & 0 & 0 \\ 0 & 0 & 0 & 0 \end{bmatrix} \tag{2.55}$$

$$F_h = \begin{bmatrix} \frac{\partial}{\partial y_1} & 0 & 0 \\ \frac{\partial}{\partial y_2} & 0 & 0 \\ \frac{\partial}{\partial y_3} & 0 & 0 \\ 0 & \frac{\partial}{\partial y_1} & 0 \\ 0 & \frac{\partial}{\partial y_2} & 0 \\ 0 & \frac{\partial}{\partial y_3} & 0 \\ 0 & 0 & \frac{\partial}{\partial y_1} \\ 0 & 0 & \frac{\partial}{\partial y_2} \\ 0 & 0 & \frac{\partial}{\partial y_3} \end{bmatrix} \tag{2.56}$$

Fluctuating function w is discretized in the same way as it is in Eq. (2.39).

Again the virtual work in Eq. (2.37) is dropped to construct the first approximation, we obtain

$$\delta\langle U\rangle = \langle \delta F^T P\rangle = \delta V^T \langle (F_h S)^T P\rangle = 0 \tag{2.57}$$

from which the fluctuating function can be determined from

$$\Omega(V) = \langle (F_h S)^T P\rangle = 0 \tag{2.58}$$

To solve the nonlinear equilibrium equation in Eq. (2.58) for the fluctuating functions, Newton's method is used for its simplicity and fast rate of convergence. According to Newton's method, for an initial guess of the fluctuating functions V_0, the increment is found to be

$$\Omega(V_0) + \left(\frac{\partial \Omega}{\partial V}\right)_{V=V_0} dV = 0 \tag{2.59}$$

from which we conclude

$$dV = -\left(\frac{\partial \Omega}{\partial V}\right)^{-1}_{V=V_0} \Omega(V_0) \tag{2.60}$$

and

$$\frac{\partial \Omega}{\partial V} = \langle (F_h S)^T A (F_h S)\rangle \tag{2.61}$$

One can iteratively solve for the incremental fluctuating functions until a convergence criterion is met. Eventually the fluctuating functions that minimize the total potential energy for a given strain $\bar{\epsilon}$ is $V^* = V_0 + \sum dV$. It should be noted that Newton's method will fail to converge once the tangent stiffness in Eq. (2.61) becomes singular. In that case, methods such as the arc-length method should be used to solve for the fluctuating functions.

Once the fluctuating functions are found, we proceed to find the bifurcated fluctuating functions. The onsets of instabilities indicate that there is more than one equilibrium solution to Eq. (2.58) meaning that V^* is not the only solution. To find the other solutions, we now find an additional fluctuating function dV under the Bloch-periodic boundary conditions. The reason why we use the Bloch-periodic boundary conditions is that the periodicity of the deformation at onsets of instabilities may not necessarily follow the periodicity of the SG. To account for all possible periodic patterns at onsets of instabilities, we use the Bloch-periodic boundary conditions with different Bloch wave numbers to represent different periodicities of buckling mode shapes.

For a SG shown in Fig. 2.3, the additional fluctuating function dV is constrained under the Bloch-periodic boundary conditions as follows

$$\begin{aligned} dV_{DC} &= dV_{AB} \cdot e^{i2\pi n_1} \\ dV_{BC} &= dV_{AD} \cdot e^{i2\pi n_2} \end{aligned} \tag{2.62}$$

where dV_{DC} is the additional fluctuating function at edge DC and so forth, i is the imaginary unit, n_1 and n_2 are the Bloch wave numbers in y_1 and y_2 directions respectively.

In view of the Bloch-periodic boundary conditions given in Eq. (2.62), the additional fluctuating function can be symbolically written as

$$dV = \begin{bmatrix} dV_{AB} \\ dV_{AD} \\ dV_i \\ dV_{DC} \\ dV_{BC} \end{bmatrix} = Q \begin{bmatrix} dV_{AB} \\ dV_{AD} \\ dV_i \end{bmatrix} = Q \cdot dV_{\text{ind}} \tag{2.63}$$

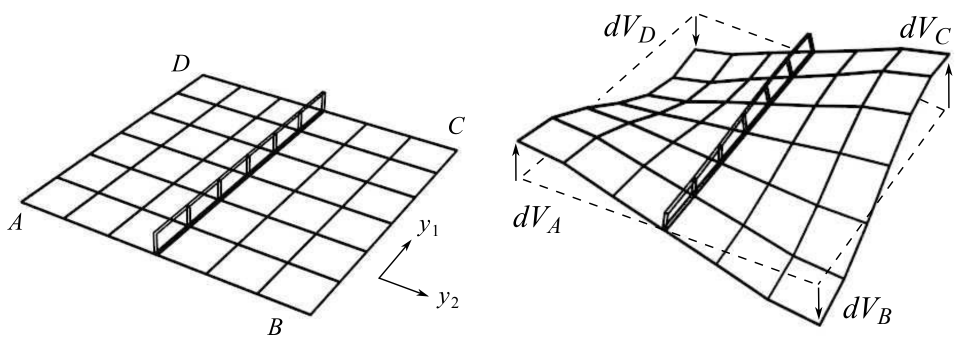

(a) Undeformed (b) Deformed

Fig. 2.3. Example of an undeformed structure genome (SG) and the deformed SG at onset of instabilities .

where dV_i denotes the additional fluctuating function at internal nodes and dV_{ind} denotes the additional fluctuating function at independent nodes. Q is therefore expressed as

$$Q = \begin{bmatrix} I_{AB} & 0 & 0 \\ 0 & I_{AD} & 0 \\ 0 & 0 & I_i \\ e^{i2\pi n_1} I_{AB} & 0 & 0 \\ 0 & e^{i2\pi n_2} I_{AD} & 0 \end{bmatrix} \tag{2.64}$$

where I_{AB} is an identity matrix whose dimension agrees with dV_{AB} and etc.

Substituting Eq. (2.63) into Eq. (2.57), we obtain

$$\delta V_{\text{ind}}^T Q^T \langle (F_h S)^T P \rangle = 0 \tag{2.65}$$

from which we conclude

$$Q^T \langle (F_h S)^T P \rangle = Q^T \Omega(V) = 0 \tag{2.66}$$

Now the Taylor series expansion of Eq. (2.66) in the neighborhood of V^* is

$$Q^T \left(\Omega(V^*) + \left(\frac{\partial \Omega}{\partial V} \right)_{V=V^*} dV \right) = 0 \tag{2.67}$$

Substituting Eq. (2.63) into Eq. (2.67), we get

$$Q^T \left(\Omega(V^*) + \left(\frac{\partial \Omega}{\partial V} \right)_{V=V^*} Q \cdot dV_{\text{ind}} \right) = 0 \tag{2.68}$$

Recall that $\Omega(V^*) = 0$, so Eq. (2.68) becomes

$$\left[Q^T \left(\frac{\partial \Omega}{\partial V} \right)_{V=V^*} Q \right] \cdot dV_{\text{ind}} = 0 \tag{2.69}$$

The only nontrivial solution to Eq. (2.69) is found when the tangent stiffness matrix becomes singular as the following.

$$\det[K] = \det \left[Q^T \left(\frac{\partial \Omega}{\partial V} \right)_{V=V^*} Q \right] = 0 \tag{2.70}$$

The tangent stiffness given in Eq. (2.70) is now a Hermitian matrix whose determinant is a real number. It is also nonlinearly dependent on 2D strain $\bar{\epsilon}$. The Taylor series expansion in the neighborhood of $\bar{\epsilon} = 0$ gives

$$K = K_0 + K_1\bar{\epsilon} + K_2\bar{\epsilon}^2 + ... \tag{2.71}$$

In linear approximation, we keep up to the first order of $\bar{\epsilon}$, which gives

$$K = K_0 + K_1\bar{\epsilon} \tag{2.72}$$

In current work, the author extrapolates the K by finding the $K_{\bar{\epsilon}_1}$ and $K_{\bar{\epsilon}_2}$ of two very small strains $\bar{\epsilon}_1$ and $\bar{\epsilon}_2$ as follows

$$K = K_{\bar{\epsilon}_1} + \lambda(K_{\bar{\epsilon}_2} - K_{\bar{\epsilon}_1}) \tag{2.73}$$

In view of the tangent stiffness matrix given in Eq. (2.73), the instability criterion in Eq. (2.70) becomes

$$\det\Big[K_{\bar{\epsilon}_1} + \lambda(K_{\bar{\epsilon}_2} - K_{\bar{\epsilon}_1})\Big] = 0 \tag{2.74}$$

The local instability problem now becomes an eigenvalue problem. λ is the eigenvalue and the buckling mode shape is the eigenvector. The critical strain can be computed as $\bar{\epsilon}_{cr} = \bar{\epsilon}_1 + \lambda(\bar{\epsilon}_2 - \bar{\epsilon}_1)$. For different Bloch wave numbers n_1 and n_2, we obtain a set of critical strains that represent solutions to Eq. (2.74). The lowest strain among the critical strains is the local buckling strain.

2.4 Formulation for the post-local-buckling analysis

After onsets of buckling, structures enter into post-buckling regime. Structures may or may not have post-buckling load-carrying capabilities depending on many factors such as materials, geometry and boundary conditions. Accurate prediction on post-buckling behavior is vital to assess structures' post-buckling load-carrying capabilities. While Newton's method can be used to solve the nonlinear equilibrium equations in pre-buckling regime, it may fail to converge at onsets of buckling (Fig.

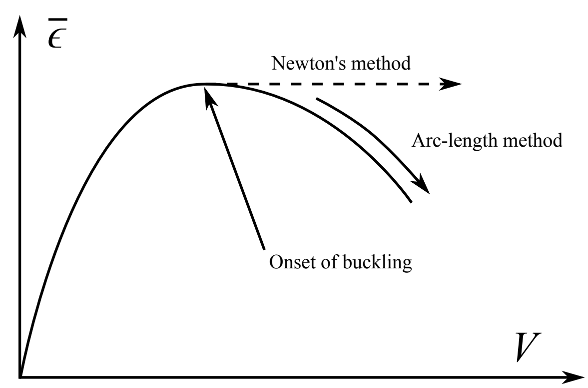

Fig. 2.4. Newton's method fails to converge at onset of buckling for structures having unstable post-buckling configurations. $\bar{\epsilon}$ is the 2D strain and V is the fluctuating function.

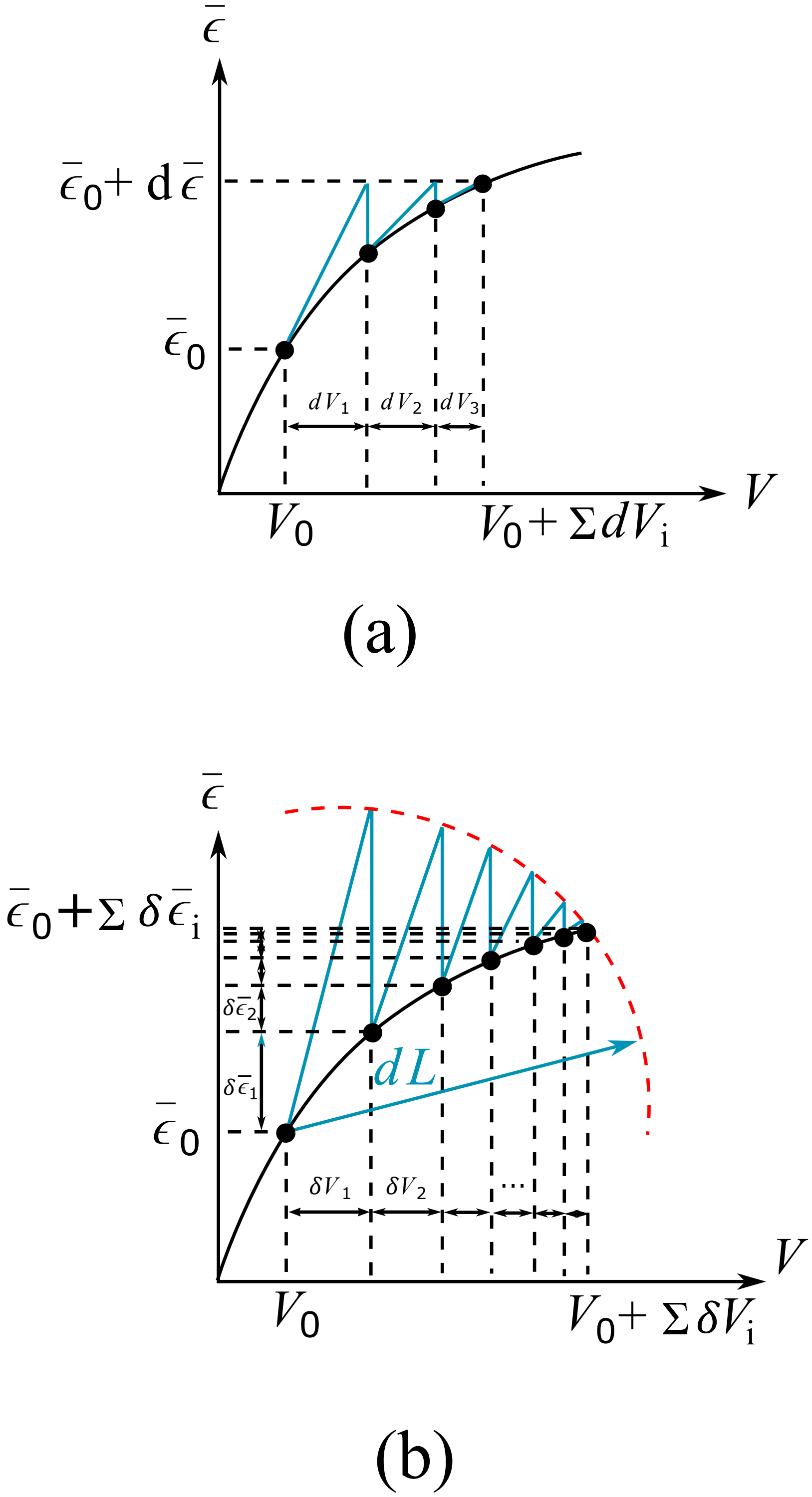

Fig. 2.5. Schematic representations of (a) Newton's method and (b) arc-length method.

2.4). This happens particularly if the post-buckling is unstable: at the onset of buckling, the slope of the curve becomes smaller than or equal to zero. Any small increment in strain $\bar{\epsilon}$ will result in Newton's method failing to trace the post-buckling curve. To overcome this shortcoming, the arc-length method [13,14,114] is introduced to solve the nonlinear equilibrium equations in a more general manner. In contrast to Newton's method which only postulates strain by initiating a strain increment, the arc-length method postulates both strain and fluctuating functions (Fig. 2.5). That is to say, Newton's method considers an incremental strain $d\bar{\epsilon}$ as a priori, and use Taylor series expansion in the neighbourhood of an equilibrium to find its incremental fluctuating functions dV as follows

$$\Omega(V_0 + dV) = \Omega(V_0) + \left.\frac{\partial \Omega}{\partial V}\right|_{V=V_0} \cdot dV = 0 \tag{2.75}$$

In contrast, the arc-length method considers both strains and fluctuating functions as unknowns in Taylor series expansion in the neighbourhood of an equilibrium as follows

$$\Omega(V_0 + dV, \bar{\epsilon}_0 + d\bar{\epsilon}) = \Omega(V_0, \bar{\epsilon}_0) + \left.\frac{\partial \Omega}{\partial V}\right|_{V_0, \bar{\epsilon}_0} \cdot dV + \left.\frac{\partial \Omega}{\partial \bar{\epsilon}}\right|_{V_0, \bar{\epsilon}_0} \cdot d\bar{\epsilon} = 0 \tag{2.76}$$

from which we get

$$\left.\frac{\partial \Omega}{\partial V}\right|_{V_0, \bar{\epsilon}_0} \cdot dV + \left.\frac{\partial \Omega}{\partial \bar{\epsilon}}\right|_{V_0, \bar{\epsilon}_0} \cdot d\bar{\epsilon} = -\Omega(V_0, \bar{\epsilon}_0) \tag{2.77}$$

This will be used later in the numerical recipe in Eq. (2.80). With both strains and fluctuating functions as unknowns, additional constraint is introduced as follows

$$dV^T \cdot dV + \psi^2 d\bar{\epsilon}^T \cdot d\bar{\epsilon} = dL^2 \tag{2.78}$$

where ψ and dL are parameters yet to be defined; ψ defines the ellipticity of the arc shown in Fig. 2.5; dL is the radius to the arc length. In view of equilibrium condition Ω in Eq. (2.58), one can derive $\frac{\partial\Omega}{\partial\bar{\epsilon}}$ as follows

$$\begin{aligned}\frac{\partial\Omega}{\partial\bar{\epsilon}} &= \left\langle \frac{\partial(F_hS)^T}{\partial\bar{\epsilon}}P + (F_hS)^T\frac{\partial P}{\partial\bar{\epsilon}} \right\rangle \\ &= \left\langle \frac{\partial(F_hS)^T}{\partial\bar{\epsilon}}P + (F_hS)^T\frac{\partial P}{\partial F}\frac{\partial F}{\partial\bar{\epsilon}} \right\rangle \\ &= \left\langle \frac{\partial(F_hS)^T}{\partial\bar{\epsilon}}P + (F_hS)^T A(F_\epsilon\delta_{(i)} + \frac{\partial(F_hS)}{\partial\bar{\epsilon}}V) \right\rangle \\ &= \left\langle (F_hS)^T A F_\epsilon \delta_{(i)} \right\rangle\end{aligned} \tag{2.79}$$

With $\frac{\partial\Omega}{\partial V}$ available in Eq. (2.61) and $\frac{\partial\Omega}{\partial\bar{\epsilon}}$ available in Eq. (2.79), one can numerically solve the equilibrium equations in Eq. (2.76) with the constraint in Eq. (2.78).

It is noted that dV as mentioned above is a symbolic variable indicating the incremental fluctuating functions in general. Below we will introduce two new operators Δ and δ particularly for numerical iterations, e.g. ΔV and δV in addition to dV. δV is what we compute in every step of iteration, and ΔV is the sum of increments δV before convergence (δV is small enough). The numerical recipe is given as follows. First, we assume an initial strain $\bar{\epsilon}_0$ and initial fluctuating functions V_0 and solve for the incremental strain $\delta\bar{\epsilon}$ and fluctuating functions δV using Eq. (2.77) as follows

$$\left.\frac{\partial\Omega}{\partial V}\right|_{V_0+\Delta V,\bar{\epsilon}_0+\Delta\bar{\epsilon}} \cdot \delta V + \left.\frac{\partial\Omega}{\partial\bar{\epsilon}}\right|_{V_0+\Delta V,\bar{\epsilon}_0+\Delta\bar{\epsilon}} \cdot \delta\bar{\epsilon} = -\Omega(V_0+\Delta V, \bar{\epsilon}_0+\Delta\bar{\epsilon}) \tag{2.80}$$

It is noted that ΔV and $\Delta\bar{\epsilon}$ are null at the first step of iteration. Equation (2.80) can also be written as follows

$$\begin{aligned}\delta V &= -K_T^{-1}\cdot\Omega - K_T^{-1}\cdot\frac{\partial\Omega}{\partial\bar{\epsilon}}\cdot\delta\bar{\epsilon} \\ &= \delta\bar{V} + \delta\bar{\bar{V}}\cdot\delta\bar{\epsilon}\end{aligned} \tag{2.81}$$

with $K_T = \frac{\partial\Omega}{\partial V}$, $\delta\bar{V} = -K_T^{-1}\cdot\Omega$, $\delta\bar{\bar{V}} = -K_T^{-1}\cdot\frac{\partial\Omega}{\partial\bar{\epsilon}}$. The incremental strain $\delta\bar{\epsilon}$ and fluctuating functions δV are constrained under Eq. (2.78) as follows

$$(\Delta V + \delta V)^T\cdot(\Delta V + \delta V) + \psi^2(\Delta\epsilon + \delta\epsilon)^T\cdot(\Delta\epsilon + \delta\epsilon) = \Delta L^2 \tag{2.82}$$

Now we have two equations Eq. (2.81) and Eq. (2.82) for two unknowns $\delta\bar{\epsilon}$ and δV. To solve for two unknowns, substitute Eq. (2.81) into Eq. (2.82), one obtains

$$a \cdot \delta\bar{\epsilon}^2 + b \cdot \delta\bar{\epsilon} + c = 0 \tag{2.83}$$

with

$$\begin{aligned} a &= \delta\bar{\bar{V}}^T \cdot \delta\bar{\bar{V}} + \psi^2 \\ b &= 2(\Delta V + \delta\bar{V})^T \cdot \delta\bar{\bar{V}} + 2\psi^2 \Delta\epsilon \\ c &= (\Delta V + \delta\bar{V})^T \cdot (\Delta V + \delta\bar{V}) + \psi^2 \Delta\epsilon^2 - \Delta L^2 \end{aligned} \tag{2.84}$$

Now Eq. (2.83) has one unknown $\delta\bar{\epsilon}$ only so we can solve the equation for $\delta\bar{\epsilon}$ and then substitute $\delta\bar{\epsilon}$ into Eq. (2.81) for δV. This marks the finish of one iteration step. For every $\delta\bar{\epsilon}$ and δV obtained in an iteration step, one update the $\Delta\bar{\epsilon}$ and ΔV by adding $\delta\bar{\epsilon}$ and δV into them until $\delta\bar{\epsilon}$ and δV are small enough (converged). If they are converged, it means that we find an equilibrium solution $(\bar{\epsilon}_0 + \Delta\bar{\epsilon}, V_0 + \Delta V)$. To find a new equilibrium solution, one can add $\Delta\bar{\epsilon}$ and ΔV to $\bar{\epsilon}_0$ and V_0 respectively, and start a new loop at Eq. (2.80). Meanwhile, one can adjust ΔL for a proper searching radius in the new loop. Eventually the equilibrium solutions together pave the equilibrium path namely the post-buckling path. Figure 2.6 summarizes the workflow of the arc-length method in MSG theory.

It is noted that the author does not introduce Bloch-periodic boundary conditions in the post-local-buckling analysis in current work. In other words, the purpose of introducing arc-length method into MSG theory is to replace the Newton's method with a more robust nonlinear solver. In the following studies, the post-local-buckling analysis of sandwich structures is established after eigenvalue buckling using Eq. (2.74) from which the author finds the buckling wavelength and then creates a new SG with the size equal to the buckling wavelength.

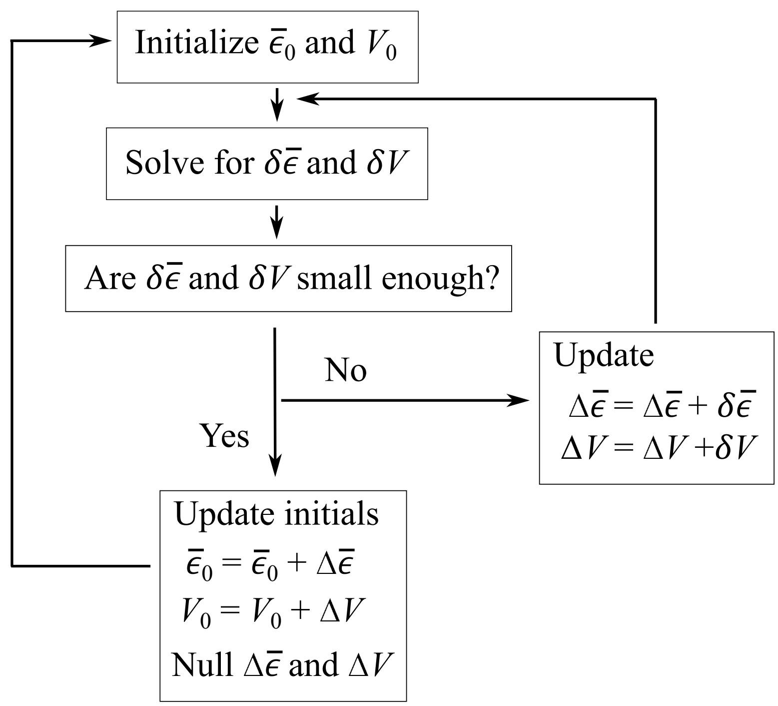

Fig. 2.6. Workflow of the arc-length method.

3. RESULTS AND DISCUSSION

Current method is evaluated for the global buckling and local buckling analysis of stiffened panels and sandwich structures. Results are compared with direct numerical solutions (DNS) in Abaqus using 20-noded 3D elements with reduced integration (C3D20R). Uniaxial compressive loads are applied at the short edges, and all edges are simply supported meaning that their out-of-plane deflection is constrained. First, the MSG theory is evaluated in the global buckling analysis of stiffened panels; both the linearized buckling and post-buckling behavior of stiffened panels are studied to validate this method. Buckling of stiffened panels with various stiffener-grid patterns and under various boundary conditions is also studied. Then the extended MSG theory is evaluated in the local buckling of stiffened panels. Various types of local buckling are studied such as skin buckling, stiffener buckling and interactive buckling. Next, the MSG and extended theory are evaluated in the global and local buckling analysis of sandwich structures. Both the global (type I & II flexural, torsion) and local buckling modes are compared with DNS. Parametric studies are performed to reveal the relative influence of selective parameters on the critical displacements. Current method is also validated in the post-local-buckling of sandwich structures. Next section illustrates how to implement the Bloch wave theory in commercial finite element softwares for RVE analysis. Lastly, the author provides the results of using the extended MSG theory in the beam model in local buckling analysis of sandwich structures. Copyright permissions have been obtained to reuse the published materials from [23] in the following sections.

3.1 Global buckling of stiffened panels

The representative cell having skin and stiffeners (Fig. 1.10) is homogenized using MSG to obtain the effective plate properties, i.e., the A, B and D matrices. Then the effective plate properties are used as the constitutive relations for a plate using plate elements in commercial finite element softwares such as Abaqus shell elements (S8R5). The linearized buckling loads, buckling mode shapes and post-buckling curves are predicted using the plate analysis.

3.1.1 Buckling of a blade-stiffened composite panel

A blade-stiffened composite panel (Fig. 1.5(a)) is studied to validate the MSG theory for global buckling. This stiffened plate is 6.3 m long, 2.52 m wide. Each stiffener covers 0.28 m wide skin. The skin is 1 mm thick. The stiffeners are 20 mm tall, 3 mm thick. Laminate layup of the skin is $[0/90]_s$. Laminate layup of the stiffeners is $[(45/-45)_2 0_2]_s$. Lamina material properties are $E_1 = 113$ GPa, $E_2 = E_3 = 9$ GPa, $G_{12} = G_{13} = 3.82$ GPa, $G_{23} = 3.46$ GPa, $\nu_{12} = \nu_{13} = \nu_{23} = 0.302$.

The effective plate properties, i.e., the A, B and D matrices are computed using MSG and are given in Table 3.1. The first six buckling modes including buckling loads and mode shapes are compared and presented in Table 3.2. It is seen that current solution is highly accurate compared with the DNS results with errors less than 2%. To visualize the difference between the buckling mode shapes of current approach and DNS, an image analysis is carried out by comparing the intensity value of each pixel in corresponding grayscale images of the contour plots that contain values in the range 0 (black) to 1 (white). The difference of the intensity value of pixels is shown in Fig. 3.1. It is found that the vast majority of the area in these contour plots is in complete agreement showing the high accuracy of current method in predicting buckling mode shapes.

Table 3.1.
The effective plate properties (A, B, and D matrices) of the blade stiffened composite plate, units: SI.

$$\begin{bmatrix} 7.1591\times10^{7} & 2.7382\times10^{6} & 0 & -2.6171\times10^{4} & -5.0719\times10^{3} & 0 \\ & 6.1469\times10^{7} & 0 & -5.0719\times10^{3} & -1.1389\times10^{5} & 0 \\ & & 3.8424\times10^{6} & 0 & 0 & -7.0551\times10^{3} \\ & & & 1.3147\times10^{3} & 9.6382 & 0 \\ & sym. & & & 212.8817 & 0 \\ & & & & & 16.7350 \end{bmatrix}$$

Table 3.2.
Comparison of first six buckling loads (N) and mode shapes in the case of the blade-stiffened composite plate. Mesh is removed for clear view.

Mode number	MSG	DNS	Error
1	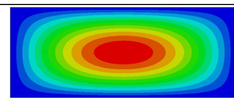 929.63	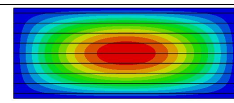 931.45	-0.20%
2	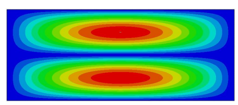 1798.90	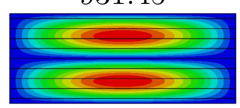 1809.11	-0.56%
3	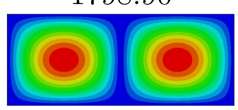 3348.32	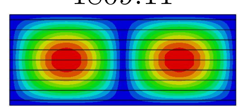 3300.98	1.43%
4	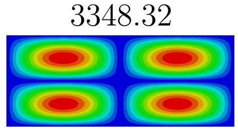 3742.96	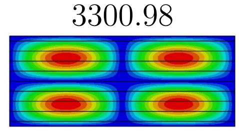 3698.59	1.20%
5	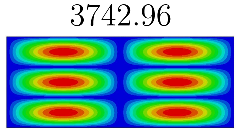 4835.88	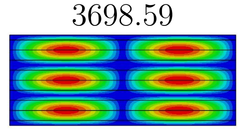 4801.57	0.71%
6	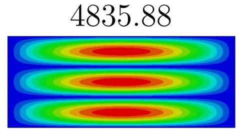 5009.26	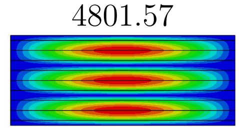 5034.19	-0.50%

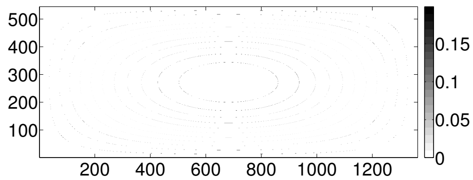

(a) Mode 1

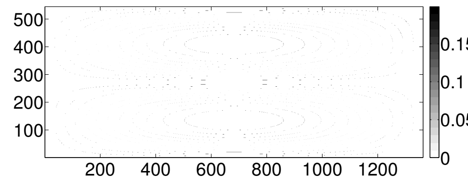

(b) Mode 2

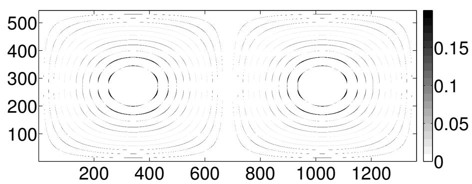

(c) Mode 3

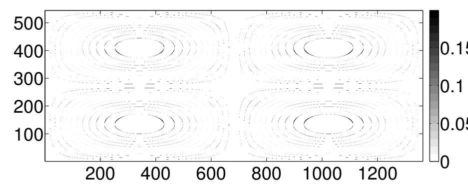

(d) Mode 4

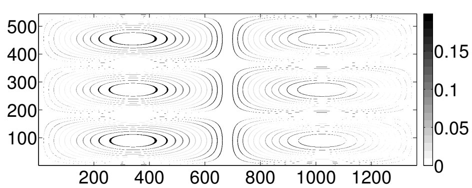

(e) Mode 5

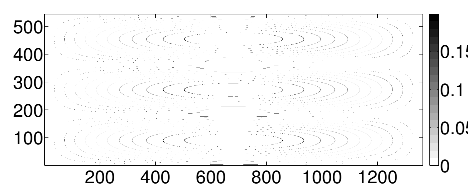

(f) Mode 6

Fig. 3.1. Comparison of the intensity value of each pixel in corresponding grayscale images of the contour plots showing the difference between buckling mode shapes predicted by MSG and DNS for the first six buckling modes. The horizontal and vertical axes are the x_1-x_2 coordinates of the pixels, respectively.

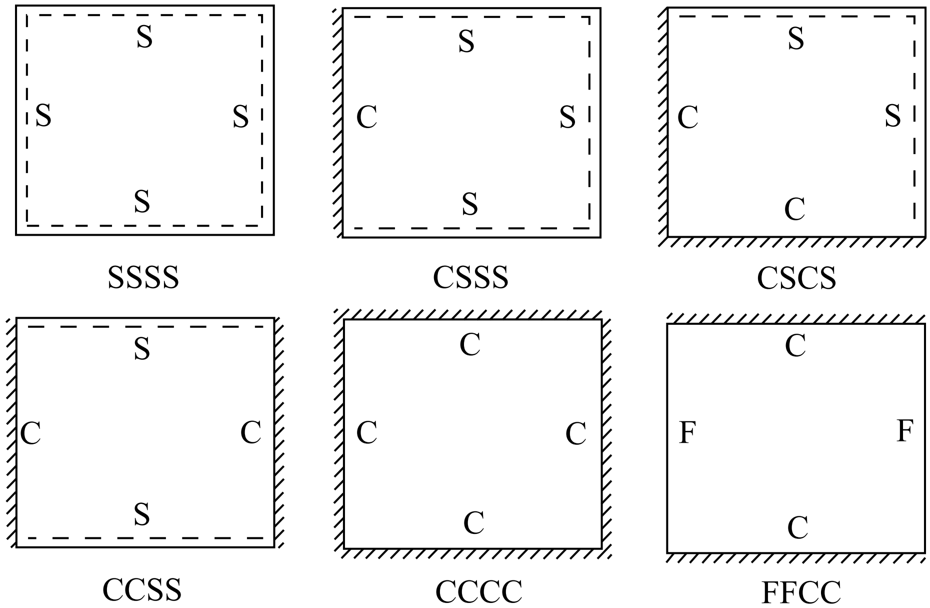

Fig. 3.2. Typical combinations of different boundary conditions (S: simply supported, C: clamped, F: free).

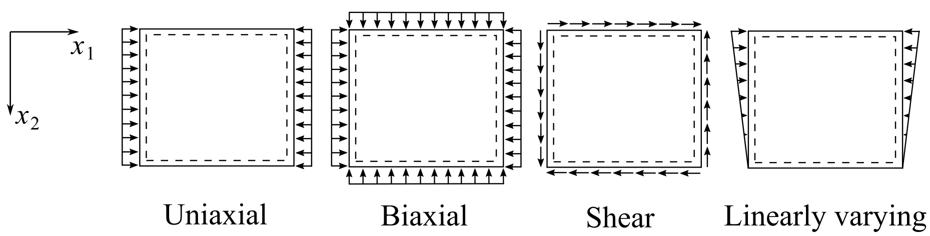

Fig. 3.3. Typical loading conditions.

3.1.2 Buckling under various boundary conditions and loadings

Buckling behaviors of un-stiffened plates under various boundary conditions (BCs) and loadings are studied and seen in [115–118]. However, studies of buckling behavior of stiffened plates under various BCs and loadings are few [119]. Motivated by this fact, the author investigates the buckling behavior of stiffened panels under a variety of BCs and loadings using MSG approach.

Same example of the stiffened panel as in section 3.1.1 is used here. Typical combinations of different BCs are shown in Fig. 3.2. The naming convention starts with the pair of BCs on the vertical edges followed by the pair of BCs on the horizontal edges [120]. For example, CSFS means the platte is clamped at left edge, simply supported at right edge, free at bottom edge and simply supported at top edge. Figure 3.3 shows different loading conditions. In general, the loadings can be expressed as follows [119]:

$$N = \int \lambda \left(1 - \alpha \frac{x_2}{b}\right) dx_2 \tag{3.1}$$

where $\alpha = 0$ indicates uniform uniaxial loading, $\alpha = 1$ indicates linearly varying uniaxial loading, and b is the width of the edges where loads apply.

Critical buckling loads and associated mode shapes under various BCs and loadings are presented in Table 3.3. It is expected that the critical buckling loads increase as the BCs make the structure stiffer. It is also observed that clamping the loading edges will significantly increase the buckling loads. CCSS BCs almost double the buckling loading comparing to CSCS BCs. Different loading conditions also affect the critical buckling loads. The biaxial loading state results in a much lower critical load (255.38 N) as opposed to the uniform uniaxial loading state (929.63 N). Under shear loading, the stiffened panel falls into an overall shear pattern without significant shear deformation seen in skin between stiffeners. This is mainly due to the tightness of the space between stiffeners. The required buckling load under linearly varying uniaxial loading (833.62 N) is less than the critical load under uniform uniaxial loading (929.63 N) due to the fact that the structure is not loaded evenly. Image analysis (Fig. 3.4) shows good agreement in predicted buckling mode shapes between MSG and DNS.

3.1.3 Post-buckling analysis

The accuracy of current approach in predicting post-buckling behavior of stiffened composite plate is investigated in this section. Post-buckling is referred to the behavior after the buckling of plate takes place. Riks method [13, 14] is used in current

Table 3.3.
Investigation of critical buckling of the blade stiffened composite panel under various boundary conditions and loadings. Loads are in Newton; L.V. is linearly varying uniaxial loading; mesh is removed for clear view.

B.C./Loading	MSG	DNS	Error
SSSS	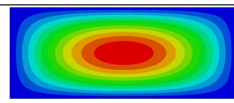 929.63	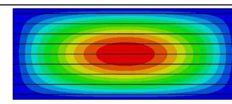 931.45	-0.20%
CSSS	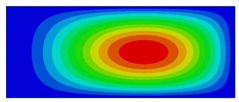 1779.30	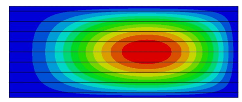 1772.86	0.36%
CSCS	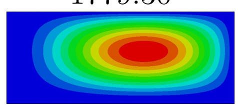 1843.41	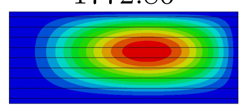 1839.16	0.23%
CCSS	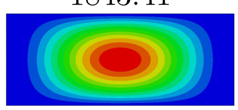 3378.06	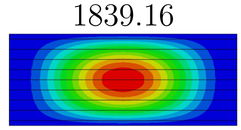 3339.13	1.15%
CCCC	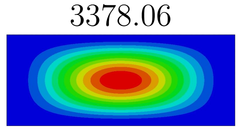 3539.85	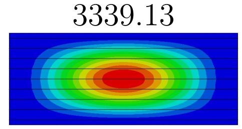 3505.11	0.98%
FFCC	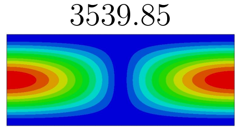 1130.95	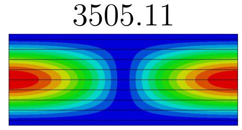 1145.93	-1.32%
Biaxial	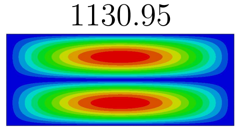 255.38	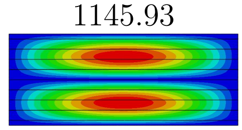 258.45	-1.19%
Shear	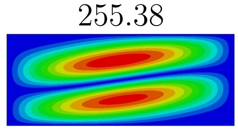 821.97	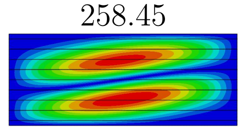 816.69	0.65%
L.V.	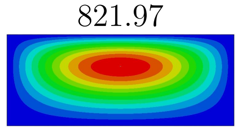 833.62	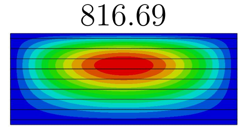 835.66	-0.24%

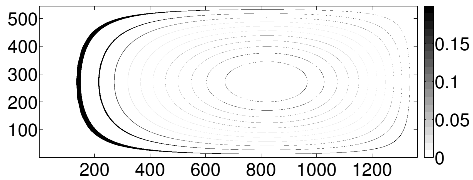

(a) CSSS

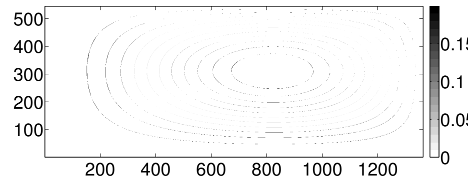

(b) CSCS

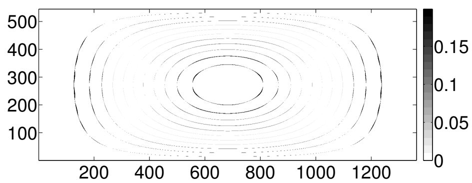

(c) CCSS

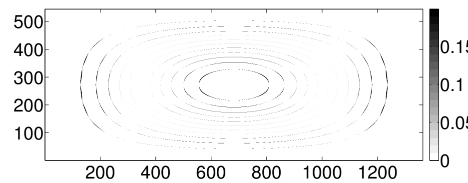

(d) CCCC

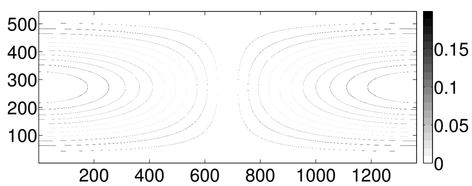

(e) FFCC

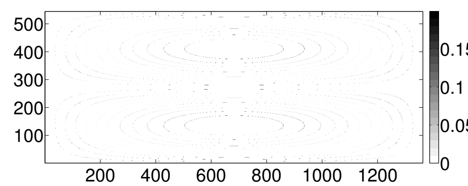

(f) Biaxial

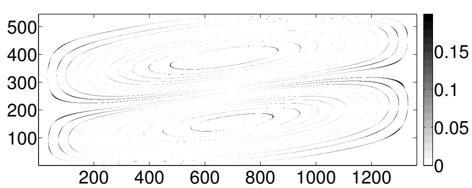

(g) Shear

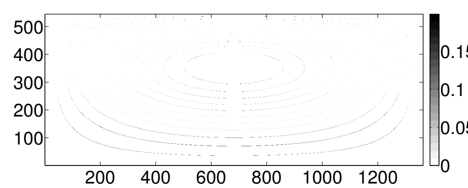

(h) L.V.

Fig. 3.4. Comparison of the intensity value of each pixel in corresponding grayscale images of the contour plots showing the difference between buckling mode shapes predicted by MSG and DNS for different boundary conditions and loadings. The horizontal and vertical axes are the x_1-x_2 coordinates of the pixels, respectively.

work to predict the nonlinear post-buckling behavior of stiffened composite plates. Same example studied in section 3.1.1 is used in this study.

The procedure to perform the post-buckling analysis for both DNS and MSG is the same and stated as follows. The first three buckling modes are selected to construct imperfections. The associated imperfection sizes (i.e., imperfection scaling factors) are assumed to be 2×10^{-4}, 1×10^{-4}, 0.5×10^{-4}. Results are predicted using 400 iteration steps with minimum arc length of 1×10^{-8} and maximum arc length of 0.1. It is noted that current work is only concerned with the elastic post-buckling behavior without considering material yielding.

Load-displacement curves are compared in Fig. 3.5. In the figure, vertical axis is the normalized uniaxial load with P_{cr} as the critical buckling load; horizontal axis is the axial shortening which is measured at the geometric center of the end cross section. It is seen that the load-displacement curve of MSG agrees very well with the curve of DNS. Modeling cost and computing time are compared in Table time. Regarding computational efficiency, current approach is more cost-efficient than DNS in modeling: 1575 shell elements (S8R5) in total as opposed to 411,804 solid elements (C3D20R) in total. MSG is also more time-efficient than DNS in performing post-buckling analysis: 18 minutes with one CPU as opposed to nearly 4 days with 32 CPUs. The computational time consumed in DNS could be reduced by using shell elements, but the accuracy of such solution would be greatly compromised [27]. In a nutshell, comparing with the DNS, MSG significantly reduces the computational efforts yet achieves high accuracy. For scholars who are interested in the details of the workstation on which the DNS is ran, they are given as follows: Dell Precision Tower 7910 powered by Intel Xeon CPU E5-2697 v3 with clock rate 2.60 GHz and 256 GB RAM.

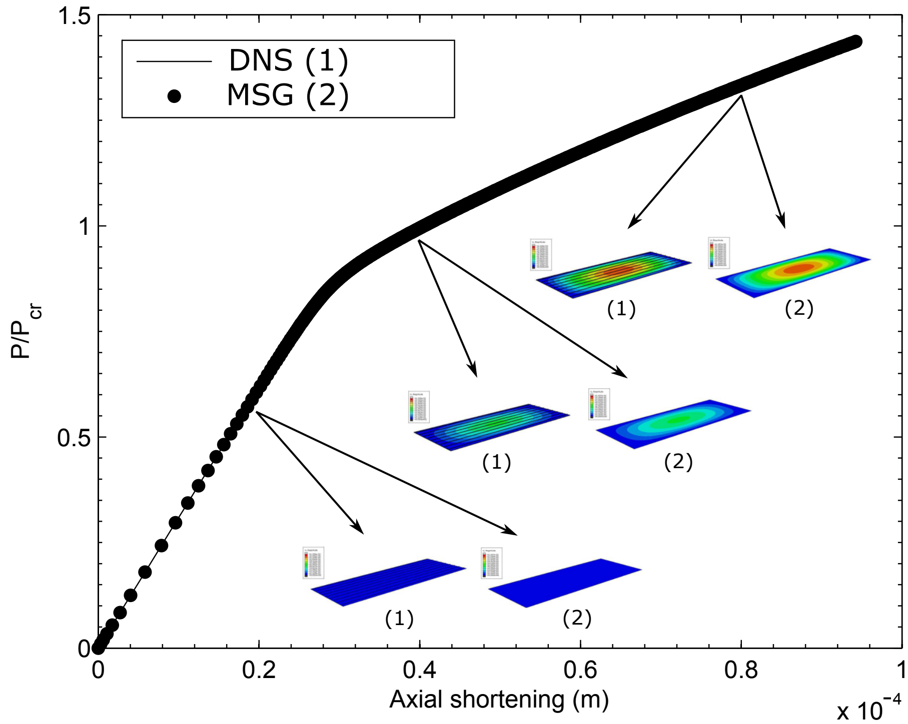

Fig. 3.5. Comparison of post-buckling load-displacement curve between current approach and DNS.

Table 3.4.
Comparison of computational cost to perform post-buckling analysis between current approach and DNS.

	MSG	DNS
Element type	Shell (S8R5)	Solid (C3D20R)
Total element number	1575	411,804
CPU number	1	32
Computational time	18 min	3 days 20 hrs

3.1.4 Buckling of orthogrid and isogrid stiffened composite plates

To validate MSG in the global buckling analysis of other stiffened composite plates, two examples of stiffened plates from Ref. [43] are studied. Their geometries, materials and stiffened patterns are reiterated as follows. Two flat plates with the length of 4.3764 m and the width of 1.5024 m are stiffened on one side by orthogrid and isogrid stiffeners, respectively, as shown in Fig. 2.1. Dimensions of a cell in the orthogrid are 0.10941 m long by 0.040095 m wide; dimensions of a cell in the isogrid are 0.236562 m long by 0.13658 m wide. The angles between stiffeners in the isogrid are 60 degrees. The skin laminate has an eight-ply symmetric layup of $[\pm 45/90/0]_s$ with each ply thickness equal to 0.1524 mm. The lamina properties are $E_1 = 139.31$ GPa, $E_2 = E_3 = 13.103$ GPa, $G_{12} = G_{13} = G_{23} = 5.0345$ GPa, $\nu_{12} = \nu_{13} = \nu_{23} = 0.3$. All the stiffeners are made of 0-degree material with a height of 12.9 mm and a width of 1.524 mm. The effective plate properties (A, B, and D matrices) of two examples are given in Tables 3.5 and 3.6.

Critical buckling loads and mode shapes predicted by MSG are compared with the results from Ref. [43] in Table 3.7. It is seen that the MSG results are very close to Ref. [43] and the DNS, which illustrates the high accuracy of MSG in predicting the global buckling loads of stiffened panels with various grid-patterns.

3.2 Local buckling of stiffened panels

3.2.1 Isotropic stiffened panels

A 1.4 m × 1.4 m stiffened panel made of Aluminum (E = 72GPa, ν = 0.33) is studied with stiffener patterns in Fig. 1.5 and stiffener profiles in Fig. 3.6 and geometric properties in Table 3.8. Skin thickness is kept at 1 mm. The stiffened panel ID 8 is loaded with shear force to induce shear buckling.

The first local buckling mode in 3D FEA is shown in Fig. 3.7. The buckling modes of first 5 stiffened panels (ID 1-5) are seen in skin local buckling. The buckling modes

Table 3.5.
The effective plate properties (A, B, and D matrices) of the orthogrid stiffened plate, units: SI.

$$\begin{bmatrix} 1.2021\times10^{8} & 2.4210\times10^{7} & 0 & 2.1300\times10^{5} & -2.0466\times10^{4} & 0 \\ & 9.6465\times10^{7} & 0 & -2.0511\times10^{4} & 6.5780\times10^{4} & 0 \\ & & 2.5376\times10^{7} & 0 & 0 & -2.2878\times10^{4} \\ & & & 2.4269\times10^{3} & 35.152 & 0 \\ & sym. & & & 1.1915\times10^{3} & 0 \\ & & & & & 26.548 \end{bmatrix}$$

Table 3.6.
The effective plate properties (A, B, and D matrices) of the isogrid stiffened plate, units: SI.

$$\begin{bmatrix} 9.8845\times10^{7} & 3.2062\times10^{7} & -1.0371\times10^{5} & -1.8535\times10^{5} & -5.8541\times10^{4} & -457.46 \\ & 1.0053\times10^{8} & -3.57691\times10^{4} & -5.8523\times10^{4} & -1.7879\times10^{5} & -166.00 \\ & & 3.3451\times10^{7} & -454.66 & -164.65 & -6.3335\times10^{4} \\ & & & 1.5959\times10^{3} & 523.23 & 0 \\ & sym. & & & 1.6431\times10^{3} & 0 \\ & & & & & 541.47 \end{bmatrix}$$

Table 3.7.
Comparison of critical buckling load and mode shape of the orthogrid and isogrid stiffened composite panels. Loads are in N/mm.

	MSG	Wang et al. [43]	DNS [43]
Orthogrid	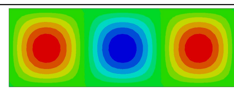 16.80 (-0.53%)	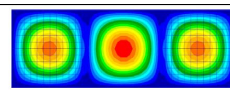 16.85 (-0.24%)	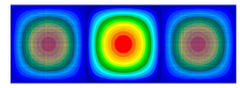 16.89
Anglegrid	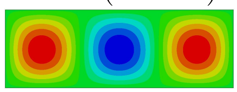 23.80 (0.85%)	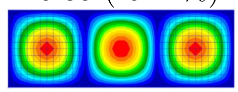 24.67 (4.53%)	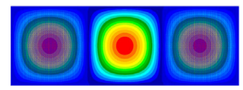 23.60

Table 3.8.
Stiffener profiles and geometric properties.

ID	stiffener shape	number of stiffeners	t_f (mm)	h_f (mm)
1	Blade	5	3	20
2	T-shape	5	3	20
3	Blade	10	3	20
4	Orthogrid	5×10	3	20
5	Orthogrid	10×10	3	20
6	Blade	5	1	70
7	Blade	5	1	140
8	Blade	5	3	40

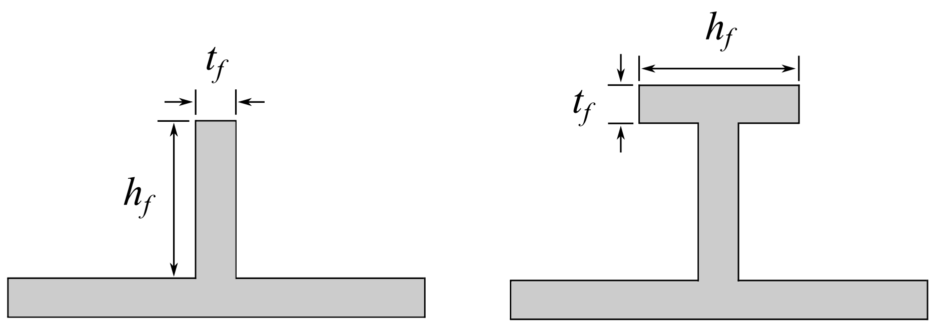

Fig. 3.6. Stiffener profiles. (a) Blade. (b) T-shape.

of the stiffened panel ID 6 and 7 are interactive buckling i.e. mix of skin buckling and stiffener buckling, and the buckling mode of the stiffened panel ID 8 is skin shear buckling due to the applied shear loads. In MSG method, failure maps are created showing the critical strains with different Bloch wave numbers (Figs. 3.8, 3.9, 3.10, 3.11, 3.12, 3.13, 3.14, and 3.15). Each shows the critical strains for the stiffened panel buckled in different buckling wavelengths. The minimum strain in each map indicates the critical strain of the first local buckling mode. The critical strain of the first local buckling mode by MSG is compared with DNS in Table 3.9. High percentage errors are found in ID 6 with 8.92% and in ID 8 with 11.45%. The first local buckling mode by MSG method is shown in Figs. 3.16, 3.17, 3.18, 3.19, 3.20, 3.21, 3.22 and 3.23. Each deformed SG is given as well as the expanded SG in 2 by 2. The expanded SG is made according to the Eq. (2.62). For example, for a expanded SG in 2 by 2, the fluctuating function of a node in the second SG in x_1 direction dV_2 is related to the fluctuating function of same node in the first SG dV_1 through $dV_2 = dV_1 \cdot e^{i2\pi n_1}$ with n_1 the Bloch wave number for this buckling. For convenience, the entire stiffened panel is not reproduced from the deformed SG. Buckling wavelength is also compared. The major concern is the wavelength in longitudinal direction in which load applies. Validation of the wavelength is given in Table 3.10. Wavelengths in MSG solutions are computed as follows: SG size is divided by the Bloch wave number n_1. Wavelengths in DNS are computed as follows: panel length is divided by the number of waves. It is seen that MSG solutions are in good agreement with DNS results except ID 7. It is found that the SG size has to be at least half of buckling wavelength ($n \geq 0.5$). This observation coincides with Ref. [93] that n and $1 - n$ identify the same mode. Increasing SG size of ID 7 to 350 mm (half of the wavelength in DNS) or more will result in good agreement with DNS solution. It should be noted that higher modes are not studied in this local buckling analysis.

Table 3.9.
Critical compressive strain of the first local buckling mode ($\times 10^{-5}$).
For ID 8, it is the critical shear strain $2\epsilon_{12}$.

ID	buckling mode	MSG (error)	DNS
1	skin buckling	7.60 (0.66%)	7.55
2	skin buckling	8.10 (-2.17%)	8.28
3	skin buckling	31.9 (0.63%)	31.7
4	skin buckling	36.1 (3.44%)	34.9
5	skin buckling	43.6 (2.59%)	42.5
6	skin&stiffener buckling	5.00 (-8.92%)	5.49
7	skin&stiffener buckling	3.80 (-5.00%)	4.00
8	skin shear buckling	29.2 (11.45%)	26.2

Table 3.10.
Validation of buckling mode shapes by comparing buckling wavelengths.

ID	MSG			DNS	
	SG size (mm)	n_x	Wavelength (mm)	No. of half waves	Wavelength (mm)
1	280	0.62	451.6	6	466.7
2	280	0.7	400	7	400
3	140	0.7	200	13	215.3
4	280	1	280	10	280
5	140	0.5	280	9	311.1
6	280	0.5	560	5	560
7	280	0.5	560	4	700
8	280	0.5	560	5	560

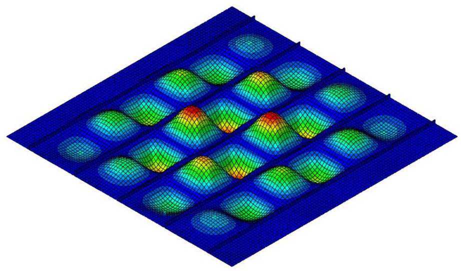

(a) Stiffened panel ID 1

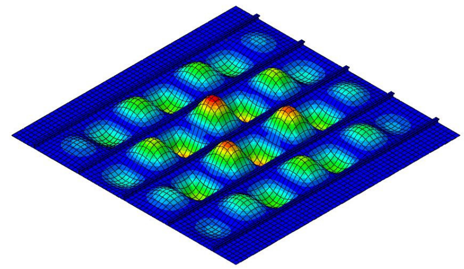

(b) Stiffened panel ID 2

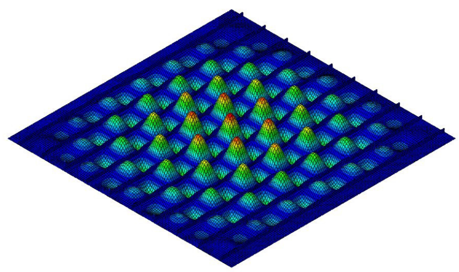

(c) Stiffened panel ID 3

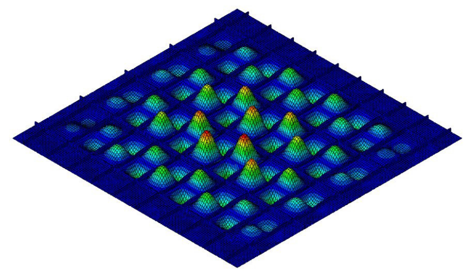

(d) Stiffened panel ID 4

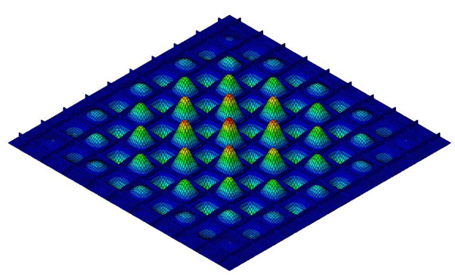

(e) Stiffened panel ID 5

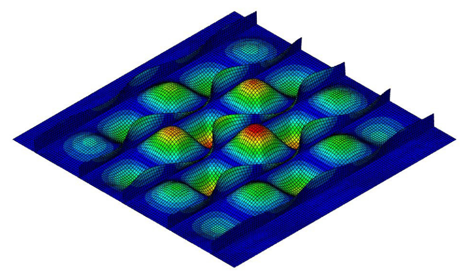

(f) Stiffened panel ID 6

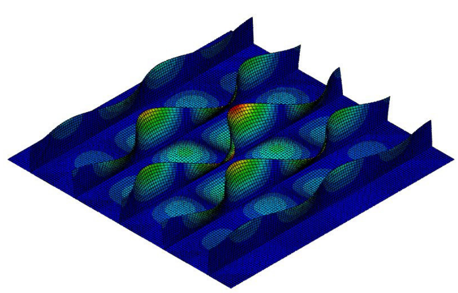

(g) Stiffened panel ID 7

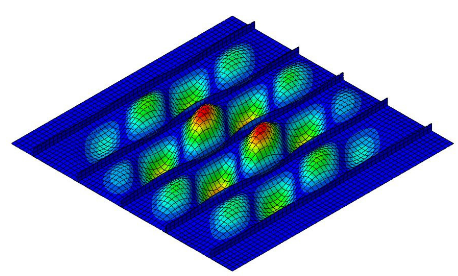

(h) Stiffened panel ID 8

Fig. 3.7. The first local buckling mode in DNS solutions.

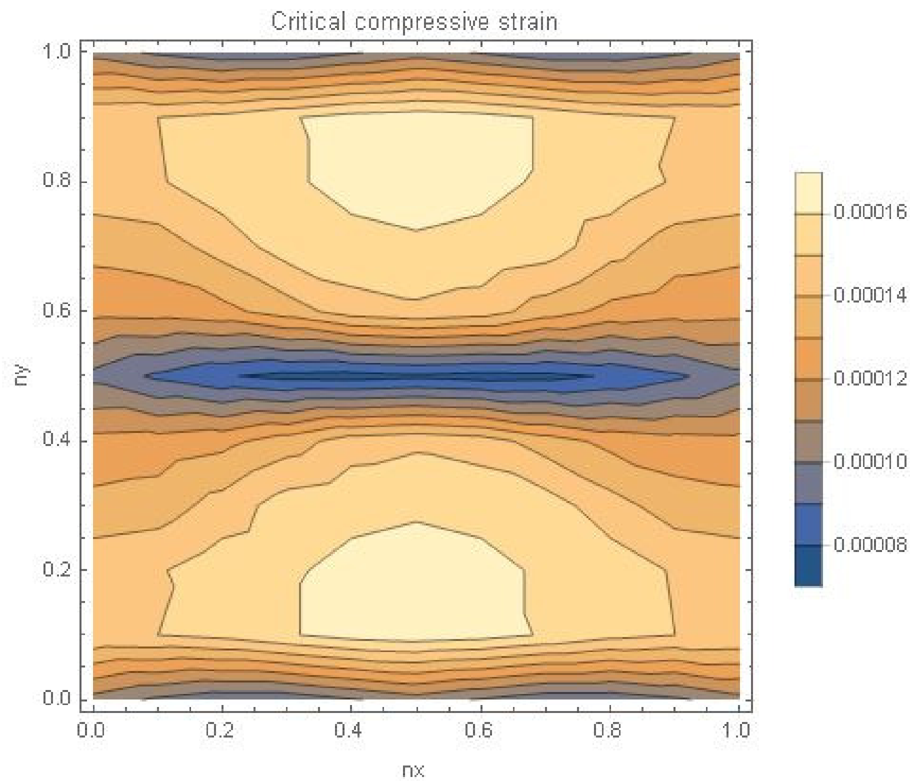

Fig. 3.8. Buckling failure map of stiffened panel ID 1: critical compressive strains in different Bloch wave numbers by MSG method.

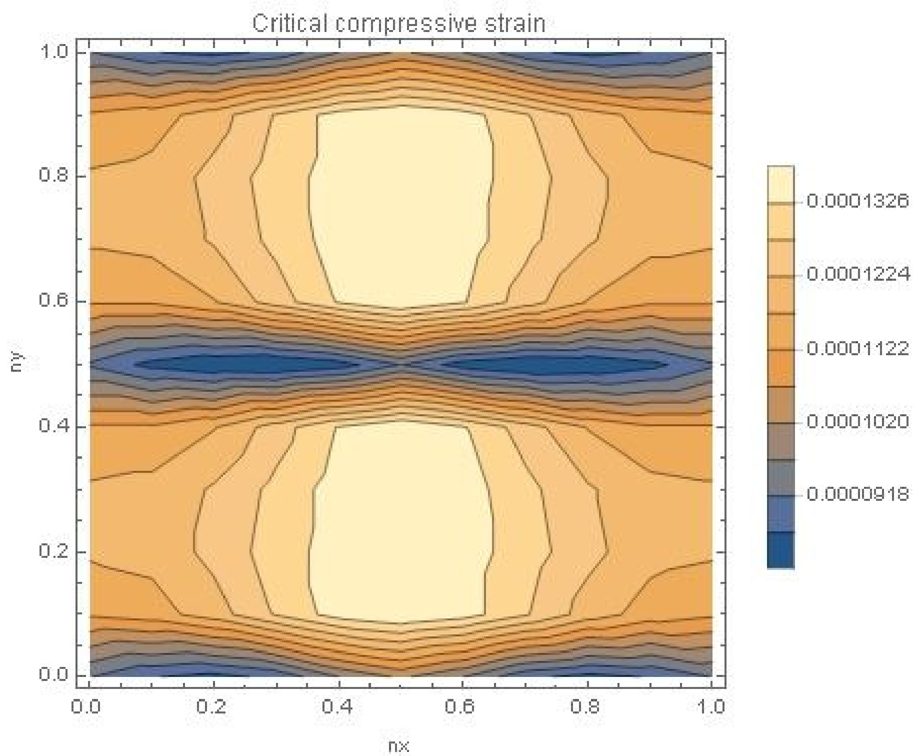

Fig. 3.9. Buckling failure map of stiffened panel ID 2: critical compressive strains in different Bloch wave numbers by MSG method.

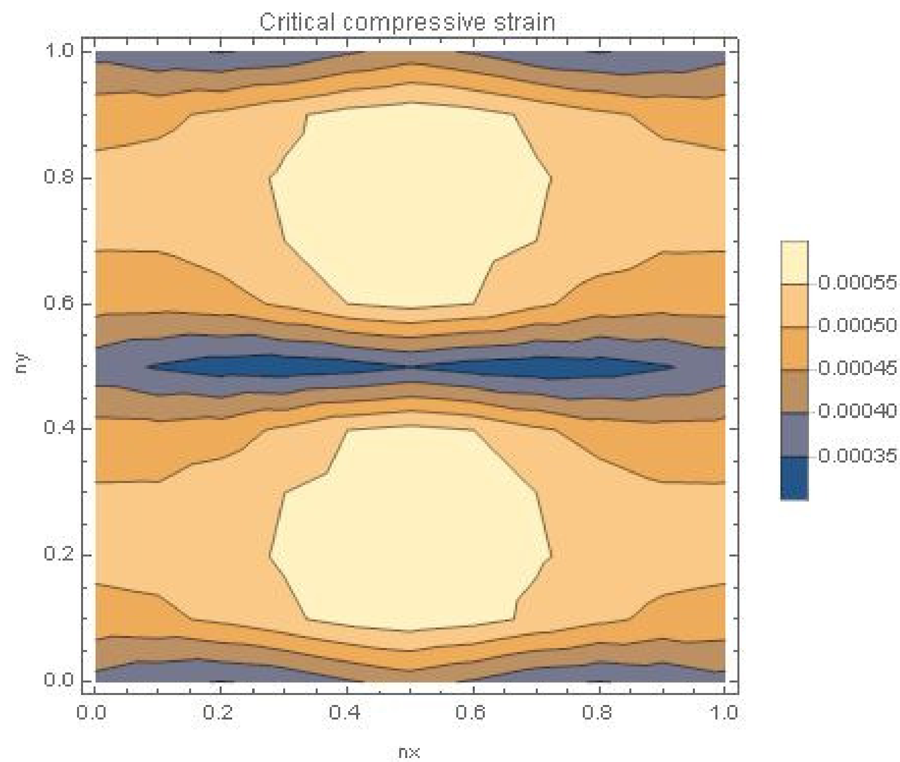

Fig. 3.10. Buckling failure map of stiffened panel ID 3: critical compressive strains in different Bloch wave numbers by MSG method.

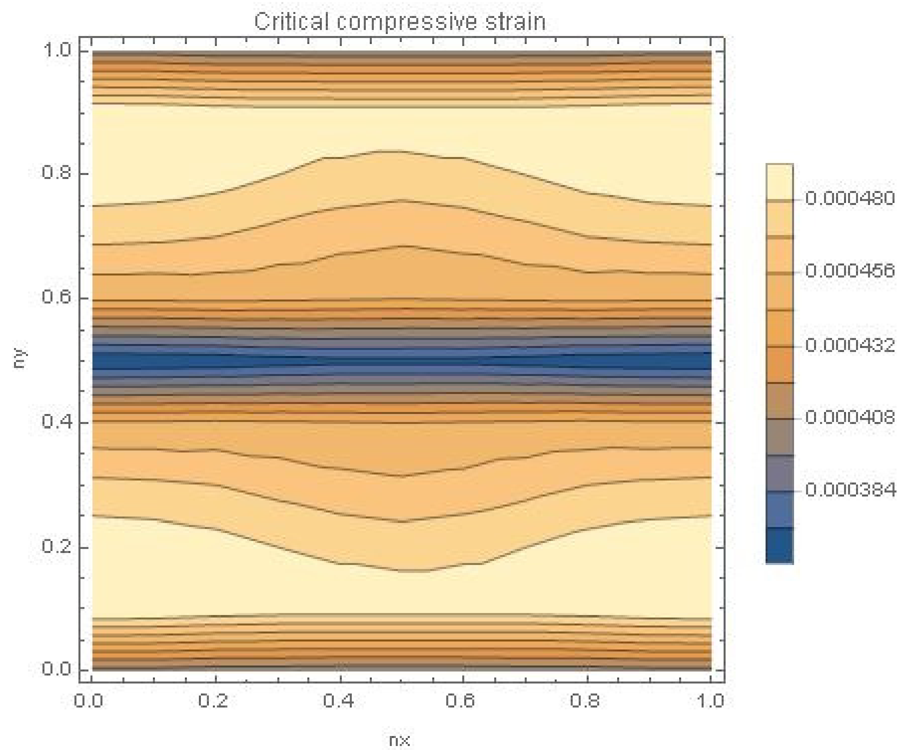

Fig. 3.11. Buckling failure map of stiffened panel ID 4: critical compressive strains in different Bloch wave numbers by MSG method.

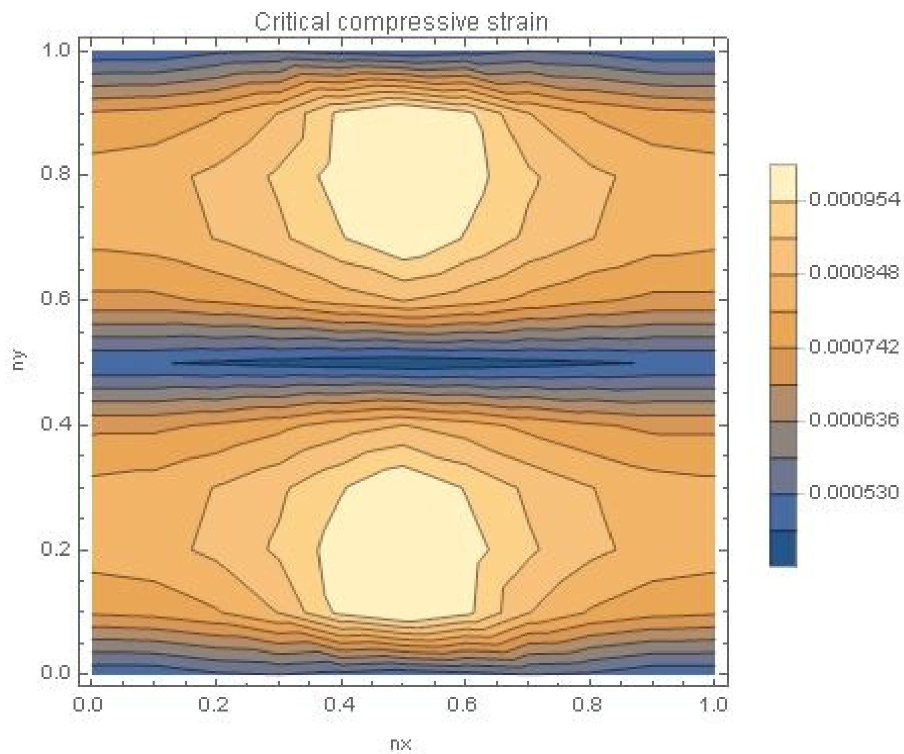

Fig. 3.12. Buckling failure map of stiffened panel ID 5: critical compressive strains in different Bloch wave numbers by MSG method.

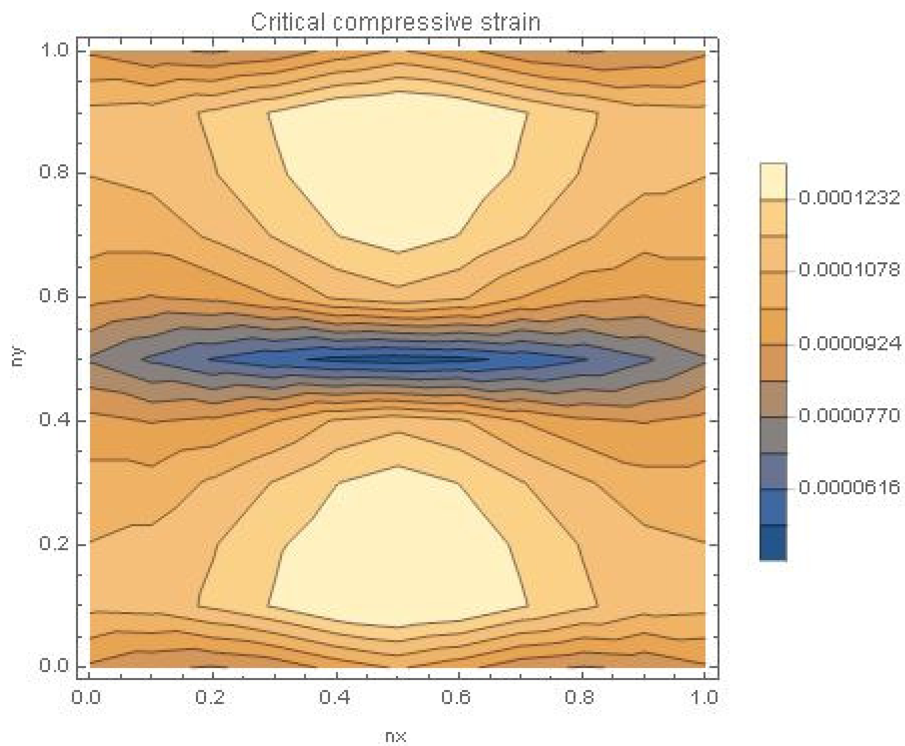

Fig. 3.13. Buckling failure map of stiffened panel ID 6: critical compressive strains in different Bloch wave numbers by MSG method.

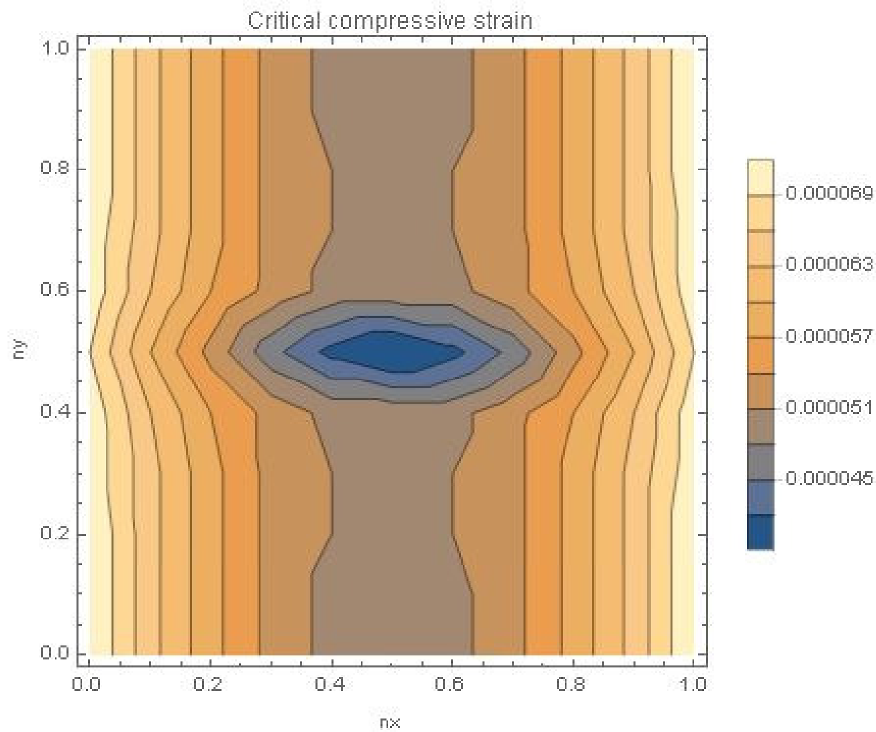

Fig. 3.14. Buckling failure map of stiffened panel ID 7: critical compressive strains in different Bloch wave numbers by MSG method.

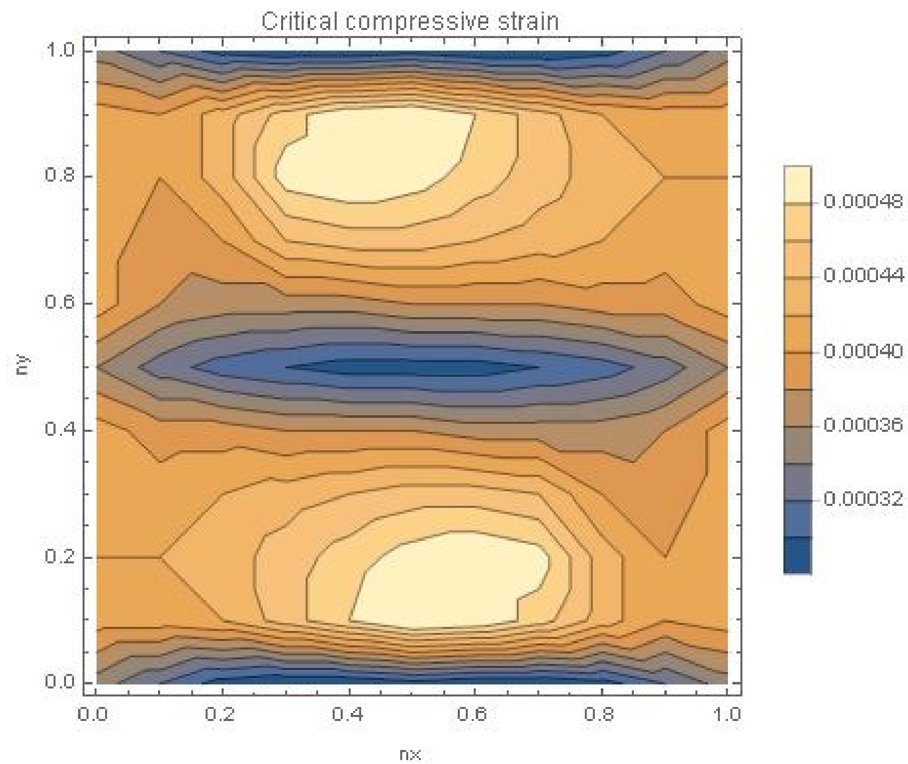

Fig. 3.15. Buckling failure map of stiffened panel ID 8: critical compressive strains in different Bloch wave numbers by MSG method.

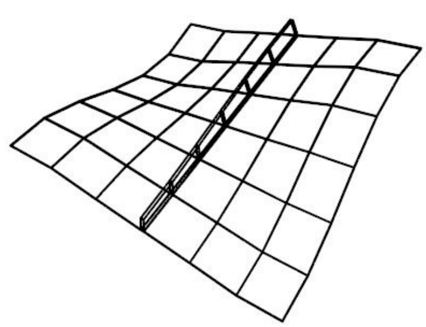

(a) SG

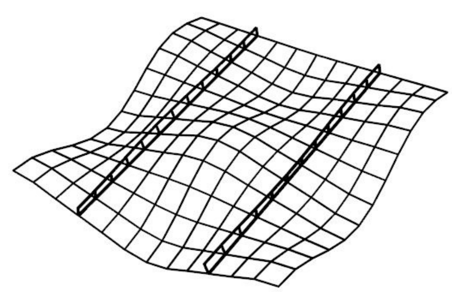

(b) Expanded 2 by 2 SG

Fig. 3.16. Buckling mode shape of stiffened panel ID 1.

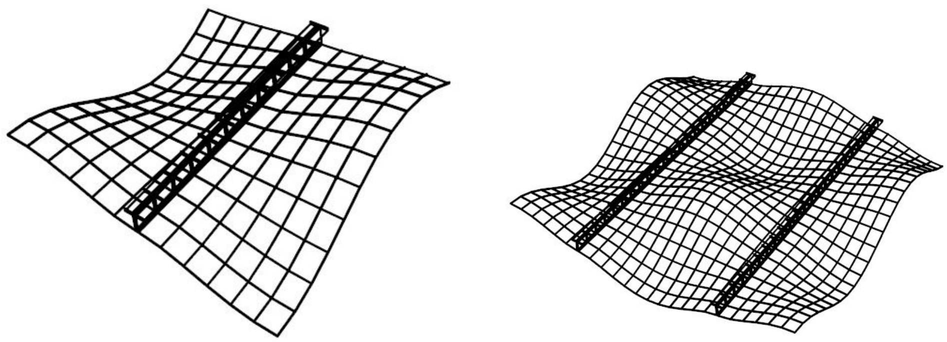

(a) SG (b) Expanded 2 by 2 SG

Fig. 3.17. Buckling mode shape of stiffened panel ID 2.

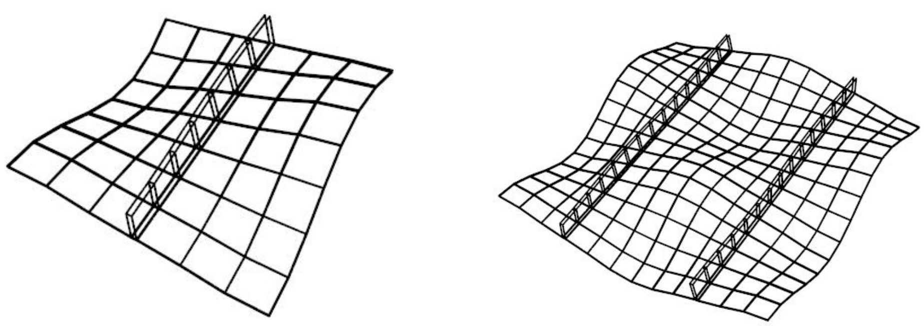

(a) SG (b) Expanded 2 by 2 SG

Fig. 3.18. Buckling mode shape of stiffened panel ID 3.

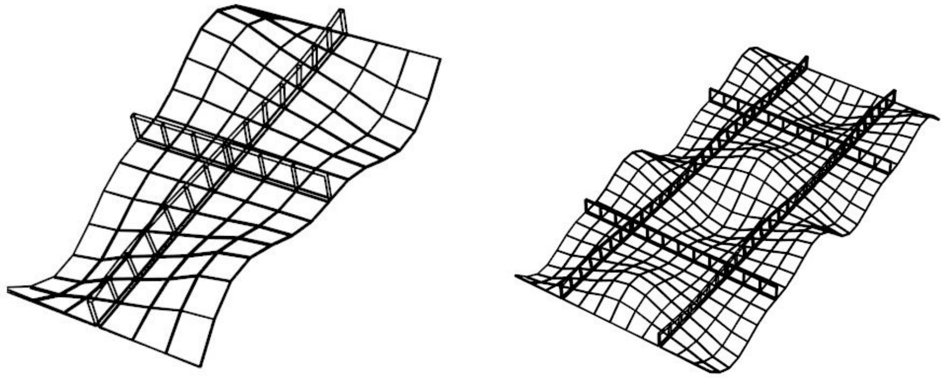

(a) SG (b) Expanded 2 by 2 SG

Fig. 3.19. Buckling mode shape of stiffened panel ID 4.

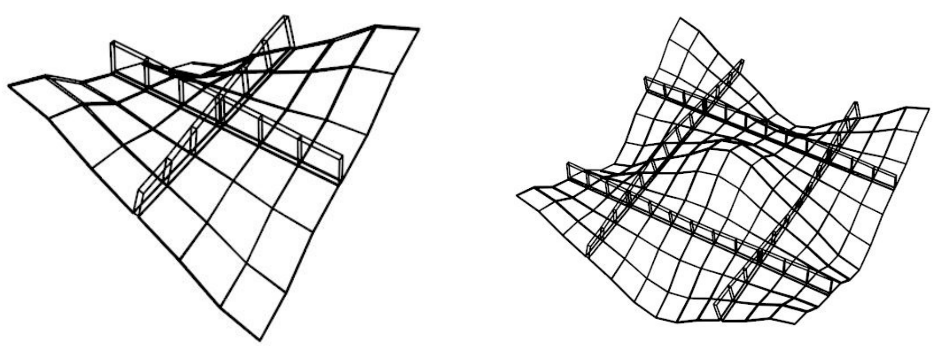

(a) SG (b) Expanded 2 by 2 SG

Fig. 3.20. Buckling mode shape of stiffened panel ID 5.

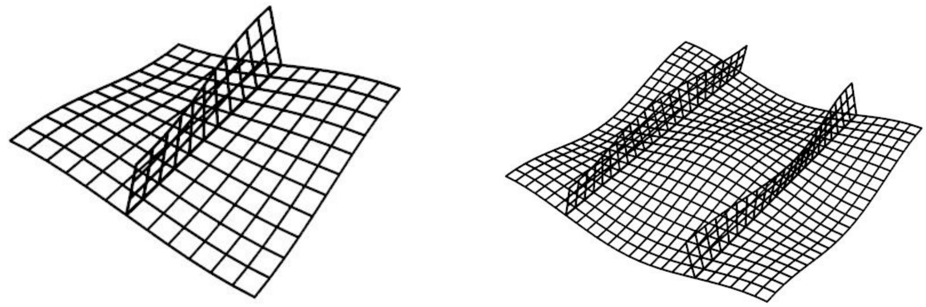

(a) SG (b) Expanded 2 by 2 SG

Fig. 3.21. Buckling mode shape of stiffened panel ID 6.

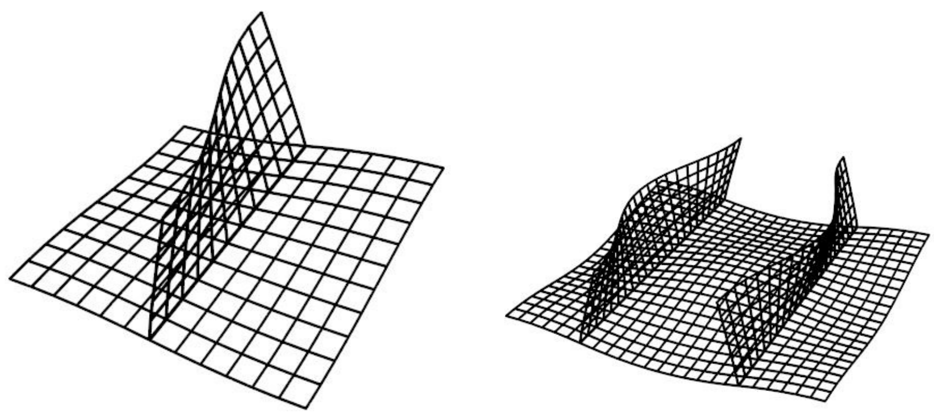

(a) SG (b) Expanded 2 by 2 SG

Fig. 3.22. Buckling mode shape of stiffened panel ID 7.

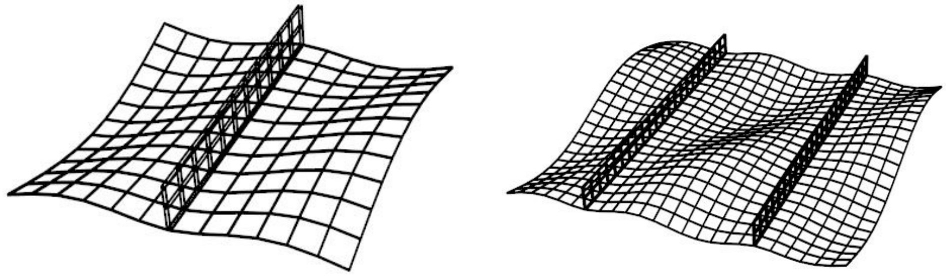

(a) SG (b) Expanded 2 by 2 SG

Fig. 3.23. Buckling mode shape of stiffened panel ID 8.

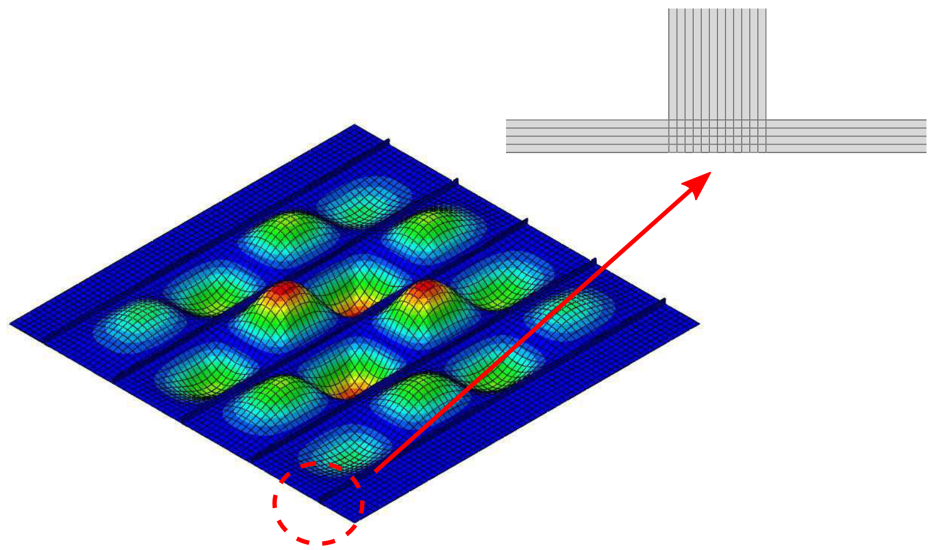

Fig. 3.24. Buckling mode shape of composite stiffened panel in DNS solution.

3.2.2 Laminated stiffened panels

A 1.4 m $\times$ 1.4 m stiffened panel made of laminates is studied to demonstrate the capability of MSG method in local buckling analysis of composite stiffened panels. The stiffener profiles and geometric properties are those of ID 1 given in Table 3.8. The skin lamination layup is $[0/90]_s$. The stiffener lamination layup is $[(45/-45)_2 0_2]_s$. Lamina material constants are $E_1 = 113$ GPa, $E_2 = E_3 = 9$ GPa, $G_{12} = G_{13} = 3.82$ GPa, $G_{23} = 3.46$ GPa, $\nu_{12} = \nu_{13} = \nu_{23} = 0.302$. The buckling mode shape in 3D FEA is shown in Fig. 3.24. It is noticed that the wavelength is different from that in the isotropic stiffened panel meaning that different materials can result in different wavelength. The critical nominal strain in DNS is 3.97×10^{-5}. The buckling failure map obtained using MSG method is shown in Fig. 3.25 From the failure map, the minimum critical strain is obtained at $n_x = n_y = 0.5$, i.e., $\epsilon_{cr} = 3.8 \times 10^{-5}$ which agrees with the DNS solution well. The deformed SG and the expanded 2 by 2 SG are shown in Fig. 3.26 which shows good agreement with the DNS solution.

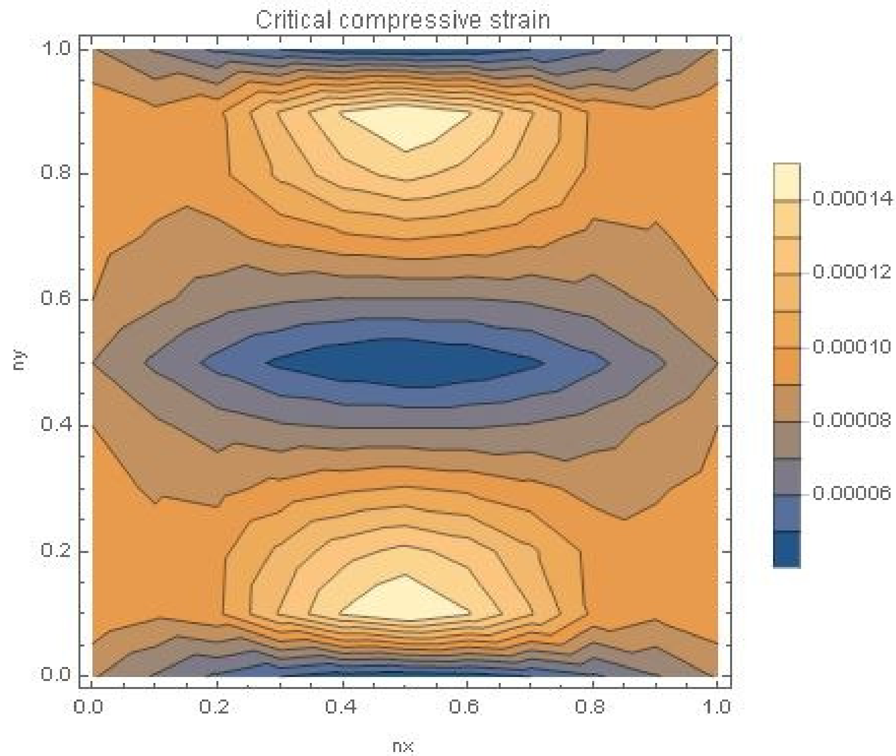

Fig. 3.25. Buckling failure map of composite stiffened panel in MSG solution.

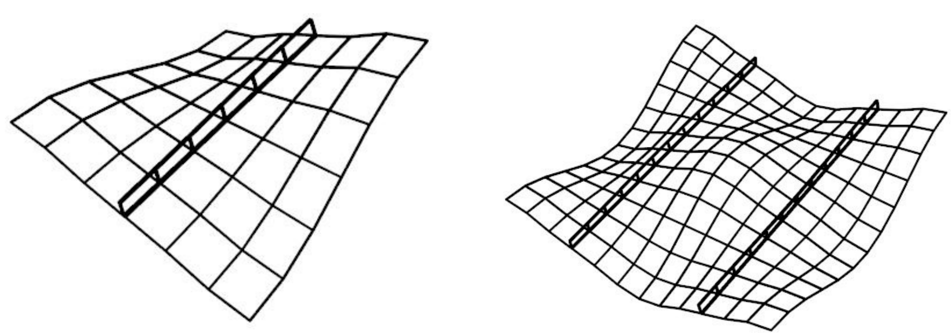

(a) SG (b) Expanded 2 by 2 SG

Fig. 3.26. Buckling mode shape of composite stiffened panel in MSG solution.

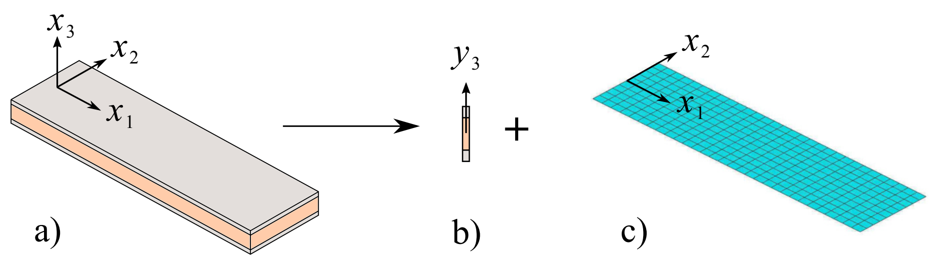

Fig. 3.27. Global buckling analysis of sandwich structures approximated by the buckling of macroscopic plate whose effective plate properties are computed by constitutive modeling using MSG. a) The original sandwich structure. b) SG. c) Macroscopic plate model.

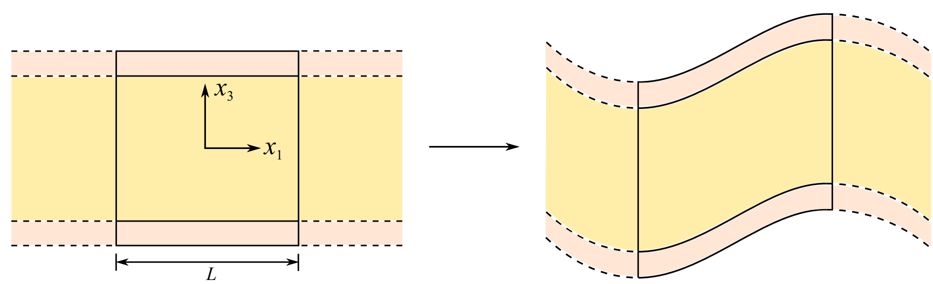

Fig. 3.28. A SG in a sandwich structure deforms along with the onsets of buckling.

3.3 Global and local buckling of sandwich structures

Buckling analysis of sandwich structures is similar to buckling analysis of stiffened panels. The global buckling of sandwich structures is approximated by the buckling of the macroscopic plates (Fig. 3.27). Geometric linear constitutive modeling is used to compute the effective plate properties. On the other hand, the local buckling of sandwich structures is predicted on a SG under Bloch-periodic boundary conditions (Fig. 3.28).

Current method is validated using three case studies by comparing current solutions with DNS in Abaqus. 3D geometries of the sandwich structures described in Leotoing et al. [63] are created. Geometric parameters and material properties are given in Table 3.11. The material and geometry parameters are kept throughout the studies unless specific change is mentioned. Critical displacements are compared

Table 3.11.
Material and geometry parameters [63].

E_s(MPa)	E_c(MPa)	ν_s=ν_c	L(mm)	W(mm)	h_s(mm)	h_c(mm)
50,000	70	0.4	600	40	1	10/30/60

along with their associated mode shapes. Parametric studies are performed using MSG method to investigate the influence of width and core thickness on the selective buckling modes. MSG method is also validated in buckling of sandwich structures under bending. Moreover, MSG is compared with RVE analysis with Bloch-periodic boundary conditions using commercial finite element packages such as Abaqus for efficiency and accuracy.

3.3.1 Validation example (h_c=30 mm)

A sandwich column with h_c=30 mm is considered first as a validation case study. The current solution is compared with DNS and Le Grognec [17]. The first 10 buckling modes are compared and given in Table 3.12. MSG successfully predicts the type II flexural mode while Le Grognec [17] is unable to predict this. MSG solution is also more close to the DNS solution than Le Grognec [17]. Maximum error is found to be 2.45% in current solution and 6.39% in Le Grognec [17]. Selective mode shapes are compared in Table 3.13. They are seen in complete agreement.

Figure 3.29 plots the type I flexure modes, antisymmetric wrinkling modes and symmetric wrinkling modes together versus half-wave number. It is observed that MSG solutions are in good agreement with DNS for a wide range of wavelength with maximum 2.84% error in antisymmetric modes at half wave number equal to 33 and 4.81% error in symmetric modes at half wave number equal to 25. In contrast, Le Grognec [17] differs from the DNS solutions with maximum 9.37% error in antisym-

Table 3.12.
Critical displacements of the first 10 modes (h_c=30 mm).

Mode	Type	DNS	MSG		Le Grognec [17]	
		$\lambda_{cr}(mm)$	$\lambda_{cr}(mm)$	Error	$\lambda_{cr}(mm)$	Error
1	Flexure I	2.142	2.131	-0.51%	2.178	1.70%
2	Flexure II	2.175	2.170	-0.23%	/	/
3	Flexure I	3.648	3.613	-0.96%	3.693	1.22%
4	Flexure I	4.191	4.147	-1.05%	4.232	0.97%
5	Flexure I	4.418	4.374	-1.00%	4.452	0.77%
6	Antisym. wk.	4.444	4.547	2.33%	4.154	-6.52%
7	Antisym. wk.	4.445	4.548	2.32%	4.155	-6.52%
8	Antisym. wk.	4.446	4.550	2.35%	4.159	-6.47%
9	Antisym. wk.	4.450	4.553	2.31%	4.160	-6.51%
10	Antisym. wk.	4.452	4.561	2.45%	4.167	-6.39%

Table 3.13.
Comparison of selective mode shapes (h_c=30 mm).

Mode	DNS	MSG
1	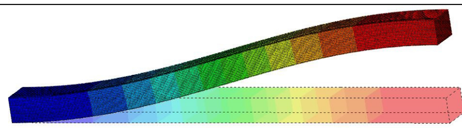	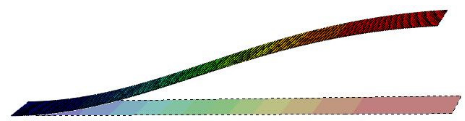
2	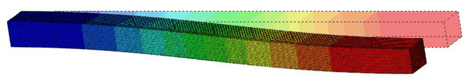	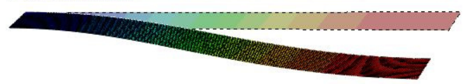
3	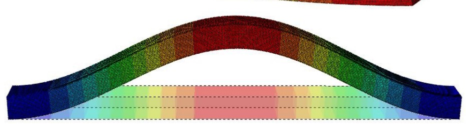	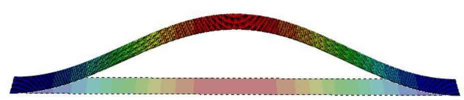
6	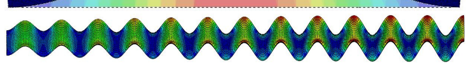	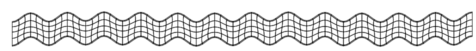
7	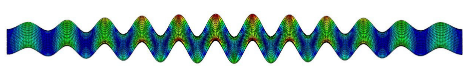	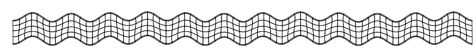
Sym. wk.	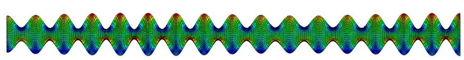	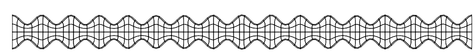

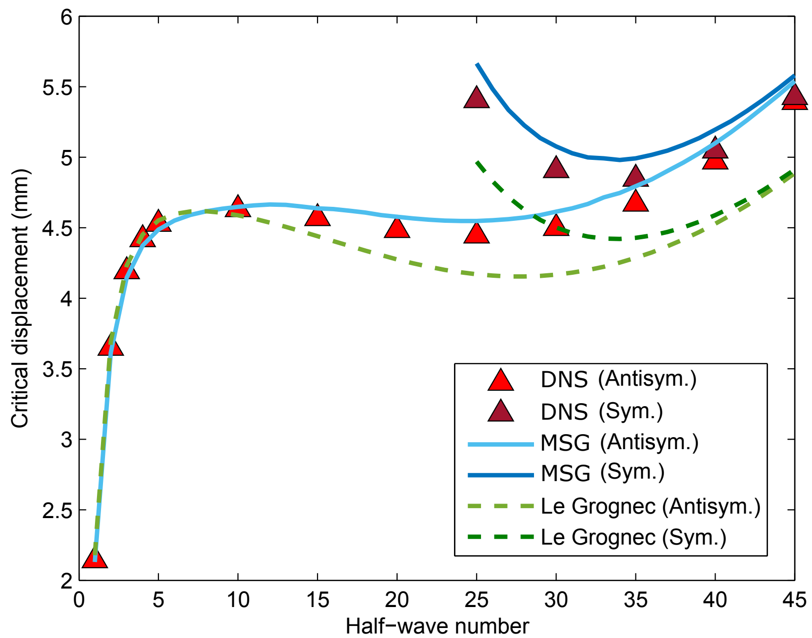

Fig. 3.29. Comparison of antisymmetric wrinkling and symmetric wrinkling modes between DNS, MSG and Le Grognec [17] (h_c=30 mm).

metric modes and 9.45% error in symmetric modes both at half wave number equal to 45.

The effect of transverse shear stiffness on the buckling behavior of sandwich structures is also investigated (Fig. 3.30). Prediction using the shear stiffness from Appendix A agrees with the DNS results better than the prediction using shear stiffness from a simplified distribution [121]. Detailed derivation of the shear stiffness is given in Appendix A.

3.3.2 Validation example (h_c=60 mm)

A sandwich column with h_c=60 mm is considered as the second validation case study. The first 10 buckling modes are compared and presented in Table 3.14. Type II flexural mode becomes the dominate mode in this case with same critical displacement

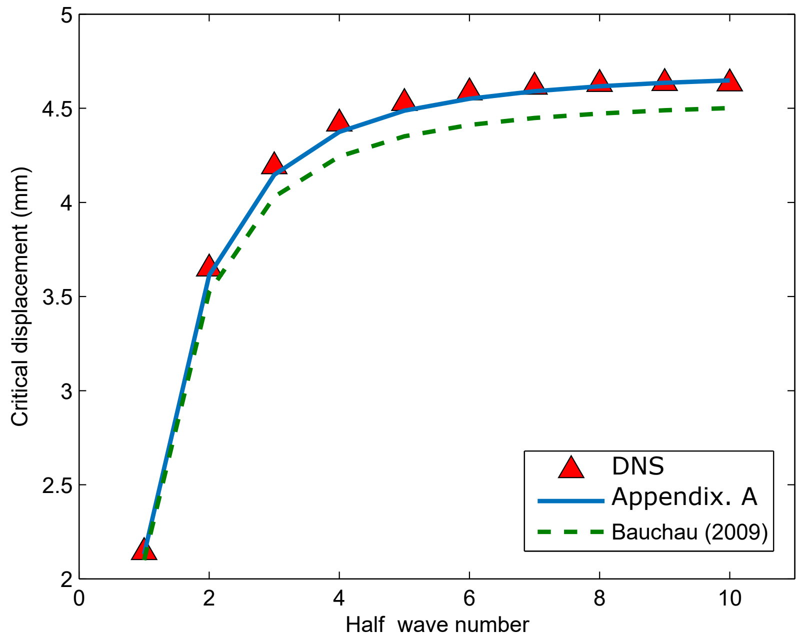

Fig. 3.30. Effect of the transverse shear stiffness on the critical values of the type I flexural buckling (h_c=30 mm).

Table 3.14.
Critical displacements of the first 10 modes (h_c=60 mm).

Mode	Type	DNS	MSG		Le Grognec [17]	
		$\lambda_{cr}(mm)$	$\lambda_{cr}(mm)$	Error	$\lambda_{cr}(mm)$	Error
1	Flexure II	2.176	2.170	-0.28%	/	/
2	Antisym. wk.	4.684	4.823	2.98%	4.313	-7.92%
3	Antisym. wk.	4.687	4.824	2.92%	4.314	-7.95%
4	Sym. wk.	4.688	4.823	2.89%	4.316	-7.94%
5	Antisym. wk.	4.690	4.830	2.99%	4.320	-7.90%
6	Sym. wk.	4.693	4.824	2.79%	4.318	-7.99%
7	Sym. wk.	4.694	4.830	2.90%	4.321	-7.94%
8	Antisym. wk.	4.700	4.836	2.89%	4.324	-8.00%
9	Antisym. wk.	4.704	4.836	2.81%	4.334	-7.87%
10	Sym. wk.	4.706	4.836	2.76%	4.329	-8.01%

as it is in the case of h_c=30 mm. This indicates that the critical displacement of type II flexural mode does not depend on the core thickness. Again, highly accurate results are seen in MSG solution in comparison with the DNS solution with maximum 2.99% error. Good agreement is observed in the comparison of the mode shapes (Fig. 3.15). Le Grognec [17] fails to predict the type II flexural mode again and the maximum error of critical displacement is 8.01%.

In the comparison of antisymmetric modes and symmetric modes versus half-wave number (Fig. 3.31), it is observed that for half-wave number greater than 25 the antisymmetric modes and symmetric modes coincide with each other. This indicates that the skins are buckled in an uncoupled manner.

Table 3.15.
Comparison of selective mode shapes (h_c=60 mm).

Mode	DNS	MSG
1	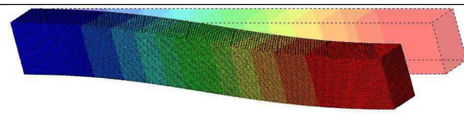	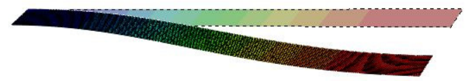
2	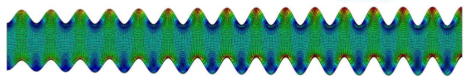	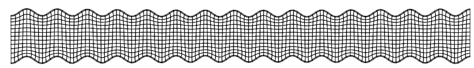
4	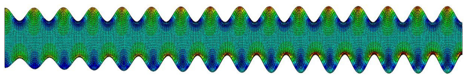	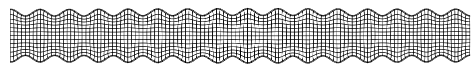

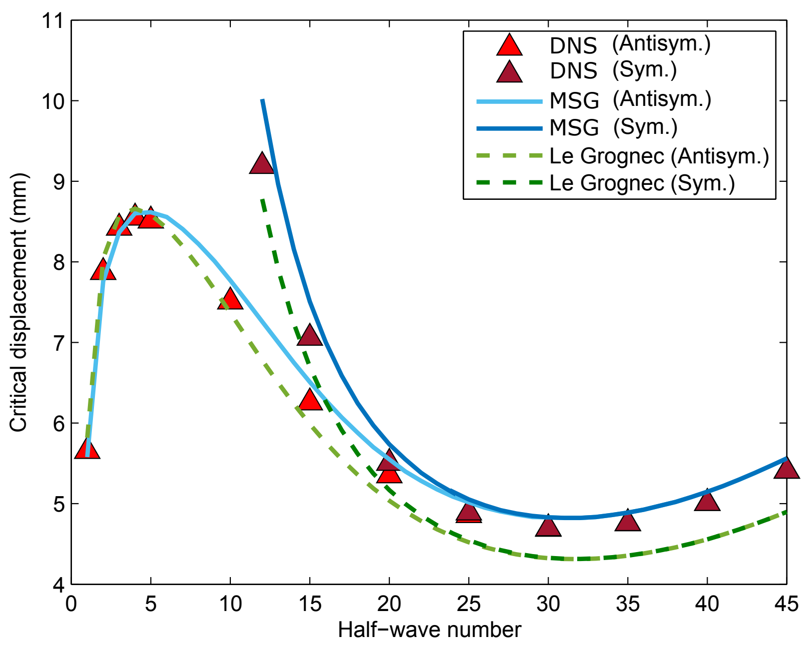

Fig. 3.31. Comparison of antisymmetric wrinkling and symmetric wrinkling modes between DNS, MSG and Le Grognec [17] (h_c=60 mm).

Table 3.16.
Critical displacements of the first 10 modes (h_c=10 mm).

Mode	Type	DNS	MSG		Le Grognec [17]	
		$\lambda_{cr}(mm)$	$\lambda_{cr}(mm)$	Error	$\lambda_{cr}(mm)$	Error
1	Flexure I	0.411	0.409	-0.58%	0.393	-4.59%
2	Torsion	0.918	0.915	-0.31%	/	/
3	Flexure I	0.992	0.985	-0.73%	0.956	-3.69%
4	Torsion	1.264	1.255	-0.71%	/	/
5	Flexure I	1.339	1.323	-1.19%	1.304	-2.60%
6	Torsion	1.491	1.473	-1.27%	/	/
7	Flexure I	1.529	1.501	-1.83%	1.499	-1.95%
8	Torsion	1.624	1.593	-1.91%	/	/
9	Flexure I	1.642	1.600	-2.62%	1.616	-1.58%
10	Torsion	1.706	1.661	-2.64%	/	/

3.3.3 Validation example (h_c=10 mm)

A sandwich plate with h_c=10mm, W=600mm is studied to investigate the torsional mode. MSG solution is compared with Le Grognec [17] and DNS solution for the critical displacements of the first 10 modes in Table 3.16. It is seen that MSG method is able to predict the torsional modes and corresponding mode shapes (Fig. 3.17) whereas Le Grognec [17] is not able to do so.

3.3.4 Effect of width and core thickness on flexural modes

The objective of this parametric study is to use MSG approach to determine the relative influence of the width and core thickness on the critical displacements of the first type I flexural mode and first type II flexural mode. It is noticed in

Table 3.17.
Comparison of selective mode shapes (h_c=10 mm).

Mode	DNS	MSG
1	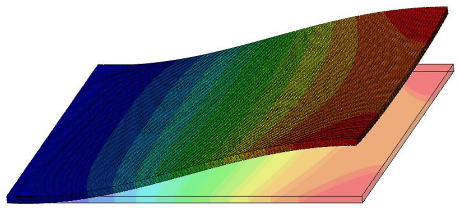	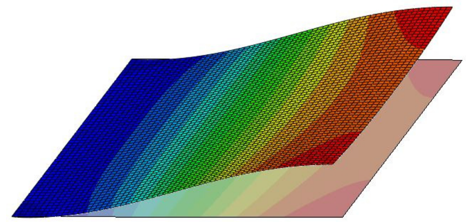
2	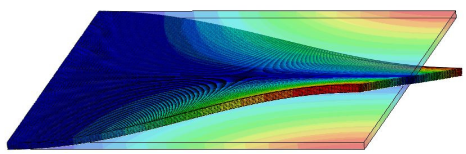	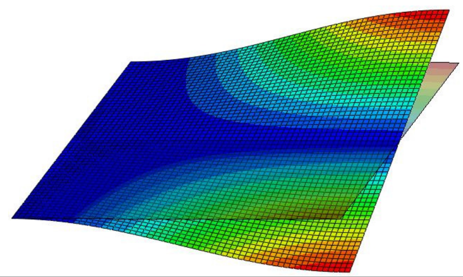

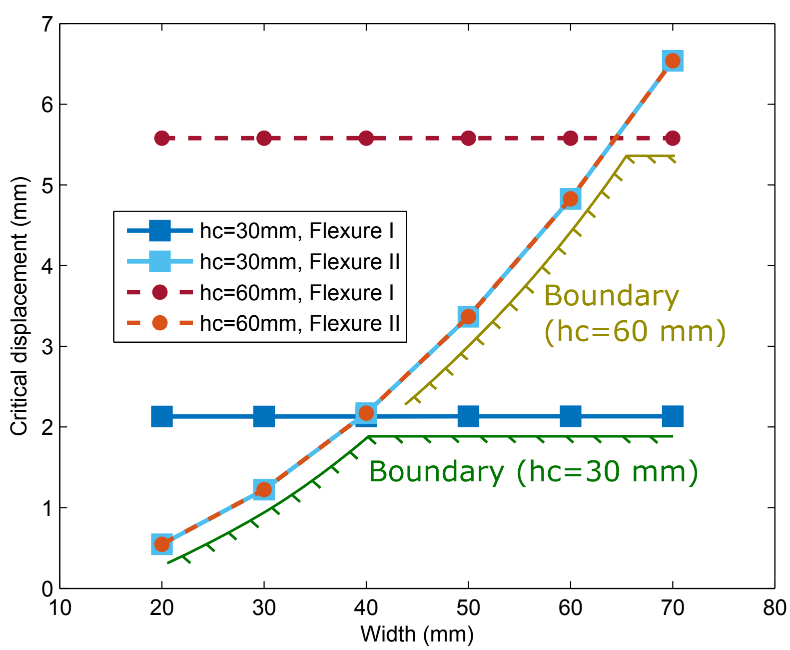

Fig. 3.32. Effect of width and core thickness on the critical displacements of the first type I flexural mode and first type II flexural mode.

the aforementioned validation that increasing the core thickness does not affect the critical displacement of the type II flexural mode, but affects the critical displacement of the type I flexural mode. The relation of the critical displacements of these two modes to width is investigated (Fig. 3.32). It is found that the critical displacement of the first type I flexural mode is only related to core thickness while the critical displacement of the first type II flexural mode is only related to width. For h_c=30 mm, the buckling boundary is hold by the type II flexure mode before width being 40 mm and by type I flexure mode afterwards. For h_c=60 mm, it is hold by the type II flexure mode before width being 64 mm and by type I flexure mode afterwards. This observation indicates that for a given core thickness column-like sandwich structures (thin and tall) buckle in type II flexure mode first while plate-like sandwich structures (wide and short) buckle in type I flexure mode first. Increasing the core thickness postpones the transition from type II flexural mode to type I flexural mode. It should be noted that the interference of local (wrinkling) modes on the buckling boundary is not studied here.

3.3.5 Effect of width and core thickness on torsional modes

Relative influence of the width and core thickness on the critical displacements of the first type I flexural mode and first torsional mode is investigated. Length is kept at L=600 mm. Width is presented in a normalized fashion b/L. It is observed in Fig. 3.33 that core thickness affects both the type I flexural mode and the torsional mode. The thicker the core thickness becomes, the harder the sandwich plates are to buckle. On the other hand, width has a strong influence on the critical displacement of the torsional mode as opposed to the type I flexural mode. The curve of torsional mode declines a lot as width increases yet remains above the curve of the type I flexural mode in the studied range of width. Critical displacement of the first torsional mode is normalized by comparing it with the first type I flexural mode in each case separately (Fig. 3.34). Curves are found to be highly correlated. It means that changing core

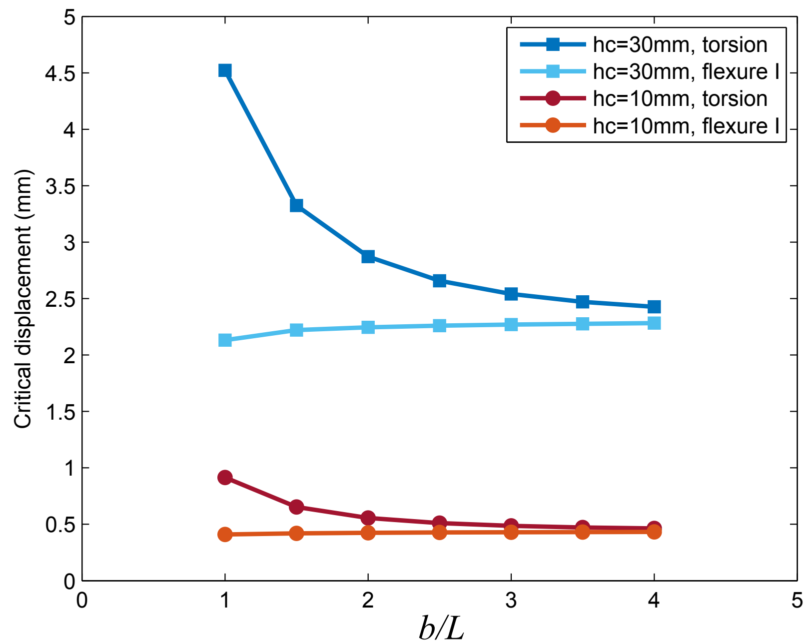

Fig. 3.33. Effect of width and core thickness on the critical displacement of the first type I flexural mode and first torsional mode.

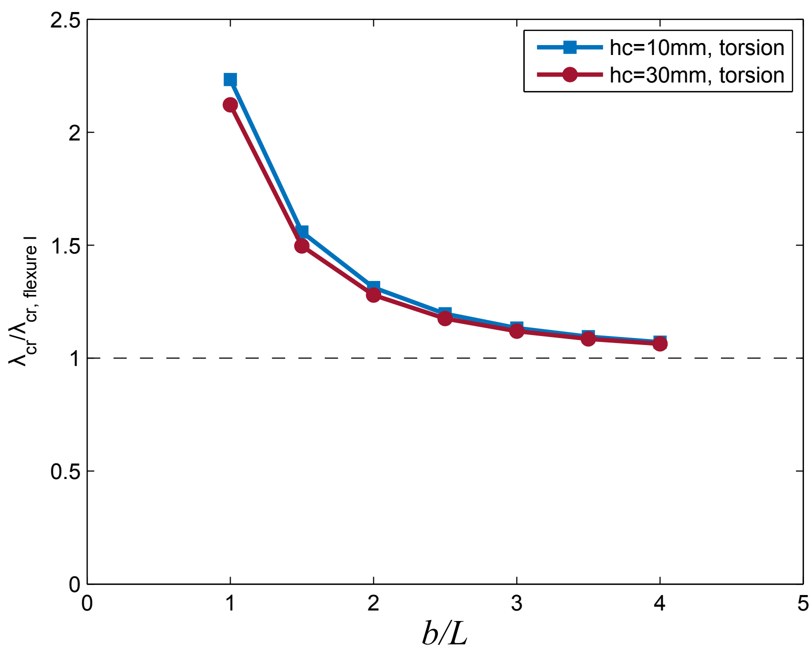

Fig. 3.34. Effect of width on the normalized critical displacement of the first torsional mode.

thickness has very little effect on the relative ratio of the critical displacements of the two modes. The determining factor comes from the relative width. For sandwich plates with moderate width $b/L \leq 3$, the torsional modes of buckling can be ignored in the design and optimization of sandwich structures. However for very wide sandwich plates $b/L > 3$, the first torsional mode must be taken into consideration as its critical value is very close to that of the first type I flexural mode (difference less than 10%).

3.3.6 Post-local-buckling

Post-local-buckling describes the mechanical behavior of structures after onsets of local buckling as loads continue. Load-carrying capability could be degraded in the post-buckling regime and is affected by the imperfections. Therefore it is important to characterize the mechanical behavior of structures during the post-buckling regime and the imperfection sensitivity. This section employs the sandwich structure in the case of h_c=60 mm to validate the extended MSG in post-local-buckling analysis and imperfection sensitivity analysis of sandwich structures. The material properties are given in Table 3.11. In FEA, 2D quadratic plane strain elements (CPE8R) are employed. The reason why author uses 2D elements is to reproduce local buckling without the intervention of global buckling such as the type II flexural buckling. An Abaqus user subroutine UANISOHYPER is used to implement the Saint-Venant Kirchhoff material in Abaqus. Eigenvalue buckling analysis is performed first; the first local buckling mode from eigenvalue buckling analysis is used to construct geometric imperfections; various imperfection factors are studied: $k = 0.000001, 0.000005, 0.00001, 0.00005, 0.0001$. Then post-local-buckling analysis is performed using the Riks method in Abaqus. The step size settings for this study in Abaqus are given as follows: initial step size 0.001, minimum step size 0.00001, maximum step size 0.01. 200 steps of iteration are used to capture the load-displacement rupture. Figure 3.35 shows an example of buckled sandwich structure superimposed on the undeformed sandwich structure. The axial shortening is recorded at the center

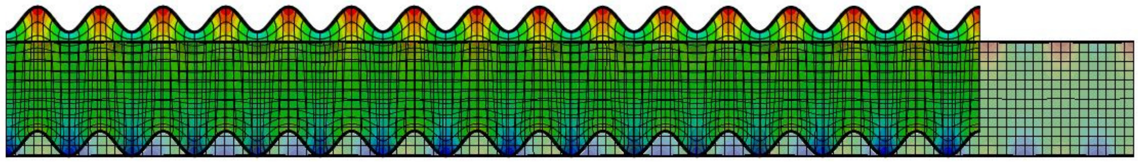

Fig. 3.35. Post-buckled sandwich structure superimposed on the undeformed sandwich structure in FEA solution (imperfection factor k=0.0001, deformation scaling factor=20, step=200).

of tip surface and the deflection is recorded at the top node of the tip surface. In MSG method, the eigenvalue buckling analysis using extended MSG described in section 2.3 is performed first to obtain the buckling mode which is used to construct geometric imperfection and the buckling wavelength. Then the post-buckling analysis using extended MSG described in section 2.4 is performed on a new SG in the size equal to the buckling wavelength. The fluctuating function in MSG solution represents the deflection and is compared with FEA solutions. Figure 3.36 shows the comparison of MSG solutions to FEA solutions in terms of axial shortening to deflection curve. It is seen that MSG solutions agree well with FEA solutions in a variety of imperfections. Other observations can be drawn, for instance, the axial shortening to deflection curve becomes more nonlinear as imperfection decreases. It indicates that the sandwich structure with less imperfection is more sensitive to buckling than the others. Buckled sandwich structure in full length is reproduced based on the buckled SG and is compared with the FEA solution in Fig. 3.37. The good agreement between MSG solution and FEA solution validates the extended MSG method in post-local-buckling analysis.

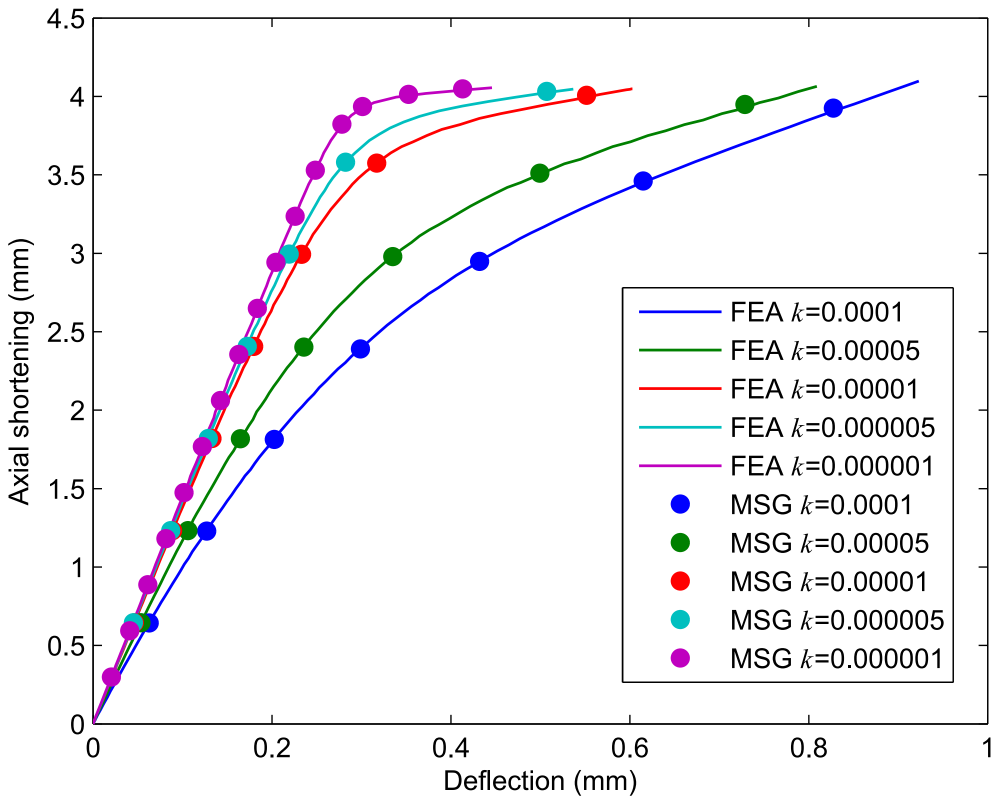

Fig. 3.36. Comparison of current solution with FEA solution in axial shortening to deflection curve. k is the imperfection factor.

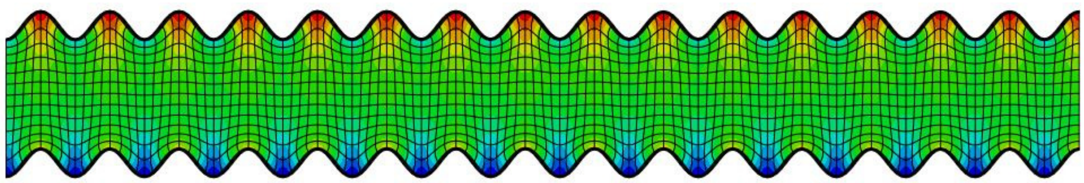

(a) FEA

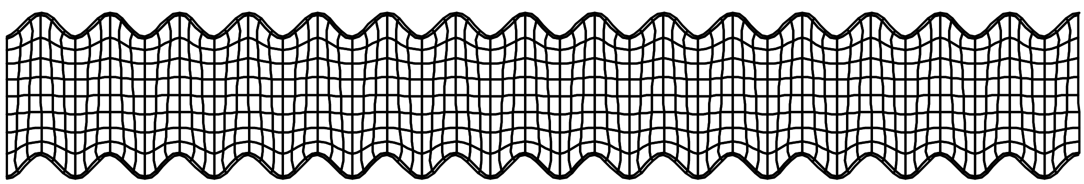

(b) MSG

Fig. 3.37. Comparison of MSG solution with FEA solution in post-buckled sandwich structure (imperfection factor k=0.0001, deformation scaling factor=20).

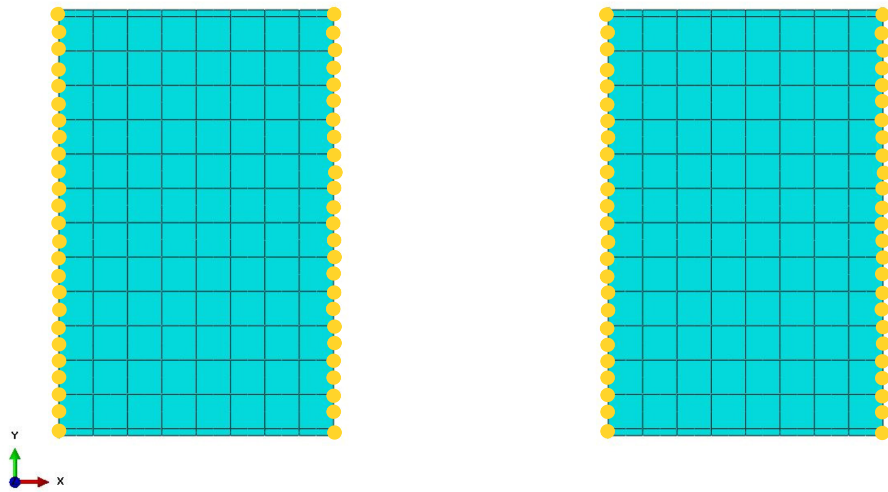

Fig. 3.38. Two identical meshes of RVE in Abaqus representing real and imaginary parts: yellow circles are the coupled nodes on the periodic boundaries.

3.3.7 Implementation of Bloch wave theory in Abaqus

This section deals with the details on how to perform RVE analysis with Bloch wave theory in Abaqus. Then the results of RVE analysis with Bloch wave theory are compared with MSG solutions.

One of the critical issues in applying Bloch-periodic boundary conditions to the RVE analysis in the commercial finite element softwares is that it involves complex-valued numbers thus the commercial finite element softwares are unable to handle it. Ȧberg and Gudmundson [122] proposed to use two identical meshes of RVE so that all quantities are split into real and imaginary parts.

For a RVE of sandwich structure with size L shown in Fig. 3.28, the author creates two identical meshes in Abaqus. Figure 3.38 shows the two identical RVEs of sandwich structure in the case of h_c=60 mm with RVE size L=40 mm. The RVE size is decided based on estimated buckling wavelength using Eqs. (1.3) and (1.5). It should be noted that the RVE is not unique and can be in various size L.

The numerical recipe starts with a geometrically nonlinear static analysis followed by a eigenfrequency analysis. In the geometrically nonlinear analysis, PBC is applied to the periodic boundaries of each RVE respectively. The displacement fluctuations χ on the periodic boundaries equal to each other as follows

$$\chi_+ = \chi_- \tag{3.2}$$

where $+$ and $-$ denote the quantities on the periodic boundaries respectively and

$$\chi_i = u_i - x_j \varepsilon_{ij} \tag{3.3}$$

where u_i is the displacement on the periodic boundaries and ε_{ij} is the applied strain. Here we only apply a nonzero compressive strain ε_{11} in the x_1 direction to study the local buckling under uniaxial compression.

Next in the eigenfrequency analysis, the displacement fluctuations χ at the periodic boundaries are defined according to the Bloch-periodic boundary condition as follows

$$\chi_+ = \chi_- \cdot e^{i2\pi n_1} \tag{3.4}$$

It is noted that in the eigenfrequency analysis, the displacement fluctuations equal to the displacement $\chi_i = u_i$ because no strain is applied $\varepsilon_{ij} = 0$. Therefore Eq. (3.4) is equivalent to

$$u_+ = u_- \cdot e^{i2\pi n_1} \tag{3.5}$$

Due to the fact that all quantities are split into real and imaginary parts, the displacement are also split as follows

$$u = u^{\text{Re}} + i \cdot u^{\text{Im}} \tag{3.6}$$

Then the Bloch-periodic boundary condition in Eq. (3.4) becomes

$$\begin{aligned} u_+^{\text{Re}} &= u_-^{\text{Re}} \cdot \cos(2\pi n_1) - u_-^{\text{Im}} \cdot \sin(2\pi n_1) \\ u_+^{\text{Im}} &= u_-^{\text{Im}} \cdot \cos(2\pi n_1) + u_-^{\text{Re}} \cdot \sin(2\pi n_1) \end{aligned} \tag{3.7}$$

Equation (3.7) is realized using the constraints **Equations* in Abaqus. A python script is developed to automatically generate the coupling constraints and is given in the Appendix B.

The eigenfrequency analysis in Abaqus computes the natural frequencies of an undamped finite element model as follows

$$\left(\begin{bmatrix} K & 0 \\ 0 & K \end{bmatrix} - \omega^2 \begin{bmatrix} M & 0 \\ 0 & M \end{bmatrix}\right) \begin{bmatrix} u^{\mathrm{Re}} \\ u^{\mathrm{Im}} \end{bmatrix} = 0 \tag{3.8}$$

where K is the stiffness matrix that includes the geometric nonlinearity of the static analysis, M is the mass matrix, ω is the natural frequency. Positive eigenvalue $\omega^2 > 0$ indicates stable oscillating motion, and negative eigenvalue $\omega^2 < 0$ indicates motion that grows exponentially in time. Therefore $\omega^2 = 0$ represents the onset of buckling [98]. The buckling problem becomes finding the compressive strain that results in zero natural frequency. Figure 3.39 shows an eigenmode in the solutions of the eigenfrequency analysis.

For every compressive strain ε_{11} applied in PBC in Eq. (3.3) in static nonlinear analysis, the author gets a natural frequency square ω^2 in the eigenfrequency analysis. The procedure is to gradually increase ε_{11} until a negative natural frequency square emerges $\omega^2 < 0$. Then the critical compressive strain can be interpolated between the two consecutive compressive strains that have $\omega^2 > 0$ and $\omega^2 < 0$ respectively.

Both 2D RVE and 3D RVE analysis are performed. In the 2D RVE analysis, we use the second-order plane-stress element (CPS8R). In the 3D RVE analysis, we use the second-order solid element (C3D20R). The author does not prefer 2D plane-stress element over 2D plane-strain element. One can also use 2D plane strain elements for 2D RVE analysis, and compare the results with 2D DNS using plane strain elements. Figures 3.40 and 3.41 show the natural frequency against the compressive strain for different Bloch wave number n in 2D RVE analysis. It is seen that the eigenfrequency is almost linear to compressive displacement. Analysis is performed again in a smaller interval of the compressive displacements and Bloch wave numbers where the curve is likely to intersect with the x axis to find the critical displacement and corresponding

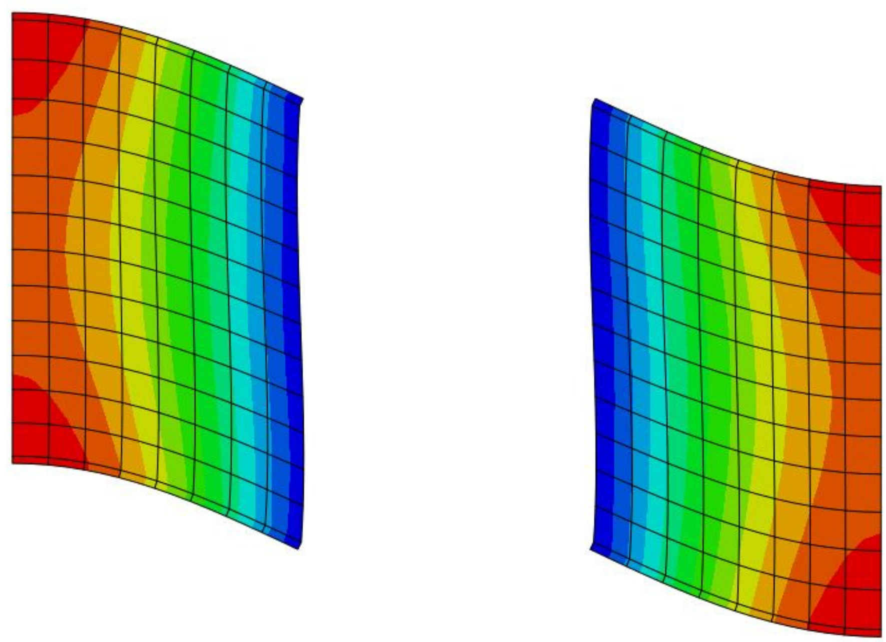

Fig. 3.39. Example of an eigenmode in the solutions of eigenfrequency analysis in Abaqus.

Bloch wave number. Figures 3.42 and 3.43 show the natural frequency against the compressive strain for different Bloch wave number n in 3D RVE analysis. It is noted that the critical compressive displacement in 3D RVE analysis is different from the one in 2D RVE analysis (8.22%). Figure 3.44 shows the critical modes of eigenfrequency analysis of 2D RVE. It can be seen from this figure that the Bloch wave number directly determines the buckling wavelength. Figure 3.45 shows the critical modes of eigenfrequency analysis of 3D RVE. In comparison with 2D RVE analysis results, 3D RVE analysis results show nonuniform expansion in the lateral surfaces. Then these critical compressive displacements are compared with 2D DNS and 3D DNS in Table 3.18. Results of Bloch wave method in Abaqus match very well with 2D and 3D DNS, respectively. MSG solution does not depend on whether it is 2D or 3D SG and is close to 3D FEA result with 2.98% error. In the next section, the author will use the MSG beam model to predict such local buckling.

It is worth to say that the results of RVE analysis strongly depend on if the RVE is 2D or 3D. On the contrary, MSG plate model does not depend on it. Figure 3.46 shows the bucking mode in MSG solution using 2D elements and 3D elements respectively.

3.3.8 Predicting local buckling of sandwich structures using MSG beam model

In previous section, the MSG plate model (Eq. (2.22)) is used to predict the local buckling of sandwich structures. In this section, the author will use the MSG beam model to analyze the local buckling of sandwich structures (Eq. (2.24)) and show that the MSG beam model is more applicable than the MSG plate model for current case study. Illustration of MSG plate model and beam model in buckling analysis of sandwich structure is shown in Fig. 3.47. It should be noted that in comparison with the MSG plate model that use 1D SG across the thickness to model plate-like structures (Fig. 1.9), we extend the 1D SG along the x_1 direction to produce a 2D

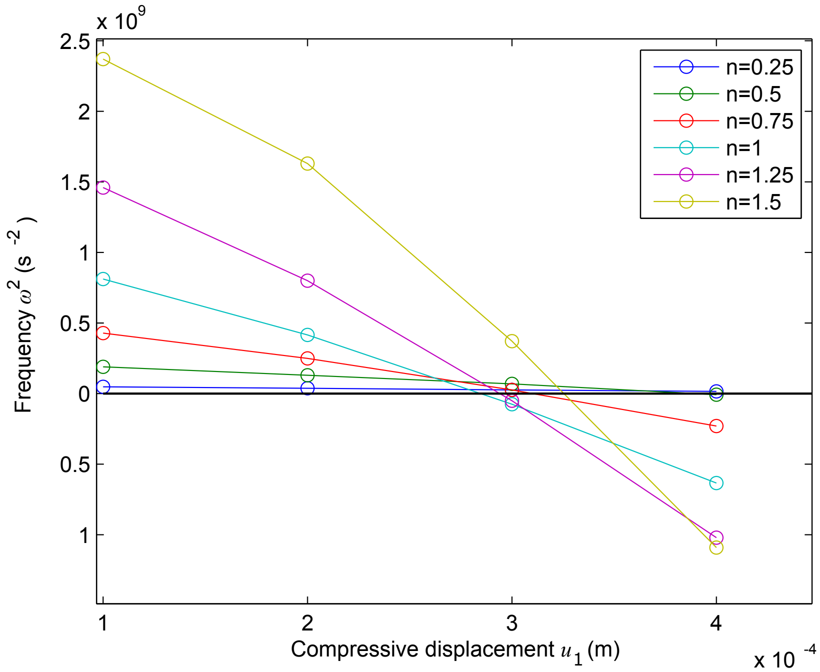

Fig. 3.40. Eigenfrequency analysis results of 2D RVE.

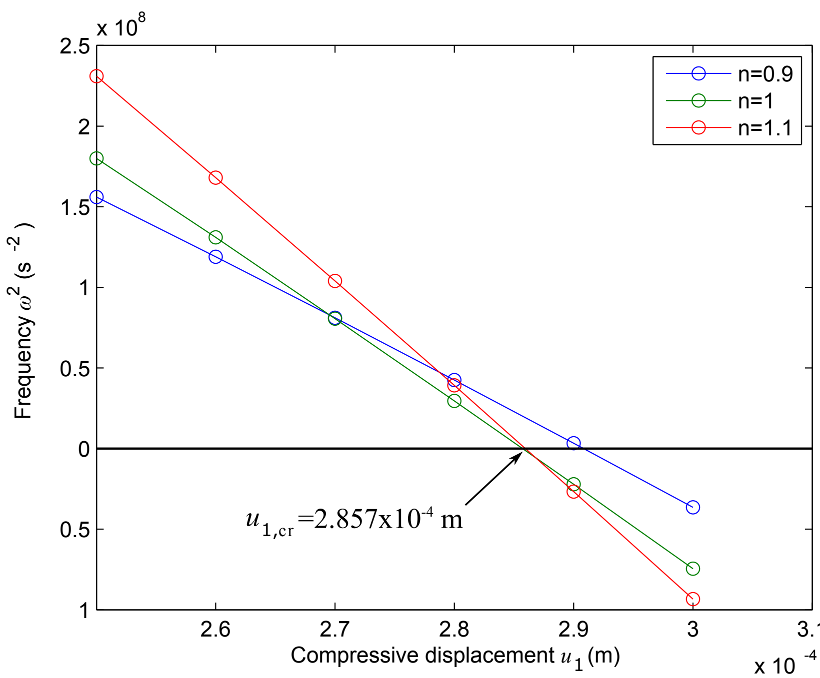

Fig. 3.41. Eigenfrequency analysis results of 2D RVE in a small interval to find critical displacement.

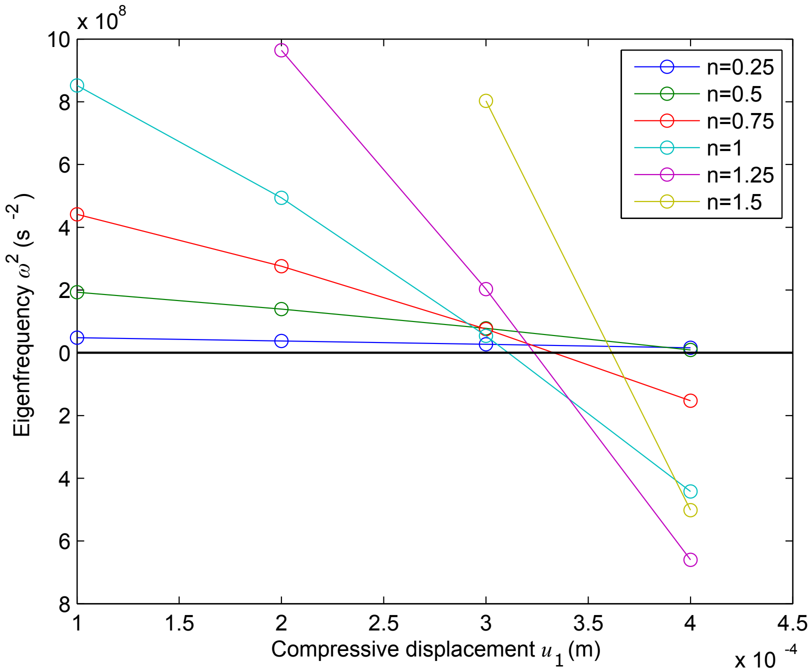

Fig. 3.42. Eigenfrequency analysis results of 3D RVE.

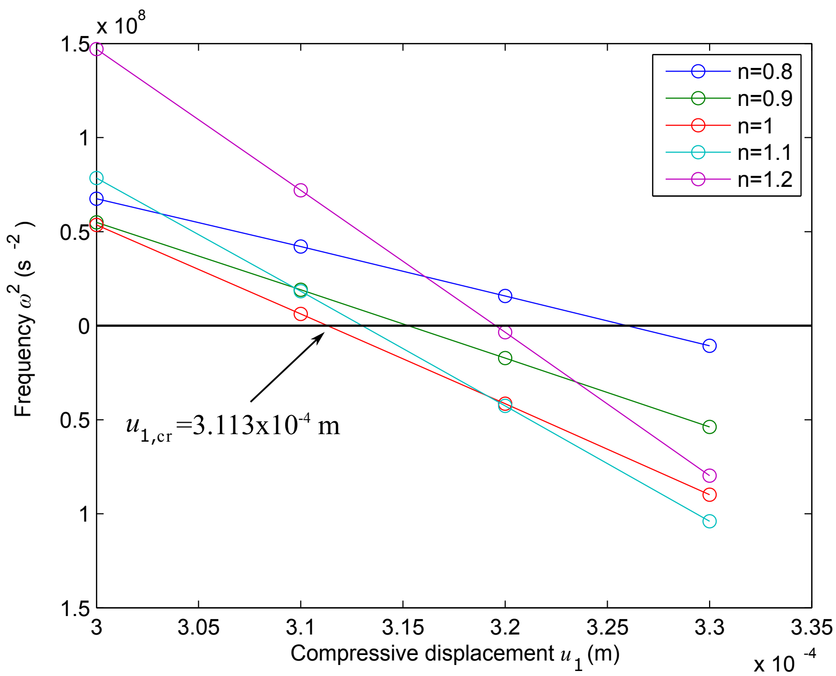

Fig. 3.43. Eigenfrequency analysis results of 3D RVE in a small interval to find critical displacement.

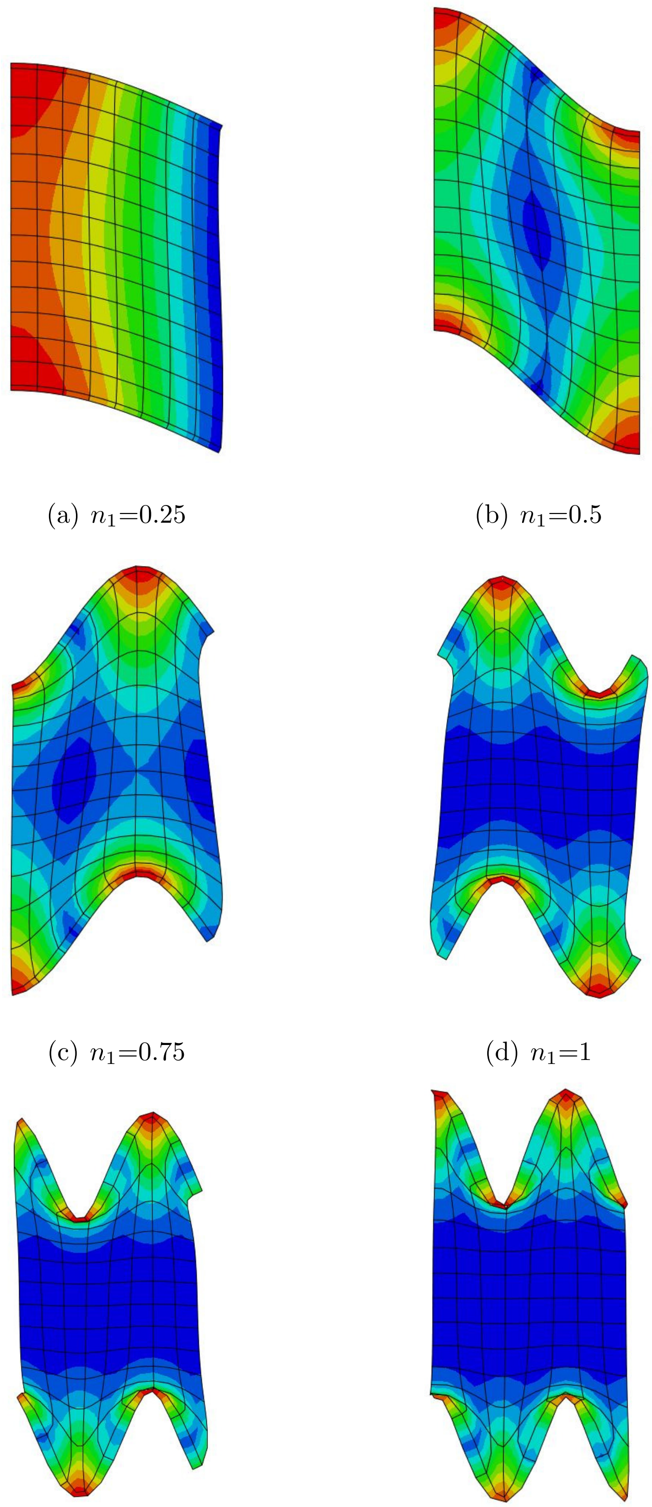

(a) n_1=0.25 (b) n_1=0.5

(c) n_1=0.75 (d) n_1=1

(e) n_1=1.25 (f) n_1=1.5

Fig. 3.44. Critical modes of eigenfrequency analysis of 2D RVE in different Bloch wave number.

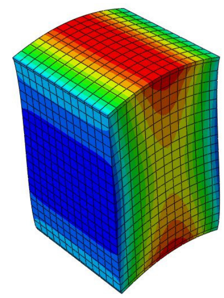

(a) n_1=0.25

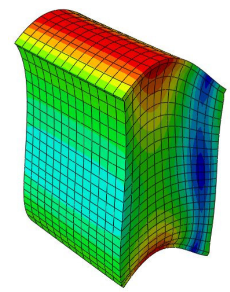

(b) n_1=0.5

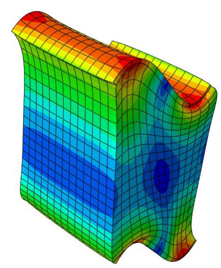

(c) n_1=0.75

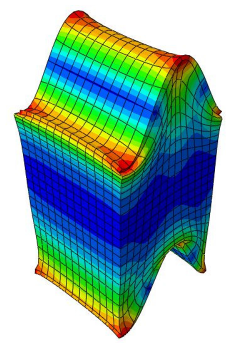

(d) n_1=1

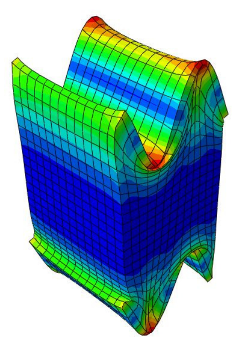

(e) n_1=1.25

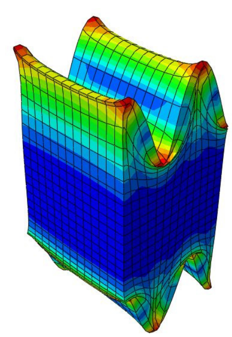

(f) n_1=1.5

Fig. 3.45. Critical modes of eigenfrequency analysis of 3D RVE in different Bloch wave number.

Table 3.18.
Comparing the critical compressive displacement of local buckling: Bloch wave method in MSG, Bloch wave method in Abaqus and DNS (h_c=60 mm).

Method	$u_{1,cr}(mm)$
2D DNS	4.294
3D DNS	4.684
Abaqus Bloch 2D	4.285
Abaqus Bloch 3D	4.670
MSG 2D	4.823
MSG 3D	4.823

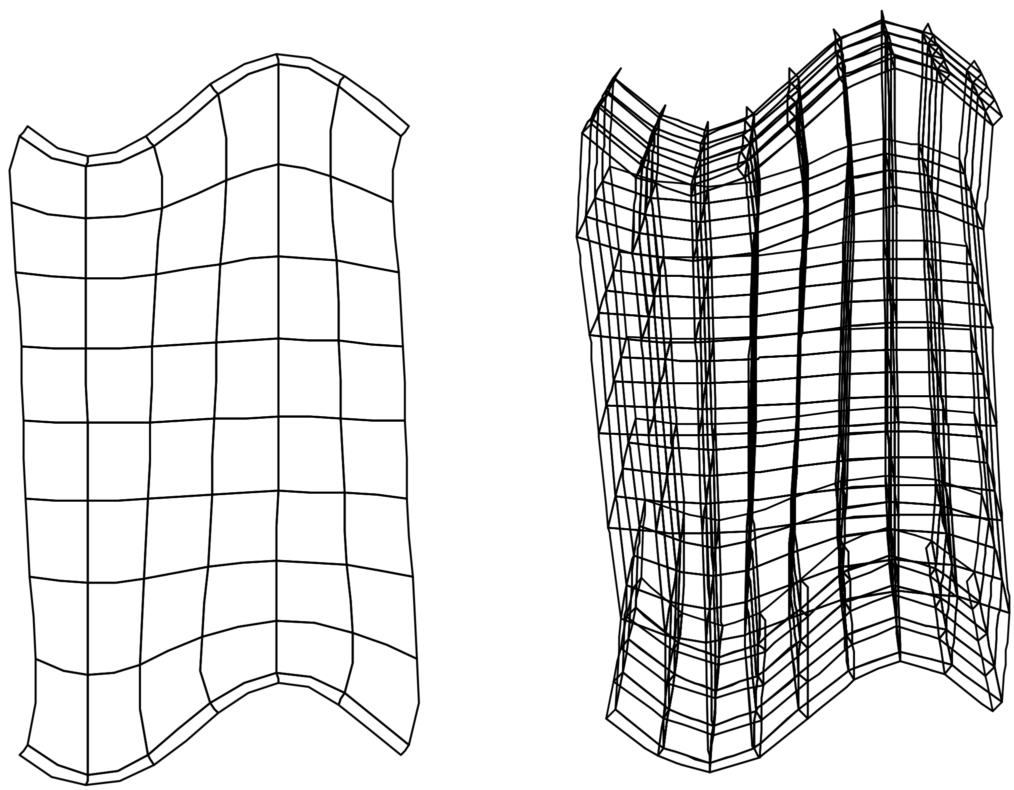

(a) 2D SG

(b) 3D SG

Fig. 3.46. Critical modes in MSG solutions using MSG plate model.

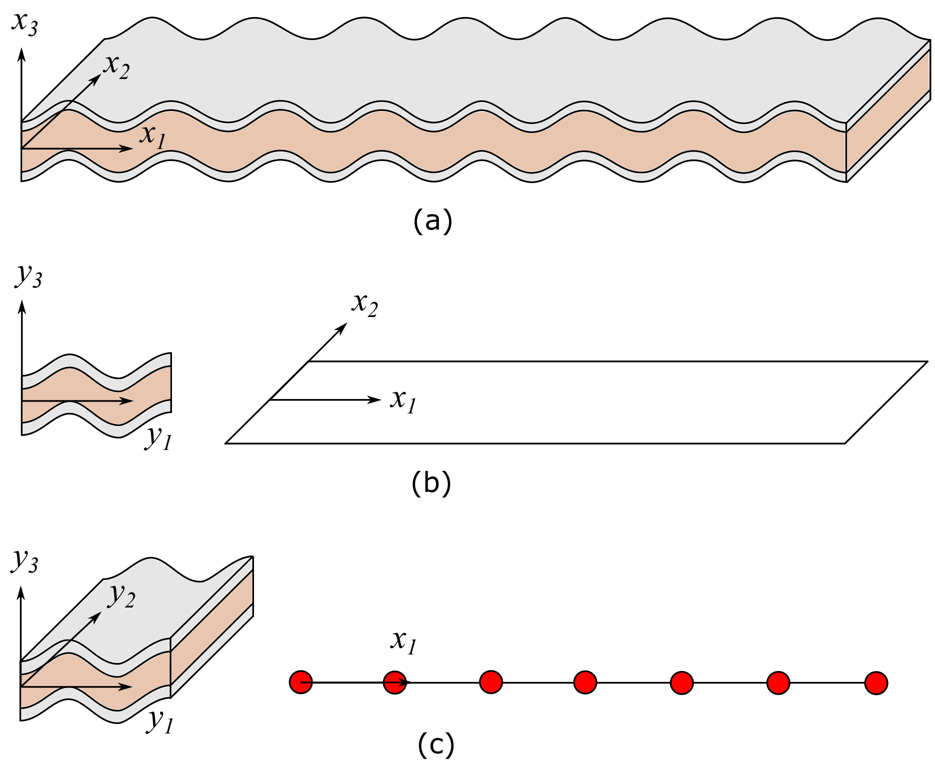

Fig. 3.47. Predicting local buckling of sandwich structures using MSG plate and beam models. (a) Local buckling mode of sandwich structures. (b) Modeling sandwich structures as plates with 2D SG. (c) Modeling sandwich structures as beams with 3D SG.

SG so that it can capture the wave in x_1 direction. Similarly, the SG of beam model is extended from 2D cross-section to a 3D block in x_1 direction. Solutions of MSG plate and MSG beam models are presented in Table 3.19. It is seen that the MSG beam model also agrees with 3D DNS very well in addition to the MSG plate model.

Table 3.19.
Comparing the critical compressive displacement (unit: mm) of local buckling in the case of h_c=30 mm and h_c=60 mm.

	h_c=30 mm	h_c=60 mm
3D DNS	4.444	4.684
MSG plate	4.547 (2.33%)	4.823 (2.98%)
MSG beam	4.440 (0.09%)	4.680 (0.08%)

4. SUMMARY

The homogenization theory, i.e., MSG is extended to study the local buckling of stiffened and sandwich panels. The main improvements of current method compared with other methods seen in literature are avoiding unnecessary assumptions, the capability of predicting all possible buckling modes including the global and local buckling modes and the potential in studying the buckling of various types of structures.

In global buckling analysis, MSG mathematically decouples the original geometrical nonlinear problem into a linear constitutive modeling over the SG and a geometrically nonlinear analysis over the macroscopic model. In the linear constitutive modeling, the effective properties such as the A, B and D matrices are computed. Then the effective properties are used as material properties of macroscopic structures in commercial finite element softwares such as Abaqus to carry out buckling and post-buckling analysis. Lastly, buckling loads, buckling mode shapes and post-buckling curves are predicted through the macroscopic structural analysis.

In local buckling analysis, the wavelengthes of the local modes are in general much smaller than those seen in the global modes, therefore finite local rotations have to be accounted in the constitutive modeling. Current work extends MSG by introducing the St. Venant-Kirchhoff material model and Bloch-periodic boundary conditions. Saint Venant-Kirchhoff material model is an extension of the linear elastic material model to the nonlinear regime. By introducing the St. Venant-Kirchhoff material model, we achieve a geometrical nonlinear constitutive modeling. Newton's method is used to solve the nonlinear equilibrium equations for fluctuating functions. Because the deformation at onset of local buckling may break into a new pattern that does not agree with the geometric periodicity, Bloch-periodic boundary conditions are introduced at this point to accommodate the need of finding all possible deformation periodicity. So the fluctuating functions are perturbed under the Bloch-periodic boundary conditions. The bifurcation is found when the tangent stiffness associated with the perturbed fluctuating functions becomes singular. To predict the post-buckling curves, the arc-length method is used to solve the nonlinear equilibrium equations because of its robustness in comparison with Newton's method which may fail to converge after onset of buckling. The geometrical imperfection is included in the form of scaled buckling mode from linear perturbation.

The method is validated by case studies of stiffened and sandwich panels. Remarkable agreements are seen between the current solutions and DNS solutions. First, the MSG theory is highly accurate in the global buckling of the stiffened composite panels with various grid-patterns and boundary conditions. The buckling modes in current solutions are compared with those in DNS solutions by comparing the pixel values of the grayscale images of buckling mode shapes. Moreover, the predicted post-buckling load-displacement curve using MSG theory matches with DNS very well, yet the time and modeling efforts are significantly reduced. Then, the extended MSG theory is validated in local buckling of stiffened panels with various grid-patterns and geometric parameters. Various local buckling types are seen in current studies such as skin buckling, web buckling and interactive buckling of skin and web, and DNS validates the accuracy of MSG in local buckling analysis. Then, the MSG and extended MSG theory is validated in the buckling of sandwich structures with different core thickness. The author also shows the importance of transverse shear stiffness in global buckling predictions. Parametric studies using MSG reveal the relative influence of core thickness and width on the type II flexural mode and torsional mode. Type II flexural mode is seen to dominate the buckling behavior of sandwich columns whose width is smaller than thickness; torsional mode is seen to be always less critical than type I flexural mode but it should be taken into consideration for very wide sandwich structures. Post-local-buckling of sandwich structure is studied and the MSG solutions well agree with DNS solutions in a wide range of imperfection factors. The author also implements the Bloch wave theory in RVE analysis in Abaqus and compares the results with DNS solutions and MSG solutions. It is found that although

RVE analysis is accurate in reproducing DNS solutions, it strongly depends on RVE dimensionality. In contrast, MSG plate model predicts the same results in regardless of 2D SG or 3D SG, and they shows high accuracy in comparison with 3D FEA results. Lastly, the author shows that using MSG beam model also predicts highly accurate results in local buckling of sandwich structures.

To conclude, the work in this dissertation mainly focuses on developing a geometrical nonlinear constitutive modeling in MSG theory and applying such theory in the global buckling and local buckling analysis of different kinds of structures. It can be used for a fast and accurate estimation of eigenvalue buckling and post-buckling during the preliminary structural design and optimization. From a broader perspective, it is part of a continuing study in predicting instabilities of various periodic structures using the MSG theory such as porous structures, metamaterials. It also lays the foundation for buckling and crippling prediction that often associates with material damage and failure. Future work includes but not limit to introducing material failure criteria and advanced hyperelastic models to predict more sophisticated buckling-related problems. The hyperelastic models is particularly desirable in studying the micro-buckling of high-strain composites that are made of extremely soft matrix materials for deployable structures [123–127]. In a nut shell, this work builds a solid foundation for buckling analysis using MSG theory and can be further improved to achieve more functionalities.

REFERENCES

REFERENCES

[1] D. Bushnell, "Buckling of shells - pitfall for designers," *AIAA Journal*, vol. 19, no. 9, pp. 1183–1226, 1981.

[2] G. J. Simitses and D. H. Hodges, *Fundamentals of Structural Stability.* Boston: Butterworth-Heinemann, 2006.

[3] D. Robbins, "Analysis of fiber micro-buckling in elastomeric composites," in *51st AIAA/ASME/ASCE/AHS/ASC Structures, Structural Dynamics, and Materials Conference*, Orlando, Florida, 2010, p. 2700.

[4] J. Hutchinson and W. Koiter, "Postbuckling theory," *Applied Mechanics Reviews*, vol. 23, no. 12, pp. 1353–1366, 1970.

[5] W. T. Koiter, "The effect of axisymmetric imperfections on the buckling of cylindrical shells under axial compression," *Proceedings Koninklijke Nederlandse Akademie Van Wetenschappen*, vol. 66, no. 5, pp. 265–279, 1963.

[6] H. Wagner and W. Pretschner, "Torsion and buckling of open sections," *NACA-TM-784*, 1936.

[7] E. E. Lundquist and E. Z. Stowell, "Critical compressive stress for flat rectangular plates supported along all edges and elastically restrained against rotation along the unloaded edges," *NACA 733*, 1941.

[8] R. M. Mello, R. E. Sherrer, and M. D. Musgrove, "Intermediate diagonal tension field shear beam development for the Boeing SST," *Journal of Aircraft*, vol. 9, no. 7, pp. 470–476, 1972.

[9] P. Kuhn, J. P. Peterson, and L. R. Levin, "A summary of diagonal tension part I: Methods of analysis," *NASA TN 2661*, 1972.

[10] ——, "A summary of diagonal tension part II: Experimental evidence," *NASA TN 2662*, 1972.

[11] P. Kuhn, "Investigations on the incompletely developed plane diagonal tension field," *NASA 697*, 1940.

[12] ——, *Stresses in Aircraft and Shell Structures.* New York: McGraw-Hill, 1956.

[13] E. Riks, "The application of Newton's method to the problem of elastic stability," *Journal of Applied Mechanics*, vol. 39, no. 4, pp. 1060–1065, 1972.

[14] ——, "Some computational aspects of the stability analysis of nonlinear structures," *Computer Methods in Applied Mechanics and Engineering*, vol. 47, no. 3, pp. 219–259, 1984.

[15] J. W. Hutchinson, “Knockdown factors for buckling of cylindrical and spherical shells subject to reduced biaxial membrane stress,” *International Journal of Solids and Structures*, vol. 47, no. 10, pp. 1443–1448, 2010.

[16] S. Kidane, G. Li, J. Helms, S.-S. Pang, and E. Woldesenbet, “Buckling load analysis of grid stiffened composite cylinders,” *Composites Part B: Engineering*, vol. 34, no. 1, pp. 1–9, 2003.

[17] M.-A. Douville and P. Le Grognec, “Exact analytical solutions for the local and global buckling of sandwich beam-columns under various loadings,” *International Journal of Solids and Structures*, vol. 50, no. 16-17, pp. 2597–2609, August 2013.

[18] H.-J. Chen and S. W. Tsai, “Analysis and optimum design of composite grid structures,” *Journal of Composite Materials*, vol. 30, no. 4, pp. 503–534, March 1996.

[19] M. Ren, T. Li, Q. Huang, and B. Wang, “Numerical investigation into the buckling behavior of advanced grid stiffened composite cylindrical shell,” *Journal of Reinforced Plastics and Composites*, vol. 33, no. 16, pp. 1508–1519, August 2014.

[20] N. Jaunky, N. F. Knight, and D. R. Ambur, “Formulation of an improved smeared stiffener theory for buckling analysis of grid-stiffened composite panels,” *Composites Part B*, vol. 27, no. 5, pp. 519–526, 1996.

[21] Y. Frostig and M. Baruch, “High-order buckling analysis of sandwich beams with transversely flexible core,” *Journal of Engineering Mechanics*, vol. 119, no. 3, pp. 476–495, March 1993.

[22] Y. Frostig, “Buckling of sandwich panels with a flexible core–high-order theory,” *International Journal of Solids and Structures*, vol. 35, no. 3-4, pp. 183–204, 1998.

[23] N. Liu, W. Yu, and D. H. Hodges, “Mechanics of structure genome-based global buckling analysis of stiffened composite panels,” *Acta Mechanica*, Dec 2018. [Online]. Available: https://doi.org/10.1007/s00707-018-2339-4

[24] Q. Zheng, D. Jiang, C. Huang, X. Shang, and S. Ju, “Analysis of failure loads and optimal design of composite lattice cylinder under axial compression,” *Composite Structures*, vol. 131, pp. 885–894, November 2015.

[25] A. Lopatin and E. Morozov, “Buckling of the composite sandwich cylindrical shell with clamped ends under uniform external pressure,” *Composite Structures*, vol. 122, pp. 209–216, April 2015.

[26] E. Wodesenbet, S. Kidane, and S.-S. Pang, “Optimization for buckling loads of grid stiffened composite panels,” *Composite Structures*, vol. 60, no. 2, pp. 159–169, 2003.

[27] P. E. Fenner and A. Watson, “Finite element buckling analysis of stiffened plates with filleted junctions,” *Thin-Walled Structures*, vol. 59, pp. 171–181, October 2012.

[28] C. Bisagni and R. Vescovini, "Analytical formulation for local buckling and post-buckling analysis of stiffened laminated panels," *Thin-Walled Structures*, vol. 47, no. 3, pp. 318–335, March 2009.

[29] R. Szilard, *Theories and Applications of Plate Analysis: Classical, Numerical and Engineering Methods*. New Jersey: John Wiley & Sons, 2004.

[30] M. Sadeghifar, M. Bagheri, and A. A. Jafari, "Buckling analysis of stringer-stiffened laminated cylindrical shells with nonuniform eccentricity," *Archive of Applied Mechanics*, vol. 81, no. 7, pp. 875–887, July 2011.

[31] E. Byklum, E. Steen, and J. Amdahl, "A semi-analytical model for global buckling and postbuckling analysis of stiffened panels," *Thin-Walled Structures*, vol. 42, no. 5, pp. 701–717, 2004.

[32] Y. Xu, Y. Tong, M. Liu, and B. Suman, "A new effective smeared stiffener method for global buckling analysis of grid stiffened composite panels," *Composite Structures*, vol. 158, pp. 83–91, December 2016.

[33] B. Wang, K. Tian, P. Hao, Y. Zheng, Y. Ma, and J. Wang, "Numerical-based smeared stiffener method for global buckling analysis of grid-stiffened composite cylindrical shells," *Composite Structures*, vol. 152, pp. 807–816, September 2016.

[34] D. G. Ninh, D. H. Bich, and B. H. Kien, "Torsional buckling and post-buckling behavior of eccentrically stiffened functionally graded toroidal shell segments surrounded by an elastic medium," *Acta Mechanica*, vol. 226, no. 10, pp. 3501–3520, October 2015.

[35] D. H. Bich and D. G. Ninh, "Research on dynamical buckling of imperfect stiffened three-layered toroidal shell segments containing fluid under mechanical loads," *Acta Mechanica*, vol. 228, no. 2, pp. 711–731, February 2017.

[36] D. Dung and N. Nga, "Buckling and postbuckling nonlinear analysis of imperfect FGM plates reinforced by FGM stiffeners with temperature-dependent properties based on TSDT," *Acta Mechanica*, vol. 227, no. 8, pp. 2377–2402, August 2016.

[37] D. Dung, B. Hoai, and L. Hoa, "Postbuckling nonlinear analysis of FGM truncated conical shells reinforced by orthogonal stiffeners resting on elastic foundations," *Acta Mechanica*, vol. 228, no. 4, pp. 1457–1479, April 2017.

[38] D. Chan, D. Dung, and L. Hoa, "Thermal buckling analysis of stiffened FGM truncated conical shells resting on elastic foundations using FSDT," *Acta Mechanica*, vol. 229, no. 5, pp. 2221–2249, May 2018.

[39] B. Hassani and E. Hinton, "A review of homogenization and topology optimization I - homogenization theory for media with periodic structure," *Computers and Structures*, vol. 69, no. 6, pp. 707–717, 1998.

[40] Y. W. Kwon, D. H. Allen, and R. Talreja, *Multiscale Modeling and Simulation of Composite Materials and Structures*. New York: Springer, 2008.

[41] A. Kalamkarov, I. Andrianov, and V. Danishevs'Kyy, "Asymptotic homogenization of composite materials and structures," *Applied Mechanics Reviews*, vol. 62, no. 3, May 2009.

[42] K. Challagulla, A. Georgiades, and A. Kalamkarov, "Asymptotic homogenization modeling of smart composite generally orthotropic grid-reinforced shells: Part I - theory," *European Journal of Mechanics - A/Solids*, vol. 29, no. 4, pp. 530–540, 2010.

[43] D. Wang and M. M. Abdalla, "Global and local buckling analysis of grid-stiffened composite panels," *Composite Structures*, vol. 119, pp. 767–776, 2015.

[44] D. Zhang and A. M. Waas, "A micromechanics based multiscale model for nonlinear composites," *Acta Mechanica*, vol. 225, no. 4-5, pp. 1391–1417, 2014.

[45] G. Allaire and R. Brizzi, "A multiscale finite element method for numerical homogenization," *Multiscale Modeling and Simulation*, vol. 4, no. 3, pp. 790–812, 2005.

[46] D. Yang, H. Zhang, S. Zhang, and M. Lu, "A multiscale strategy for thermo-elastic plastic stress analysis of heterogeneous multiphase materials," *Acta Mechanica*, vol. 226, no. 5, pp. 1549–1569, 2015.

[47] Y. Efendiev and T. Y. Hou, *Multiscale Finite Element Methods: Theory and Applications*. Berlin, Germany: Springer Science & Business Media, 2009, vol. 4.

[48] T. Hou and X.-H. Wu, "A multiscale finite element method for elliptic problems in composite materials and porous media," *Journal of Computational Physics*, vol. 134, no. 1, pp. 169–189, 1997.

[49] U. K. Mallela and A. Upadhyay, "Buckling of laminated composite stiffened panels subjected to in-plane shear: A parametric study," *Thin-Walled Structures*, vol. 44, no. 3, pp. 354–362, March 2006.

[50] S. Patel, P. Datta, and A. Sheikh, "Buckling and dynamic instability analysis of stiffened shell panels," *Thin-Walled Structures*, vol. 44, no. 3, pp. 321–333, 2006.

[51] C. Graciano and O. Lagerqvist, "Critical buckling of longitudinally stiffened webs subjected to compressive edge loads," *Journal of Constructional Steel Research*, vol. 59, no. 9, pp. 1119–1146, 2003.

[52] M. Madhavan and J. S. Davidson, "Buckling of centerline-stiffened plates subjected to uniaxial eccentric compression," *Thin-Walled Structures*, vol. 43, no. 8, pp. 1264–1276, 2005.

[53] K. Ghavami and M. R. Khedmati, "Numerical and experimental investigations on the compression behaviour of stiffened plates," *Journal of Constructional Steel Research*, vol. 62, no. 11, pp. 1087–1100, 2006.

[54] H. Ovesy, J. Loughlan, and H. Assaee, "The compressive post-local bucking behaviour of thin plates using a semi-energy finite strip approach," *Thin-Walled Structures*, vol. 42, no. 3, pp. 449–475, March 2004.

[55] O. K. Bedair, "The application of mathematical programming techniques to the stability analysis of plate/stiffener assemblies," *Computer Methods in Applied Mechanics and Engineering*, vol. 148, no. 3, pp. 353–365, 1997.

[56] ——, "Analysis of stiffened plates under lateral loading using sequential quadratic programming (SQP)," *Computers and Structures*, vol. 62, no. 1, pp. 63–80, 1997.

[57] L. Peng, K. Liew, and S. Kitipornchai, "Buckling and free vibration analyses of stiffened plates using the FSDT mesh-free method," *Journal of Sound and Vibration*, vol. 289, no. 3, pp. 421–450, January 2006.

[58] E. Byklum and J. Amdahl, "A simplified method for elastic large deflection analysis of plates and stiffened panels due to local buckling," *Thin-Walled Structures*, vol. 40, no. 11, pp. 925–953, 2002.

[59] R. Vescovini and C. Bisagni, "Buckling analysis and optimization of stiffened composite flat and curved panels," *AIAA Journal*, vol. 50, no. 4, pp. 904–915, 2012.

[60] ——, "Two-step procedure for fast post-buckling analysis of composite stiffened panels," *Computers and Structures*, vol. 128, pp. 38–47, 2013.

[61] C. Mittelstedt and M. Beerhorst, "Closed-form buckling analysis of compressively loaded composite plates braced by omega-stringers," *Composite Structures*, vol. 88, no. 3, pp. 424–435, 2009.

[62] D. Stamatelos, G. Labeas, and K. Tserpes, "Analytical calculation of local buckling and post-buckling behavior of isotropic and orthotropic stiffened panels," *Thin-Walled Structures*, vol. 49, no. 3, pp. 422–430, 2011.

[63] L. Lotoing, S. Drapier, and A. Vautrin, "First applications of a novel unified model for global and local buckling of sandwich columns," *European Journal of Mechanics - A/Solids*, vol. 21, no. 4, pp. 683–701, 2002.

[64] G. Kardomateas, "Wrinkling of wide sandwich panels/beams with orthotropic phases by an elasticity approach," *Journal of Applied Mechanics*, vol. 72, no. 6, pp. 818–825, November 2005.

[65] K. Niu and R. Talreja, "Modeling of wrinkling in sandwich panels under compression," *Journal of Engineering Mechanics*, vol. 125, no. 8, pp. 875–883, August 1999.

[66] G. Gough, C. Elam, G. Tipper, and N. De Bruyne, "The stabilisation of a thin sheet by a continuous supporting medium," *The Aeronautical Journal*, vol. 44, no. 349, pp. 12–43, 1940.

[67] N. J. Hoff and S. Mautner, "Buckling of sandwich-type panels," *Journal of the Aeronautical Sciences.*, vol. 12, pp. 285–298, July 1945.

[68] F. J. Plantema, *Sandwich Construction: the Bending and Buckling of Sandwich Beams, Plates, and Shells*. New York: Wiley, 1966.

[69] H. G. Allen, *Analysis and Design of Structural Sandwich Panels: the Commonwealth and International Library: Structures and Solid Body Mechanics Division*. Oxford, New York: Pergamon Press, 1969.

[70] L. Fagerberg, "Wrinkling of sandwich panels for marine applications," Ph.D. dissertation, Royal Institute of Technology, 2003.

[71] Y. Frostig, M. Baruch, O. Vilnay, and I. Sheinman, "High-order theory for sandwich-beam behavior with transversely flexible core," *Journal of Engineering Mechanics*, vol. 118, pp. 1026–1044, May 1992.

[72] C. N. Phan, Y. Frostig, and G. A. Kardomateas, "Analysis of sandwich beams with a compliant core and with in-plane rigidity–extended high-order sandwich panel theory versus elasticity," *Journal of Applied Mechanics*, vol. 79, no. 4, pp. 1–12, July 2012.

[73] C. N. Phan, G. A. Kardomateas, and Y. Frostig, "Global buckling of sandwich beams based on the extended high-order theory," *AIAA Journal*, vol. 50, no. 8, pp. 1707–1717, August 2012.

[74] C. N. Phan, N. W. Bailey, G. A. Kardomateas, and M. A. Battley, "Wrinkling of sandwich wide panels/beams based on the extended high-order sandwich panel theory: formulation, comparison with elasticity and experiments," *Archive of Applied Mechanics*, vol. 82, no. 10/11, pp. 1585–1600, October 2012.

[75] L. Lotoing, S. Drapier, and A. Vautrin, "Nonlinear interaction of geometrical and material properties in sandwich beam instabilities," *International Journal of Solids and Structures*, vol. 39, no. 13, pp. 3717–3739, 2002.

[76] P. Jasion, E. Magnucka-Blandzi, W. Szyc, and K. Magnucki, "Global and local buckling of sandwich circular and beam-rectangular plates with metal foam core," *Thin-Walled Structures*, vol. 61, pp. 154–161, December 2012.

[77] K. S. Saoud and P. Le Grognec, "An enriched 1D finite element for the buckling analysis of sandwich beam-columns," *Computational Mechanics*, vol. 57, no. 6, pp. 887–901, June 2016.

[78] P. Le Grognec and K. S. Saoud, "Elastoplastic buckling and post-buckling analysis of sandwich columns," *International Journal of Non-Linear Mechanics*, vol. 72, pp. 67–79, June 2015.

[79] K. Sad Saoud and P. Le Grognec, "Post-buckling analysis of elastoplastic sandwich columns by means of an enriched 1D finite element model." *International Journal of Solids and Structures*, vol. 129, pp. 90–103, December 2017.

[80] H. Hu, S. Belouettar, M. Potier-Ferry, and A. Makradi, "A novel finite element for global and local buckling analysis of sandwich beams," *Composite Structures*, vol. 90, no. 3, pp. 270–278, 2009.

[81] H. Hu, S. Belouettar, M. Potier-Ferry, A. Makradi, and Y. Koutsawa, "Assessment of various kinematic models for instability analysis of sandwich beams," *Engineering Structures*, vol. 33, no. 2, pp. 572–579, February 2011.

[82] Y. Liu, K. Yu, H. Hu, S. Belouettar, M. Potier-Ferry, and N. Damil, "A new fourier-related double scale analysis for instability phenomena in sandwich structures," *International Journal of Solids and Structures*, vol. 49, no. 22, pp. 3077–3089, November 2012.

[83] K. Yu, H. Hu, S. Chen, S. Belouettar, and M. Potier-Ferry, "Multi-scale techniques to analyze instabilities in sandwich structures," *Composite Structures*, vol. 96, pp. 751–762, February 2013.

[84] G. W. Hunt, L. S. D. Silva, and G. M. E. Manzocchi, "Interactive buckling in sandwich structures," *Proceedings of the Royal Society of London. Series A, Mathematical and Physical Sciences (1934-1990)*, vol. 417, no. 1852, pp. 155–177, May 1988.

[85] S. Yiatros and M. A. Wadee, "Interactive buckling in sandwich beam-columns," *IMA Journal of Applied Mathematics*, vol. 76, no. 1, pp. 146–168, 2011.

[86] J. Hohe and L. Librescu, "Advances in the structural modeling of elastic sandwich panels," *Mechanics of Advanced Materials and Structures*, vol. 11, no. 4-5, pp. 395–424, July 2004.

[87] Y. He, Y. Zhou, Z. Liu, and K. Liew, "Buckling and pattern transformation of modified periodic lattice structures," *Extreme Mechanics Letters*, vol. 22, pp. 112–121, 2018.

[88] C. Kittel, *Introduction to Solid State Physics*, 8th ed. Hoboken, NJ: John Wiley, 2005.

[89] G. Geymonat, S. Müller, and N. Triantafyllidis, "Homogenization of nonlinearly elastic materials, microscopic bifurcation and macroscopic loss of rank-one convexity," *Archive for Rational Mechanics and Analysis*, vol. 122, no. 3, pp. 231–290, September 1993.

[90] N. Triantafyllidis and B. N. Maker, "On the comparison between microscopic and macroscopic instability mechanisms in a class of fiber-reinforced composites," *Journal of Applied Mechanics*, vol. 52, no. 4, pp. 794–800, 1985.

[91] N. Triantafyllidis and M. Schraad, "Onset of failure in aluminum honeycombs under general in-plane loading," *Journal of the Mechanics and Physics of Solids*, vol. 46, no. 6, pp. 1089–1124, 1998.

[92] N. Triantafyllidis, "Failure surfaces for finitely strained two-phase periodic solids under general in-plane loading," *Journal of Applied Mechanics*, vol. 73, no. 3, pp. 505–516, May 2006.

[93] X. Ning and S. Pellegrino, "Bloch wave buckling analysis of axially loaded periodic cylindrical shells," *Computers and Structures*, vol. 177, pp. 114–125, December 2016.

[94] V. D. Do and P. Le Grognec, "Buckling analysis of a reinforced sandwich column using the bloch wave theory," *Thin-Walled Structures*, vol. 115, pp. 323–335, June 2017.

[95] K. Bertoldi, M. Boyce, S. Deschanel, S. Prange, and T. Mullin, "Mechanics of deformation-triggered pattern transformations and superelastic behavior in periodic elastomeric structures," *Journal of the Mechanics and Physics of Solids*, vol. 56, no. 8, pp. 2642–2669, August 2008.

[96] K. Bertoldi, P. M. Reis, S. Willshaw, and T. Mullin, "Negative poisson's ratio behavior induced by an elastic instability," *Advanced Materials*, vol. 22, no. 3, pp. 361–366, 2010.

[97] P. Wang, F. Casadei, S. Shan, J. C. Weaver, and K. Bertoldi, "Harnessing buckling to design tunable locally resonant acoustic metamaterials," *Physical Review Letters*, vol. 113, no. 1, p. 014301, 2014.

[98] J. Liu and K. Bertoldi, "Bloch wave approach for the analysis of sequential bifurcations in bilayer structures," in *Proceedings of the Royal Society A: Mathematical, Physical and Engineering Sciences*, vol. 471, no. 2182. Royal Society of London, 2015.

[99] D. Yang, B. Mosadegh, A. Ainla, B. Lee, F. Khashai, Z. Suo, K. Bertoldi, and G. M. Whitesides, "Buckling of elastomeric beams enables actuation of soft machines," *Advanced Materials*, vol. 27, no. 41, pp. 6323–6327, 2015.

[100] D. Kochmann and K. Bertoldi, "Exploiting microstructural instabilities in solids and structures: From metamaterials to structural transitions," *Applied Mechanics Reviews*, vol. 69, no. 5, p. 050801, 2017.

[101] W. Yu, "A unified theory for constitutive modeling of composites," *Journal of Mechanics of Materials and Structures*, vol. 11, no. 4, pp. 379–411, 2016.

[102] X. Liu and W. Yu, "A novel approach to analyze beam-like composite structures using mechanics of structure genome," *Advances in Engineering Software*, vol. 100, pp. 238–251, 2016.

[103] B. Peng, J. Goodsell, R. B. Pipes, and W. Yu, "Generalized free-edge stress analysis using mechanics of structure genome," *Journal of Applied Mechanics*, vol. 83, no. 10, p. 101013, 2016.

[104] N. Liu and W. Yu, "Evaluation of smeared properties approaches and mechanics of structure genome for analyzing composite beams," *Mechanics of Advanced Materials and Structures*, pp. 1–15, July 2017.

[105] K. Rouf, X. Liu, and W. Yu, "Multiscale structural analysis of textile composites using mechanics of structure genome," *International Journal of Solids and Structures*, vol. 136-137, pp. 89–102, April 2018.

[106] A. Bensoussan, J.-L. Lions, and G. Papanicolaou, *Asymptotic Analysis for Periodic Structures*. American Mathematical Society, 2011, vol. 374.

[107] W. Yu, "Asymptotic construction of Reissner-like composite plate theory with accurate strain recovery," *International Journal of Solids and Structures*, vol. 39, no. 20, pp. 5185–5204, October 2002.

[108] W. Yu, D. H. Hodges, and J. C. Ho, "Variational asymptotic beam sectional analysis - an updated version," *International Journal of Engineering Science*, vol. 59, pp. 40–64, October 2012.

[109] W. Yu and D. H. Hodges, "A geometrically nonlinear shear deformation theory for composite shells," *Journal of Applied Mechanics*, vol. 71, no. 1, pp. 1–9, January 2004.

[110] W. Pietraszkiewicz and V. Eremeyev, "On natural strain measures of the nonlinear micropolar continuum," *International Journal of Solids and Structures*, vol. 46, no. 3, pp. 774–787, 2009.

[111] W. Yu, D. H. Hodges, and V. V. Volovoi, "Asymptotic generalization of Reissner-Mindlin theory: accurate three-dimensional recovery for composite shells," *Computer Methods in Applied Mechanics and Engineering*, vol. 191, no. 44, pp. 5087–5110, October 2002.

[112] D. H. Hodges, *Nonlinear composite beam theory.* American Institute of Aeronautics and Astronautics, 2006.

[113] D. Danielson and D. Hodges, "Nonlinear beam kinematics by decomposition of the rotation tensor," *Journal of Applied Mechanics*, vol. 54, no. 2, pp. 258–262, June 1987.

[114] N. Vasios. (2015) The arc length method. [Online]. Available: https://scholar.harvard.edu/files/vasios/files/ArcLength.pdf

[115] A. Lopatin, "Buckling of the SSCF rectangular orthotropic plate subjected to linearly varying in-plane loading," *Composite Structures*, vol. 93, no. 7, pp. 1900–1910, June 2011.

[116] I. Shufrin, O. Rabinovitch, and M. Eisenberger, "Buckling of symmetrically laminated rectangular plates with general boundary conditions - A semi analytical approach," *Composite Structures*, vol. 82, no. 4, pp. 521–531, 2008.

[117] M. A. A. Meziane, H. H. Abdelaziz, and A. Tounsi, "An efficient and simple refined theory for buckling and free vibration of exponentially graded sandwich plates under various boundary conditions," *Journal of Sandwich Structures and Materials*, vol. 16, no. 3, pp. 293–318, May 2014.

[118] S. Kumar Panda, "Buckling of rectangular plates with various boundary conditions loaded by non-uniform inplane loads," *International Journal of Mechanical Sciences*, vol. 52, no. 6, pp. 819–829, June 2010.

[119] S. J. Hamedani and A. R. Ranji, "Buckling analysis of stiffened plates subjected to non-uniform biaxial compressive loads using conventional and super finite elements," *Thin-Walled Structures*, vol. 64, pp. 41–49, 2013.

[120] J. N. Reddy, *Mechanics of Laminated Composite Plates and Shells: Theory and Analysis*, 2nd ed. Boca Raton: CRC Press, 2004.

[121] O. A. Bauchau and J. I. Craig, *Structural Analysis: With Applications to Aerospace Structures.* Berlin, Germany: Springer Science & Business Media, 2009, vol. 163.

[122] M. Ȧberg and P. Gudmundson, "The usage of standard finite element codes for computation of dispersion relations in materials with periodic microstructure," *Journal of the Acoustical Society of America*, vol. 102, no. 4, pp. 2007–2013, 1997.

[123] T. W. Murphey, "Large strain composite materials in deployable space structures," in *17th International Conference on Composite Materials*, vol. 28. The British Composites Soc. Edinburgh, UK, 2009.

[124] G. Sanford, A. Biskner, and T. Murphey, "Large strain behavior of thin unidirectional composite flexures," in *51st AIAA/ASME/ASCE/AHS/ASC Structures, Structural Dynamics, and Materials Conference*, Orlando, Florida, 2010, p. 2698.

[125] W. H. Francis IV, "Mechanics of post-microbuckled compliant-matrix composites," Ph.D. dissertation, University of Colorado at Boulder, 2008.

[126] J. M. Mejia-Ariza and T. W. Murphey, "Flexible lightweight adjustable stiffness hinge (FLASH) for advanced cable technology," in *57th AIAA/ASCE/AHS/ASC Structures, Structural Dynamics, and Materials Conference*, San Diego, California, 2016, p. 1415.

[127] T. W. Murphey, W. Francis, B. Davis, and J. M. Mejia-Ariza, "High strain composites," in *2nd AIAA Spacecraft Structures Conference*, Kissimmee, Florida, 2015, p. 0942.

APPENDICES

A. TRANSVERSE SHEAR STIFFNESS OF PLATE STRUCTURES

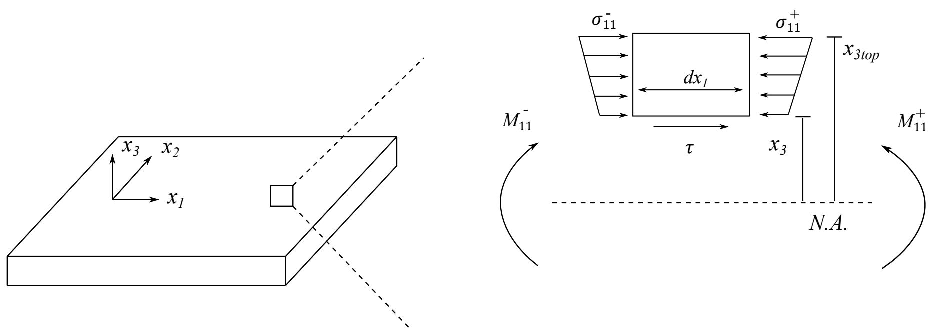

Fig. A.1. Segment of length dx_1 in a distance x_3 from neutral axis (N.A.).

For a plate under bending in x_1 direction, the force equilibrium in x_1 direction for a segment shown in the Fig. A.1 is

$$\tau dx_1 = \int_{x_3}^{x_{3top}} \sigma_{11}^{+} dx_3 - \int_{x_3}^{x_{3top}} \sigma_{11}^{-} dx_3 \tag{A.1}$$

where τ is the shear stress for the segment to be in equilibrium. Divide dx on both sides of the Eq. (A.1), we obtain

$$\tau = \int_{x_3}^{x_{3top}} \sigma_{11,1} dx_3 \tag{A.2}$$

According to Hooke's law, σ_{11} is related to the 3D strains as

$$\sigma_{11} = (2\mu + \lambda)\varepsilon_{11} + \lambda\varepsilon_{22} + \lambda\varepsilon_{33} \tag{A.3}$$

where λ and μ are Lamé constants. The 3D strains can be related to 2D plate stain and curvatures in a classical plate model as follows

$$\begin{aligned} \varepsilon_{\alpha\beta} &= \epsilon_{\alpha\beta} + x_3\kappa_{\alpha\beta} \\ \varepsilon_{33} &= 0 \end{aligned} \tag{A.4}$$

Substitute Eq. (A.4) in Eq. (A.3) then in Eq. (A.2), we obtain

$$\tau = \int_{x_3}^{x_{3top}} \Big[(2\mu + \lambda)(\epsilon_{11} + x_3\kappa_{11})_{,1} + \lambda(\epsilon_{22} + x_3\kappa_{22})_{,1}\Big] dx_3 \tag{A.5}$$

The 2D strain and curvatures can be computed using the inverse of A, B and D matrices in Eq. (2.45) as follows

$$\left\{ \begin{array}{c} \epsilon \\ \kappa \end{array} \right\} = H \left\{ \begin{array}{c} N \\ M \end{array} \right\} \tag{A.6}$$

where H is

$$H = \begin{bmatrix} A & B \\ B & D \end{bmatrix}^{-1} \tag{A.7}$$

Under the bending moment M_{11}, the 2D strains and curvatures can be computed as follows

$$\left\{ \begin{array}{c} \epsilon \\ \kappa \end{array} \right\} = \left[\begin{array}{cccccc} H_{14} & H_{24} & H_{34} & H_{44} & H_{54} & H_{64} \end{array} \right]^T M_{11} \tag{A.8}$$

Assume $M_{22} = M_{12} = 0$, the equilibrium equation for a plate under bending moment M_{11} is

$$M_{11,1} - N_{13} = 0 \tag{A.9}$$

where N_{13} is the shear stress resultant. Substitute Eq. (A.8) in Eq. (A.5) and then substitute Eq. (A.9) in Eq. (A.5), we obtain

$$\tau = N_{13} \int_{x_3}^{x_{3top}} \Big[(2\mu + \lambda)(H_{14} + x_3H_{44}) + \lambda(H_{24} + x_3H_{54})\Big] dx_3 \tag{A.10}$$

For sandwich plates whose flanges and core are made of isotropic materials, the transverse shear stiffness in the two transverse directions x_1 and x_2 are decoupled, i.e., $K_{12} = 0$ and equal to each other, i.e., $K_{11} = K_{22}$. Then the strain energy in terms of the transverse shear stress τ is

$$U = \frac{1}{2} \int \frac{\tau^2}{\mu} dx_3 \tag{A.11}$$

The strain energy in terms of the shear stress resultant N_{13} is

$$U = \frac{1}{2} \frac{N_{13}^2}{K_{11}} \tag{A.12}$$

from which we obtain

$$\frac{N_{13}^2}{K_{11}} = \int \frac{\tau^2}{\mu} dx_3 \tag{A.13}$$

Substitute Eq. (A.10) in Eq. (A.13), we can compute the K_{11}.

B. PYTHON SCRIPT FOR APPLYING THE BLOCH-PERIODIC BOUNDARY CONDITIONS IN ABAQUS

Two meshes are created in Abaqus for realizing Bloch-periodic boundary conditions. A Python script is developed to automatically couple the master and slave nodes on the periodic boundaries of two meshes.

```
#
# Select the model, part and instants that has real and
    imiginary parts
#
modelName = 'Model-1'
partName = 'Part-1'
instNameRe = 'Part-1-1'
instNameIm = 'Part-1-2'
#
# Define the periodic surface or edge in sets named 'Re_a'
    and 'Re_b'
#
a=[]
for i in mdb.models[modelName].parts[partName].sets['Re_a'].
    nodes:
    a=a+[(i.coordinates[0],i.coordinates[1],i.label)]
a.sort(key=lambda row:row[0])
a.sort(key=lambda row:row[1])
rep=1
```

```
for i in a:
    mdb.models[modelName].parts[partName].Set(name='Node-'+str(rep), nodes=
        mdb.models[modelName].parts[partName].nodes[(i[2]-1):(i[2])])
    rep=rep+2
#
a=[]
for i in mdb.models[modelName].parts[partName].sets['Re_b'].nodes:
    a=a+[(i.coordinates[0],i.coordinates[1],i.label)]
a.sort(key=lambda row:row[0])
a.sort(key=lambda row:row[1])
rep=2
for i in a:
    mdb.models[modelName].parts[partName].Set(name='Node-'+str(rep), nodes=
        mdb.models[modelName].parts[partName].nodes[(i[2]-1):(i[2])])
    rep=rep+2
LenAV=len(a)
#
# Define the cosine and sine values associated with Bloch wave number.
# For example, n=0.5, cos(2*pi*n)= -1,  sin(2*pi*n)= 0,
#
cos=-1
sin=0
#
```

```
# BC for displacement in x
#
rep=1
for i in range(0,LenAV):
    mdb.models[modelName].Equation(name='Bloch-Constraint-x-
        Re'+str(i+1),
            terms=((1, instNameRe+'.Node-'+str(rep+1), 1),(-cos,
                instNameRe+'.Node-'+str(rep), 1),(sin, instNameIm+
                '.Node-'+str(rep), 1)))
    rep=rep+2
rep=1
for i in range(0,LenAV):
    mdb.models[modelName].Equation(name='Bloch-Constraint-x-
        Im'+str(i+1),
            terms=((1, instNameIm+'.Node-'+str(rep+1), 1),(-sin,
                instNameRe+'.Node-'+str(rep), 1),(-cos, instNameIm
                +'.Node-'+str(rep), 1)))
    rep=rep+2
#
# BC for displacement in y
#
rep=1
for i in range(0,LenAV):
    mdb.models[modelName].Equation(name='Bloch-Constraint-y-
        Re'+str(i+1),
            terms=((1, instNameRe+'.Node-'+str(rep+1), 2),(-cos,
                instNameRe+'.Node-'+str(rep), 2),(sin, instNameIm+
                '.Node-'+str(rep), 2)))
    rep=rep+2
```

```
rep=1
for i in range(0,LenAV):
    mdb.models[modelName].Equation(name='Bloch-Constraint-y-Im'+str(i+1),
        terms=((1, instNameIm+'.Node-'+str(rep+1), 2),(-sin, instNameRe+'.Node-'+str(rep), 2),(-cos, instNameIm+'.Node-'+str(rep), 2)))
    rep=rep+2
#
# BC for displacement in z
#
rep=1
for i in range(0,LenAV):
    mdb.models[modelName].Equation(name='Bloch-Constraint-z-Re'+str(i+1),
        terms=((1, instNameRe+'.Node-'+str(rep+1), 3),(-cos, instNameRe+'.Node-'+str(rep), 3),(sin, instNameIm+'.Node-'+str(rep), 3)))
    rep=rep+2
rep=1
for i in range(0,LenAV):
    mdb.models[modelName].Equation(name='Bloch-Constraint-z-Im'+str(i+1),
        terms=((1, instNameIm+'.Node-'+str(rep+1), 3),(-sin, instNameRe+'.Node-'+str(rep), 3),(-cos, instNameIm+'.Node-'+str(rep), 3)))
    rep=rep+2
```

VITA

VITA

Ning Liu was born in Baoding, Hebei, China in August 15, 1990. He graduated from Tsinghua High School in June, 2009. He entered Northwestern Polytechnical University at Xi'an, China in September, 2009 and received Bachelor of Science in June, 2013. He then entered Purdue University in August, 2013 and received Master of Science in Aeronautics and Astronautics in May, 2015. He started his Ph.D. in Purdue University in August, 2015.